

**EFFECTS OF TEMPERATURE TRANSIENTS ON THE STALL AND STALL
RECOVERY AERODYNAMICS OF A MULTI-STAGE AXIAL FLOW
COMPRESSOR**

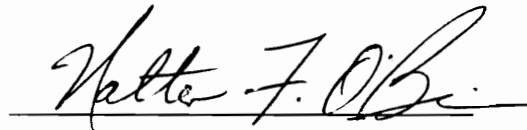
(A NEW TECHNIQUE FOR ACTIVE RECOVERY FROM ROTATING STALL)

by

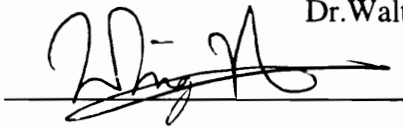
Anthony L. DiPietro Jr.

Dissertation submitted to the Faculty of the
Virginia Polytechnic Institute and State University
in partial fulfillment of the requirements for the degree of
Doctor of Philosophy
in
Mechanical Engineering

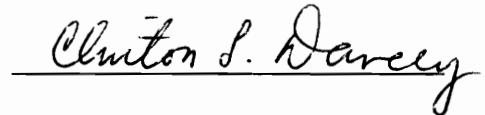
APPROVED



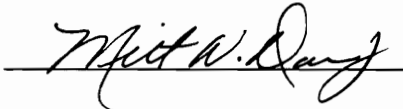
Dr. Walter F. O'Brien, Chairman




Dr. Wing-fai Ng



Dr. Clinton L. Dancey



Dr. Milton W. Davis Jr.



Dr. John Moore

February, 1997

Blacksburg, Virginia

Key words: Compressor, Stall, Temperature, Transient, Distortion

C.2

LD
5655
V856
1997
D575
c.2

**EFFECTS OF TEMPERATURE TRANSIENTS ON THE STALL AND STALL
RECOVERY AERODYNAMICS OF A MULTI-STAGE AXIAL FLOW
COMPRESSOR**

(A NEW TECHNIQUE FOR ACTIVE RECOVERY FROM ROTATING STALL)

by

Anthony L. DiPietro Jr.

Committee Chairman: Dr. Walter F. O' Brien

(ABSTRACT)

An experimental investigation into the effects of inlet temperature transients on the stall and stall recovery aerodynamics of a low speed multi-stage axial flow compressor has been presented. Experiments were conducted on a low speed multi-stage axial flow compression system to demonstrate how a compressor dynamically stalls or recovers from a rotating stall operating condition during an inlet temperature transient. The specific effects of the inlet temperature transients on the compressor rotor blade flow physics during the dynamic stall or rotating stall recovery events of the axial flow compression system have been presented. In one experiment, a full recovery from a rotating stall operating condition was successfully accomplished on the low speed multi-stage axial flow compressor. Explanations for the axial flow compression system dynamic stall and rotating stall recovery processes during inlet temperature transients have been presented. The method utilized for inducing the rotating stall recovery on the compression system has been proposed as a possible new technique for active recovery from rotating stall for single and multi-stage axial flow compression systems.

ACKNOWLEDGMENTS

The author wishes to express sincere gratitude to Dr. Joseph Schetz, of the Aerospace and Ocean Engineering Department at Virginia Polytechnic Institute and State University, who provided the opportunity to attend graduate school. The author also wishes to express sincere gratitude to Dr. Walter F. O'Brien of the Mechanical Engineering Department for providing the funding, opportunity, and resources to conduct this research. The guidance, advice, and patience of the advisory committee is greatly appreciated. In particular, the author wishes to thank Dr. John Moore , Dr. Wing-fai Ng, Dr. Clinton Dancey, and Dr. Milton Davis for serving on the committee and for their discussions involving the fundamental principles associated with the development of this piece of research. The author also wishes to thank William T. Cousins at AlliedSignal Corporation for his discussions and assistance regarding experiments conducted in this piece of research. The support received from the Mechanical Engineering Department Machine Shop, which made the author's graduate study possible, is gratefully acknowledged. Finally, the author wishes to thank Mr. Frank Caldwell, of the Mechanical Engineering Department's Instrument Shop, who provided invaluable assistance in developing the necessary data acquisition systems and instrumentation for the experiment and also helped solve problems encountered with it.

TABLE OF CONTENT

	<u>Page</u>
TITLE	i
ABSTRACT	ii
ACKNOWLEDGMENTS	iii
TABLE OF CONTENT	iv
LIST OF FIGURES	viii
NOMENCLATURE	xv
1. INTRODUCTION	1
2. LITERATURE REVIEW	4
3. ENERGIZED COMPRESSION SYSTEM STALL AND RECOVERY THEORETICAL DEVELOPMENT	15
3.1 Compressor Map	15
3.1.1 Compressor Rotor Blade Velocity/Mach Number Triangles	17
3.1.2 The Stall Line	21
3.1.3 The Recovery Line	23
3.2 Effect Of Inlet Temperature Increase On Compressor Pressure Rise	25
3.3 Compression System Helmholtz Resonator Model	30
3.3.1 Differential Equation Of Motion	30
3.3.2 Solution To The Differential Equation Of Motion	38
3.4 Compression System Dynamic Response On Compressor Performance Map	42

TABLE OF CONTENT (continued)

	<u>Page</u>
3.5 Energized Compression System Rotating Stall And Recovery Hypotheses	45
3.5.1 Compression System Rotating Stall Hypothesis	46
3.5.2 Compression System Rotating Stall Recovery Hypothesis	48
3.6 Summary Of The Theory	50
4. DESCRIPTION OF EXPERIMENT	52
4.1 Test Cell	53
4.2 Compressor	53
4.3 Plenum Chamber	56
4.4 Throttle Valve	57
4.5 Inlet Duct System	58
4.6 Temperature Transient Generator	58
4.7 Fuel Delivery and Control	60
4.8 Instrumentation	61
4.8.1 Computer	61
4.8.2 Thermocouples	63
4.8.3 Pressure Transducers	66
5. DATA REDUCTION AND ANALYSIS	69
6. RESULTS AND DISCUSSION	76
6.1 Rotating Stall Recovery	77

TABLE OF CONTENT (continued)

	<u>Page</u>
6.2 No Rotating Stall Recovery	85
6.3 Rotating Stall	93
6.4 No Rotating Stall	101
6.5 Rotating Stall Followed By An Immediate Recovery	109
7. CONCLUSIONS AND SUMMARY	118
7.1 Conclusions	118
7.1.1 Rotating Stall Recovery Conclusions	120
7.1.2 Conclusions Related To The Development Of Stall	121
7.2 Summary	122
8. RECOMMENDATIONS AND FUTURE WORK	123
9. REFERENCES	127
10. APPENDIX A Experimental Data	131
11. APPENDIX B Instrument Calibration	167
12. APPENDIX C Mass Flow Measurement	171
13. APPENDIX D Uncertainty	179
13.1 Measurement Uncertainty Analysis	179
13.1.1 Uncertainty in Flow Density At Throttle Exit Plane	180
13.1.2 Uncertainty in Flow Velocity At Throttle Exit Plane	182
13.1.3 Uncertainty in Mass Flow Rate	185

TABLE OF CONTENT (continued)

	<u>Page</u>
13.2 Frequency Response Of Pressure Measurement Systems	188
14. APPENDIX E Instrumentation/Hardware	193
14.1 Computer/Data Acquisition System	193
14.2 Ignition System	195
14.3 Fuel/Fuel Control	195
14.4 Compressor Control	195
14.5 Thermocouples	196
14.6 Pressure Transducer	196
15. VITA	200

LIST OF FIGURES

	<u>Page</u>	
<u>Chapter 3</u>		
Figure 3.1	Compressor Performance Map	16
Figure 3.2	Blade Velocity Triangle	18
Figure 3.3	Blade Velocity/Mach Number Triangles	20
Figure 3.4	Closing The Throttle	22
Figure 3.5	Opening The Throttle	24
Figure 3.6	The Recovery Line	26
Figure 3.7	Compressor Response To Quasi-Steady Inlet Temperature Increase	27
Figure 3.8	Time History of Compressor Pressure Rise and Inlet Total Temperature During An Inlet Temperature Transient	28
Figure 3.9	Compression System Helmholtz Resonator Model	31
Figure 3.10	Compressor Duct Fluid Control Volume	32
Figure 3.11	Fluid Mass Free Body Diagram	34
Figure 3.12	Air-Tight Piston	35
Figure 3.13	Helmholtz Resonator Driven By An Inlet Temperature Transient	40
Figure 3.14	Helmholtz Resonator Undergoing Free Damped Response Oscillations	41
Figure 3.15	Conceptual Compression System Dynamic Response Paths	44
Figure 3.16	Compressor Dynamic Stall By Inlet Temperature Transient	47

LIST OF FIGURES (continued)

	<u>Page</u>
Figure 3.17 Compressor Dynamic Recovery From Rotating Stall By Inlet Temperature Transient	49
<u>Chapter 4</u>	
Figure 4.1 Test Facility	52
Figure 4.2 Test Cell	54
Figure 4.3 Two Stage Low Speed Compressor	55
Figure 4.4 RAF-Airfoil Section	55
Figure 4.5 Plenum Chamber	56
Figure 4.6 Throttle Valve	57
Figure 4.7 Inlet Duct	58
Figure 4.8 Temperature Transient Generator	59
Figure 4.9 Propane Tanks	60
Figure 4.10 Thermocouple Position (Compressor)	64
Figure 4.11 Thermocouple Position (Plenum)	65
Figure 4.12 Pressure Probe Position (Compressor)	67
Figure 4.13 Pressure Probe Position (Plenum)	68
<u>Chapter 5</u>	
Figure 5.1 Compression System Data Measuring Stations	70
Figure 5.2 Rotor Blade Chordline/Stagger Angle	75

LIST OF FIGURES (continued)

	<u>Page</u>
<u>Chapter 6</u>	
Figure 6.1 Compressor Performance Map (Overall) (Rotating Stall Recovery)	78
Figure 6.2 Axial Flow Mach Number and Inlet Temperature vs Time (Rotating Stall Recovery)	79
Figure 6.3 Rotor Mach Number and Inlet Temperature vs Time (Rotating Stall Recovery)	80
Figure 6.4 Blade Angle of Attack and Inlet Temperature vs Time (Rotating Stall Recovery)	81
Figure 6.5 Individual Stage Pressure Rise and Inlet Temperature vs Time (Rotating Stall Recovery)	82
Figure 6.6 Compressor Performance Map (Overall) (No Rotating Stall Recovery)	87
Figure 6.7 Axial Flow Mach Number and Inlet Temperature vs Time (No Rotating Stall Recovery)	88
Figure 6.8 Rotor Mach Number and Inlet Temperature vs Time (No Rotating Stall Recovery)	89
Figure 6.9 Blade Angle of Attack and Inlet Temperature vs Time (No Rotating Stall Recovery)	90
Figure 6.10 Individual Stage Pressure Rise and Inlet Temperature vs Time (No Rotating Stall Recovery)	91
Figure 6.11 Compressor Performance Map (Overall) (Stall)	94
Figure 6.12 Axial Flow Mach Number and Inlet Temperature vs Time (Stall)	95

LIST OF FIGURES (continued)

		<u>Page</u>
Figure 6.13	Rotor Mach Number and Inlet Temperature vs Time (Stall)	96
Figure 6.14	Blade Angle of Attack and Inlet Temperature vs Time (Stall)	97
Figure 6.15	Individual Stage Pressure Rise and Inlet Temperature vs Time (Stall)	98
Figure 6.16	Compressor Performance Map (Overall) (No Stall)	102
Figure 6.17	Axial Flow Mach Number and Inlet Temperature vs Time (No Stall)	103
Figure 6.18	Rotor Mach Number and Inlet Temperature vs Time (No Stall)	104
Figure 6.19	Blade Angle of Attack and Inlet Temperature vs Time (No Stall)	105
Figure 6.20	Individual Stage Pressure Rise and Inlet Temperature vs Time (No Stall)	106
Figure 6.21	Compressor Performance Map (Overall) (Stall Followed By Immediate Recovery)	110
Figure 6.22	Axial Flow Mach Number and Inlet Temperature vs Time (Stall Followed By Immediate Recovery)	111
Figure 6.23	Rotor Mach Number and Inlet Temperature vs Time (Stall Followed By Immediate Recovery)	112
Figure 6.24	Blade Angle of Attack and Inlet Temperature vs Time (Stall Followed By Immediate Recovery)	113
Figure 6.25	Individual Stage Pressure Rise and Inlet Temperature vs Time (Stall Followed By Immediate Recovery)	114

LIST OF FIGURES (continued)

	<u>Page</u>
<u>Chapter 10 (Appendix A)</u>	
Figure 10.1 Pressure Ratio and Inlet Temperature vs Time (Rotating Stall Recovery)	133
Figure 10.2 Corrected Mass Flow and Inlet Temperature vs Time (Rotating Stall Recovery)	134
Figure 10.3 Flow Density and Inlet Temperature vs Time (Rotating Stall Recovery)	135
Figure 10.4 Axial Flow Velocity and Inlet Temperature vs Time (Rotating Stall Recovery)	136
Figure 10.5 Blade Incidence and Inlet Temperature vs Time (Rotating Stall Recovery)	137
Figure 10.6 Throttle Area and Inlet Temperature vs Time (Rotating Stall Recovery)	138
Figure 10.7 Pressure Ratio and Inlet Temperature vs Time (No Rotating Stall Recovery)	140
Figure 10.8 Corrected Mass Flow and Inlet Temperature vs Time (No Rotating Stall Recovery)	141
Figure 10.9 Flow Density and Inlet Temperature vs Time (No Rotating Stall Recovery)	142
Figure 10.10 Axial Flow Velocity and Inlet Temperature vs Time (No Rotating Stall Recovery)	143
Figure 10.11 Blade Incidence and Inlet Temperature vs Time (No Rotating Stall Recovery)	144
Figure 10.12 Throttle Area and Inlet Temperature vs Time (No Rotating Stall Recovery)	145

LIST OF FIGURES (continued)

	<u>Page</u>
Figure 10.13 Pressure Ratio and Inlet Temperature vs Time (Stall)	147
Figure 10.14 Corrected Mass Flow and Inlet Temperature vs Time (Stall)	148
Figure 10.15 Flow Density and Inlet Temperature vs Time (Stall)	149
Figure 10.16 Axial Flow Velocity and Inlet Temperature vs Time (Stall)	150
Figure 10.17 Blade Incidence and Inlet Temperature vs Time (Stall)	151
Figure 10.18 Throttle Area and Inlet Temperature vs Time (Stall)	152
Figure 10.19 Pressure Ratio and Inlet Temperature vs Time (No Stall)	154
Figure 10.20 Corrected Mass Flow and Inlet Temperature vs Time (No Stall)	155
Figure 10.21 Flow Density and Inlet Temperature vs Time (No Stall)	156
Figure 10.22 Axial Flow Velocity and Inlet Temperature vs Time (No Stall)	157
Figure 10.23 Blade Incidence and Inlet Temperature vs Time (No Stall)	158
Figure 10.24 Throttle Area and Inlet Temperature vs Time (No Stall)	159
Figure 10.25 Pressure Ratio and Inlet Temperature vs Time (Stall Followed By Immediate Recovery)	161

LIST OF FIGURES (continued)

	<u>Page</u>
Figure 10.26 Corrected Mass Flow and Inlet Temperature vs Time (Stall Followed By Immediate Recovery)	162
Figure 10.27 Flow Density and Inlet Temperature vs Time (Stall Followed By Immediate Recovery)	163
Figure 10.28 Axial Flow Velocity and Inlet Temperature vs Time (Stall Followed By Immediate Recovery)	164
Figure 10.29 Blade Incidence and Inlet Temperature vs Time (Stall Followed By Immediate Recovery)	165
Figure 10.30 Throttle Area and Inlet Temperature vs Time (Stall Followed By Immediate Recovery)	166
 <u>Chapter 11 (Appendix B)</u>	
Figure 11.1 Pressure Transducer Calibration Apparatus	168
 <u>Chapter 12 (Appendix C)</u>	
Figure 12.1 Compressor and Plenum Chamber Control Volume	172
 <u>Chapter 13 (Appendix D)</u>	
Figure 13.1 Frequency Response Of Pressure Measurement Systems	190

NOMENCLATURE

A	area
a	isentropic speed of sound
c	stiffness
dB	decibel
F	force
k	wave number
L	compressor duct length
m	mass
\dot{m}	mass flow rate
Mu	rotor Mach Number
Mv	axial flow Mach Number
Mw	relative Mach Number
N	rotor mechanical speed (% of design)
P	static pressure
Pa	ambient pressure
P0	total pressure
P01	compressor inlet total pressure
P02	total pressure across stage 1
P03	total pressure across stage 2

NOMENCLATURE (continued)

P_{actual}	actual pressure
P_{measured}	measured pressure
P_{min}	minimum absolute level of pressure
P_{ref}	reference pressure
P_{ss}	steady state pressure
p	acoustic pressure
r	compressor duct radius
R	ideal gas constant
\mathcal{R}	radiation resistance
s	entropy
t	time
T	static temperature
T_a	ambient temperature
T_0	total temperature
T_{01}	compressor inlet total temperature
T_{02}	total temperature across stage 1
T_{max}	maximum absolute level of temperature
T_{ref}	reference temperature
U	rotor velocity

NOMENCLATURE (continued)

V	absolute flow velocity
Vol	plenum volume
W	relative velocity
x	x-direction of Cartesian coordinate system
y	y-direction of Cartesian coordinate system
Z	uncertainty

Greek Math Symbols

α	angle of attack
β	incidence angle
γ	ratio of specific heats
ξ	stagger angle
ϕ	phase angle
ρ	density
ω	driving frequency
Ω	angular velocity

NOMENCLATURE (continued)

Subscripts

1	static conditions at compressor stage 1 inlet
01	total conditions at compressor stage 1 inlet
2	static conditions at compressor stage 2 inlet
02	total conditions at compressor stage 2 inlet
ave	arithmetic average
C	compressor
eff	effective
in	properties flowing into fluid control volume
mean	mean radius of compressor
out	properties flowing out of fluid control volume
P	plenum
ref	reference
T	throttle exit plane
x	axial direction
x1	axial direction at compressor stage 1 inlet
x2	axial direction at compressor stage 2 inlet

NOMENCLATURE (continued)

ACRONYMS

AEDC	Arnold Engineering Development Center
AIP	Aerodynamic Interface Plane
ARP	Aerospace Recommended Practice
ATM	Atmosphere
ETF	Engine Test Facility
MEGI	Missile Exhaust Gas Ingestion
NACA	National Advisory Committee For Aeronautics
NASA	National Aeronautics And Space Administration
PWT	Propulsion Wind Tunnel
STOL	Short Takeoff And Landing
VTOL	Vertical Takeoff And Landing

1. INTRODUCTION

The problem of aircraft gas turbine engine axial flow fan and compressor performance loss and stall due to the ingestion of rocket exhaust gas, gun gas, or engine exhaust gas reingestion has been recognized for years. It is well known that changes in the temperature and chemical composition of compressor inlet flows affect compressor operation. However, there is no documentation in the literature that discusses the fundamentals of fan and compressor stall and stall recovery aerodynamics during these particular events. This is probably due to the fact that the historical remedial measures were to locate the aircraft ordnance such that the armament exhaust gases never approached the engine inlet. Also, engine nozzles and inlets were carefully designed with gas deflectors such that the recirculation and reingestion of engine exhaust gases was minimized. The implementation of these airframe remedial measures, for this particular propulsion system problem, deterred any efforts to understand the aerodynamic phenomena that occurred in the fan and compressor during the hot gas ingestion event.

In view of the technological developments of more maneuverable fighter aircraft and VTOL/STOL aircraft, the need to understand the effects of temperature disturbances on the stall and stall recovery aerodynamics of gas turbine fans and compressors becomes more evident. The effects of thrust vectoring, thrust reverser gas ingestion, and exhaust gas reingestion during fixed wing or rotary-wing VTOL/STOL operation in close proximity to the ground are examples of reasons to understand this particular field more thoroughly. Also, the development of stealth technology aircraft, requiring ordnance to be

stored in an internal weapons bay inside the aircraft fuselage, revisits the problem of positioning armament in proximity of the engine inlet and makes the avoidance technique impossible.

Temperature flow disturbances are caused by the ingestion of exhaust gases from armament firings such as guns, rockets, and missiles. Also, reingestion of gas turbine engine exhaust gases in fixed wing and rotary-wing VTOL/STOL aircraft are other common sources. These temperature disturbances vary the chemical composition and reduce the density of the gas being compressed by the fan or compressor, causing the fan and compressor to stall. The stall/flameout phenomenon is caused by a severe transient mismatch of the compressor stages. Since the overall compressor characteristics are actually a composite of each individual stage, it is necessary for only one stage to be driven to a flow breakdown situation by a temperature transient. When a flow breakdown and reversal does occur at one stage, or more likely a group of stages, the probable result is rotating stall or surge in the compressor and subsequent flame-out of the engine.

Axial flow fans and compressors are vulnerable to the phenomenon of rotating stall. Rotating stall is an operational condition where a localized circumferential portion of the compressor rotor operates stalled and the overall performance is reduced. It is a globally stable, but locally dynamic operational mode that makes the compressor operate at a lower efficiency and pressure rise for a given rotor mechanical speed. Rotating stall that occurs in the axial flow fan or compressor of an aircraft gas turbine engine causes a

complete malfunctioning of the propulsion system. The consequences of a complete propulsion system malfunction for an aircraft in flight can be catastrophic.

Manifestations of a rotating stall operating condition are a rapid increase in engine exhaust gas temperature, engine pressure ratio decrease or fluctuation, vibration caused by fan or compressor pressure pulsation, fluctuation in rotor RPM, and poor engine response to throttle movements. Severe compressor rotating stalls cause loud noise, may be accompanied by fire, vapor, or smoke in the engine exhaust and/or engine inlet, and lead to excessive fan or compressor rotor blade vibration which can induce structural failure. Therefore, methods or techniques for prevention of and recovery from rotating stall are of considerable interest.

2. LITERATURE REVIEW

The topic of this dissertation is the effects of inlet temperature transients on the stall and stall recovery aerodynamics of axial flow compression systems. After conducting a careful search, previous fundamental treatments of the effects of inlet temperature transients on axial flow compression system stall and stall recovery aerodynamics were not found. The literature contains many references discussing operational effects of inlet temperature transients on the compressor and complete gas turbine engine systems. Therefore, the literature review addresses these particular operational effects.

The problem of axial flow fan and compressor stall or combustor flameout, due to rocket exhaust gas or gun gas ingestion into the aircraft engine, has been recognized for years. Temperature ramps of up to 36,000 degrees F/sec, with peak temperatures of 1100 degrees (F) at engine inlets aligned with the flight path of air launched missiles (Sidewinder, Zuni, etc.), have been documented. The temperature rise time for a single rocket firing was observed to be 0.1 to 0.2 seconds, while the decay to ambient inlet temperature generally took 0.2 to 0.4 seconds. The rail launch method, for launching the missile from the aircraft, appeared to be a factor in the severe temperature ramps because of the very close proximity of the engine inlet to the missile exhaust plume. Experimental studies of rocket exhaust gas ingestion by simulation in engine test cells revealed that the stall/flameout temperature ramp is different for each engine /inlet combination. Other phenomena associated with gas ingestion are supersonic inlet unstarts, temporary engine control anomalies, and deposition of solid rocket particulates on engine internal components.

Wells [1] conducted a survey of hot gas ingestion simulation techniques for the United States Air Force Arnold Engineering Development Center. Five different techniques were examined and evaluated for simulating hot gas ingestion into gas turbine engines. Evaluation criteria involved the simulation quality of actual air to air rocket firing characteristics. A comparison was made between all five simulation techniques with emphasis on the generated temperature ramp, pressure pulse, gas chemical composition, and temperature distortion. Emphasis also was placed upon required resources and whether or not the simulation technique satisfied military specifications.

The first hot gas ingestion simulation technique investigated was the missile exhaust gas ingestion (MEGI) simulator developed at the Naval Air Propulsion Test Center. The simulator was designed to burn specially fabricated grains of rocket propellant in a boiler-plate motor capable of producing up to 30 lbm/sec exhaust gas flow for 0.1 seconds. The grains were designed and developed at the Naval Ordnance Station at Indian Head, Maryland and were made with either double base (Zuni missile) or composite (Sparrow, Sidewinder) formulation. The rig accurately simulated engine encountered temperature ramps and gas chemical composition but was unable to produce controlled spatial temperature distortion. Also, the burning of the rocket propellant grains produced corrosive agents HCL and AL_2O_3 solid particulates that attached to and damaged engine internal components.

The second hot gas ingestion simulation technique investigated was a four-quadrant segmented hydrogen burner used at the NASA Lewis Research Center. The segmented burner was installed upstream of a gas turbine engine and was designed to produce spatial temperature distortion as well as time-dependent temperature variations at the engine inlet. It utilized fuel injectors and V-gutter flameholders with swirl can ignitors. The rig produced adequate temperature ramps (up to 17,750 R/sec) but had the

disadvantage of requiring a fuel supply and control system. It also experienced ignition problems at pressures and temperatures associated with high altitude flight conditions. Also, the correct gas chemical composition was not simulated.

The third hot gas ingestion simulation technique investigated was a pivoting nozzle mounted in the propulsion wind tunnel (PWT) at the Arnold Engineering Development Center (AEDC). This simulator discharged heated gaseous nitrogen into the wind tunnel flow toward the inlet/engine model. A tactical missile launch could be simulated by sweeping the hot gas plume across the inlet. Significant findings, resulting from tests conducted with this hot gas ingestion simulation technique, were that the presence of an inlet system in front of the engine can have a significant effect on the transient temperature characteristics at the engine face. Also, the nitrogen heated to a temperature of 1200 (R) was insufficient to provide required temperature ramps. A rocket motor was recommended for full scale testing.

The fourth hot gas ingestion simulation technique investigated represented a significant but incomplete effort to establish a rocket exhaust gas ingestion simulation capability at the Engine Test Facility (ETF) at AEDC in 1971. At the time it appeared that the rocket exhaust gas ingestion capability of the F-100 engine was to be demonstrated in a qualification test program. The requirement was dropped, however, in early 1972. The basic approach was to construct a turnstile mount that supported four small solid rocket motors, mounted in a wind tunnel in the Engine Test Facility at AEDC. The proposed technique was of course susceptible to the same shortcomings as the Naval Air Propulsion Test Center hot gas ingestion simulation concept.

The fifth hot gas ingestion simulation technique investigated was the converted Engine Test Facility airjet pressure distortion generator. The airjet system was converted to inject high temperature compressed air into the engine inlet with minor hardware

modifications. This approach was particularly well adapted to producing controlled spatial temperature distortion. However, temperature ramps produced were inadequate and the gas chemical composition was incorrect.

The conclusion of the hot gas ingestion simulation survey, for the AEDC, recommended that the Engine Test Facility adapt the turnstile rocket motor mount technique for a hot gas ingestion simulation capability. This technique was considered to be the most practical and cost effective method to simulate the temperature ramps encountered at the engine inlet during the launch of tactical missiles.

Childs, Kochendorfer, Lubick, and Friedman [2] set out to determine the actual temperature profiles at the inlet of an aircraft flying at high altitudes, after the launching of an air to air rocket and the firing of cannons. Their investigation led to the identification of specific effects on the compressor and combustor, during the firing of armament at high altitudes. These results involved actual temperature increments measured at the inlet, during the firing of armament. Other results include temperature distortion effects on the compressor map and combustion stability limits during the ingestion of combustibles into the engine.

They determined that the main sources of temperature distortion for gas turbine engines were the ingestion of exhaust gases from armament firings such as guns, rockets, and missiles. Other sources include engine exhaust gas reingestion from VTOL/STOL aircraft, helicopters, thrust reversing operations, and hot steam ingestion from catapult launches from aircraft carriers. They determined that following engine inlet effects will occur during the firing of armament or engine exhaust gas reingestion:

- 1) Increased inlet temperatures
- 2) Entry of combustibles into the engine

3) Reduced oxygen content in the gases entering the engine

The effect of temperature distortion, in terms of the entire compressor, was to effectively lower the surge line and to shift the operating point to the left to a lower corrected rotor speed on the compressor map.

They examined the exhaust flow of a 2.75 inch air to air rocket. The rocket had a combustion chamber pressure and temperature of 1100 psi and 4500 (R) respectively. It had a design exit Mach number of 2.7 and a design exit static pressure of 42 psi. It was determined that this pressure was considerably above the ambient pressure at altitude and that the exhaust plume expanded greatly upon leaving the nozzle. Data were obtained from the plume of a single rocket launched from an aircraft moving at Mach 0.9 at an altitude of 45,000 feet. At approximately 0.3 seconds after the firing, the rocket was 60 feet in front of the launch station and was moving away at a velocity of 400 ft/sec. Contours of temperature were obtained for the exhaust plume of the rocket. These temperatures were expressed as the difference in temperatures at various locations in the plume, and the ambient temperature. The location of the inlet relative to the launch station was known and temperature increments at the inlet were estimated.

The average temperature of the incoming air was found to be approximately 200 (C) above the ambient. The spatial temperature gradient varied from 260 (C) at the inner wall of the inlet to 140 (C) on the outer wall. They also investigated the effects of an aircraft in the process of firing cannons. It was determined that as the muzzle gases moved out ahead of the inlet, the gases mixed with the incoming air and the inlet temperature was increased. An additional effect was muzzle flash which is a sudden burning or explosion of the gases in front of the guns. It was found that when this occurs,

the hot gases expand in front of the aircraft and enter the engine at greater than normal rates.

Braithwaite, Garber, and Mehalic at the NASA Lewis Research Center [3] quantified steady state pressure, temperature, and combined pressure and temperature distortions with a simplified parallel compressor theory mathematical model. They obtained steady state pressure, temperature, and combined pressure and temperature distortion data on a General Electric J-85 eight stage turbojet engine. Specifically, they examined the effects of the steady state distortions on the compressor stall margin. From the data, and with the aid of parallel compressor theory, they derived the theoretical performance of the J-85 when subjected to pressure and temperature distortions.

Results from the investigation revealed that pressure and temperature distortion reduce compressor stall margin. They demonstrated that as pressure or temperature distortion intensity increased, compressor stall margin decreased. They also concluded that the relative orientation of the distortion patterns during combined pressure and temperature distortion, affect loss of compressor stall margin differently. Specifically, if the distortions overlapped, the loss in compressor stall margin was greatest. If the distortions were directly opposed from each other, then the loss in compressor stall margin was minimal. They postulated from these results that the detrimental effects of a steady state pressure distortion on compressor stall margin could be reduced by imposing a steady state temperature distortion directly opposite the pressure distortion. They also postulated that the reverse of this situation was true.

The Society of Automotive Engineers Aerospace Resource Document [4] discussed the inlet temperature distortion problem. It also discussed some of the past and present temperature distortion work. It indicated that the sources of temperature distortion that are of concern are weapons wake ingestion, STOL/VTOL hot gas reingestion, thrust

reverser exhaust ingestion, and steam ingestion. Helicopter flight tests were conducted with a CH-47 and YUH-61A to determine the effect of reingesting hot exhaust gases. Inlet temperatures of 610 (R) were reached and resulted in a decrease in horsepower. Understanding of reingestion during hover was gained by testing a 1/15th scale model. Primary design variables were nozzle area, inboard blade geometry, and engine location. Based on these tests, an optimum design was chosen for full-scale production aircraft.

A modern helicopter engine, the T-700, was subjected to temperature distortion. Part of the test consisted of placing an inlet temperature sensor in the engine inlet. When the sensor detected either hot or cold distorted flow, a control adjusted the fuel flow and varied the geometry accordingly to change the compressor surge margin.

Hot gas reingestion in the AV-8B V/STOL aircraft was found to be within the tolerance of the compression system. However, the proposed use of plenum chamber burning in the fan duct will increase the temperature of any ingested gas. The airframe and engine manufacturers have conducted rig and full-scale tests of various nozzle, inlet, and mechanical deflector designs in an attempt to reduce the levels of hot gas reingestion. Laboratory test data was produced by the NASA Lewis hydrogen-fueled temperature distortion generator.

Wallner, Useller, and Saari [5] conducted extensive wind tunnel experiments to learn why inlet temperature transients disturb the operation of turbojet engines. Rapid temperature increases were applied across the inlet of two turbojet engines over a wide range of altitudes, temperature ramp rates, and engine speeds. High response instrumentation was used to evaluate compressor performance during the temperature transients. At all altitudes investigated, compressor stall was induced by a rapid temperature transient on both engines. Compressor stall was induced by consistently smaller temperature transients as altitude was increased. They also noted that this altitude

effect becomes important at high altitudes because combustor blowout occurred from the pressure pulsations of the stalled compressor.

It was found that internal flow changes within the axial flow compressor lagged considerably behind the rapid inlet temperature transient. This lag caused a transient mismatch of the stages because the compressor was not able to adjust to the rapidly changing flow conditions resulting from the temperature transients. An attempt was made to alleviate compressor stall resulting from rapid temperature transients. It was found that the only remedial action that afforded any measure of relief from the temperature induced stalls was a sudden reduction in engine fuel flow just prior to the temperature increase. This technique shifts the operating point so as to lower the compressor pressure ratio and thus increase the stall margin.

Mehalic and Lottig [6] investigated the effects of circumferential and radial temperature distortions and combined temperature and pressure distortion on the performance of a J85-GE-13 turbojet engine. The loss of compressor stall pressure ratio at constant speed was used to determine the severity of the various distortions and combination of distortions tested. They concluded that the most severe pattern of temperature distortion was a hub radial while a circumferential pattern of diametrically opposed sectors was least severe. Combined pressure and temperature distortion effects were dependent upon the location of the high temperature and low pressure regions. The largest stall pressure ratio loss occurred when these two regions overlapped. The least stall pressure ratio loss occurred when these two regions were directly opposed.

Rudey and Antl [7] examined the effects of inlet temperature distortion on the performance of a turbofan engine compressor system. The turbofan engine was experimentally subjected to spatial and time dependent inlet temperature distortions in an altitude test facility at the NASA Lewis Research Center. A gaseous hydrogen fueled

burner was used to produce the distortions. The purpose of the investigation was to determine the effects of circumferential extent, magnitude, and rate of change in inlet temperature on the compressor system stability margin.

It was found that the high pressure compressor was more sensitive than the fan. They concluded that the main parameter affecting compressor stability margin was the magnitude for spatial distortions and the time rate of change for time dependent distortions. The high pressure compressor was more sensitive than the fan to both spatial and transient temperature distortions. They hypothesized that the high pressure compressor was more sensitive than the fan because of characteristics related to the hydrogen burner. Specifically, the hottest and most rapidly changing temperatures, which occurred in the center of the burner, were ingested by the core compressor, producing high pressure compressor stalls but not fan stalls. The loss in high pressure compressor stall margin was found to be more dependent upon magnitude than circumferential extent for spatial temperature distortion. However, the time rate of change in engine inlet temperature, during a temperature transient, had a more pronounced effect than did either the circumferential extent or absolute level of temperature obtained during a transient. No determinable reduction in stall margin of the fan was established because core compressor stalls occurred before fan stalls.

Abdelwahab [8] conducted an experimental investigation to determine the effects of fan inlet temperature disturbances on the stability of a turbofan engine. A TF30-P-3 turbofan was used to conduct the investigation at the NASA Lewis Research Center. All tests were conducted with a 90 degree circumferential extent of the fan inlet exposed to above average temperatures. Temperature disturbances were induced by a gaseous fueled burner installed upstream of the fan inlet. During increasing levels of steady state temperature distortion, stall initiated in the high pressure compressor when a critical stage

reached its stall temperature rise limit. During temperature transients, inlet temperature ramps and rise magnitudes were as high as 20,000 K/sec and 300 K. During low inlet temperature transients and rises, compression system response was similar to the steady state temperature distortion compressor response because stall initiated in the high pressure compressor. During high inlet temperature transients and rise magnitudes, stall initiated in the fan.

Davis [9] evaluated flight test data for the A-10 to determine causes of engine instability problems while ingesting gun exhaust gases. The flight vehicle was a Fairchild Republic A-10 which has a nose mounted General Electric GAU-8/A Avenger 30 mm seven barrel cannon as its main armament system. The cannon is offset slightly to port to allow firing of each rotating barrel on the centerline of the aircraft. The cannon has two firing rates, high rate of 4,200 rounds/minute and low rate of 2,100 rounds/minute. The engine is a TF34-GE-100 dual rotor, nonaugmented turbofan engine. The compression system consists of a single stage fan and a 14 stage axial flow compressor. High response instrumentation was mounted throughout the engine and in the engine inlet system to measure pressures and temperatures. Conclusions were based upon two A-10 flight tests in which nine surge events occurred during the firing of the GAU-8/A cannon.

It was determined that the high pressure compressor of the TF34 was most affected during the ingestion of the gun exhaust gases. The rapid temperature change at the compressor inlet, due to the hot gas ingestion, was the likely cause of the high pressure compressor surges. Evidence of circumferential temperature distortion at the engine inlet was found with the most severe temperature gradients passing through the portion of the fan nearest the fuselage. Radial variations in temperature were found at the compressor inlet with the hottest gases in the hub area.

Conclusions From Literature Review

It is evident that research and experiments have been conducted to determine how inlet temperature transients and distortion affect overall gas turbine engine performance. However, few references exist in the literature that address the specific effects of inlet temperature transients or distortion on gas turbine engine fan and compressor stall or recovery aerodynamics. Specifically, there does not exist in the literature, any discussion or development of the blade flow physics associated with fan and compressor stall, or recovery during an inlet temperature transient or distortion. Therefore, the objective of this dissertation is to address the specific effects of a temperature transient on the stall and stall recovery processes of an axial flow compression system by examination of the blade flow physics.

There is currently strong interest in methods for active control of compressor stall. Previous methods for stall control involve opening compressor bleed doors, using variable geometry stator blades, and sudden reductions in fuel flow rate. These techniques shift the operating point so as to lower the compressor pressure ratio and increase the stall margin. These particular stall control methods such as the method utilized by Day (18), concentrate on means to interfere with the development of rotating stall and following surge.

The present investigation deals with recovery from an already-existing rotating stall operating condition, as well as the effects of thermal inputs on the development of stall. Thus the previous work is not directly related to previous investigations of stall control, neither in intent or in methods. However, the potential for utilization of thermal inputs for the prevention of stall development (i.e., active stall control) should not be ignored. Future investigation is recommended.

3. ENERGIZED COMPRESSION SYSTEM STALL AND RECOVERY

THEORETICAL DEVELOPMENT

The addition of energy to a compression system in the form of transient inlet temperature excursions energizes a dynamic response from the compression system, resulting in variations in flow angle of attack relative to the blades. Depending upon the initial operating condition of the compression system, these variations in flow angle of attack can induce compressor rotating stall or recovery. This section discusses the effects of quasi-steady changes on the compressor performance map, followed by a conceptual discussion of the excitation of a dynamic response from a compression system with an inlet temperature transient. Finally, the section concludes with a discussion of how an inlet temperature transient can induce either rotating stall or rotating stall recovery in a compression system.

3.1 The Compressor Map

Compression system steady state performance is quantified on a nondimensional plot called a compressor map or performance map as displayed in Figure 3.1. The performance map is a plot of compressor pressure rise versus mass flow in nondimensional form. The relationship of pressure rise to mass flow is characterized for different compressor mechanical speeds. An operating point on any particular speed

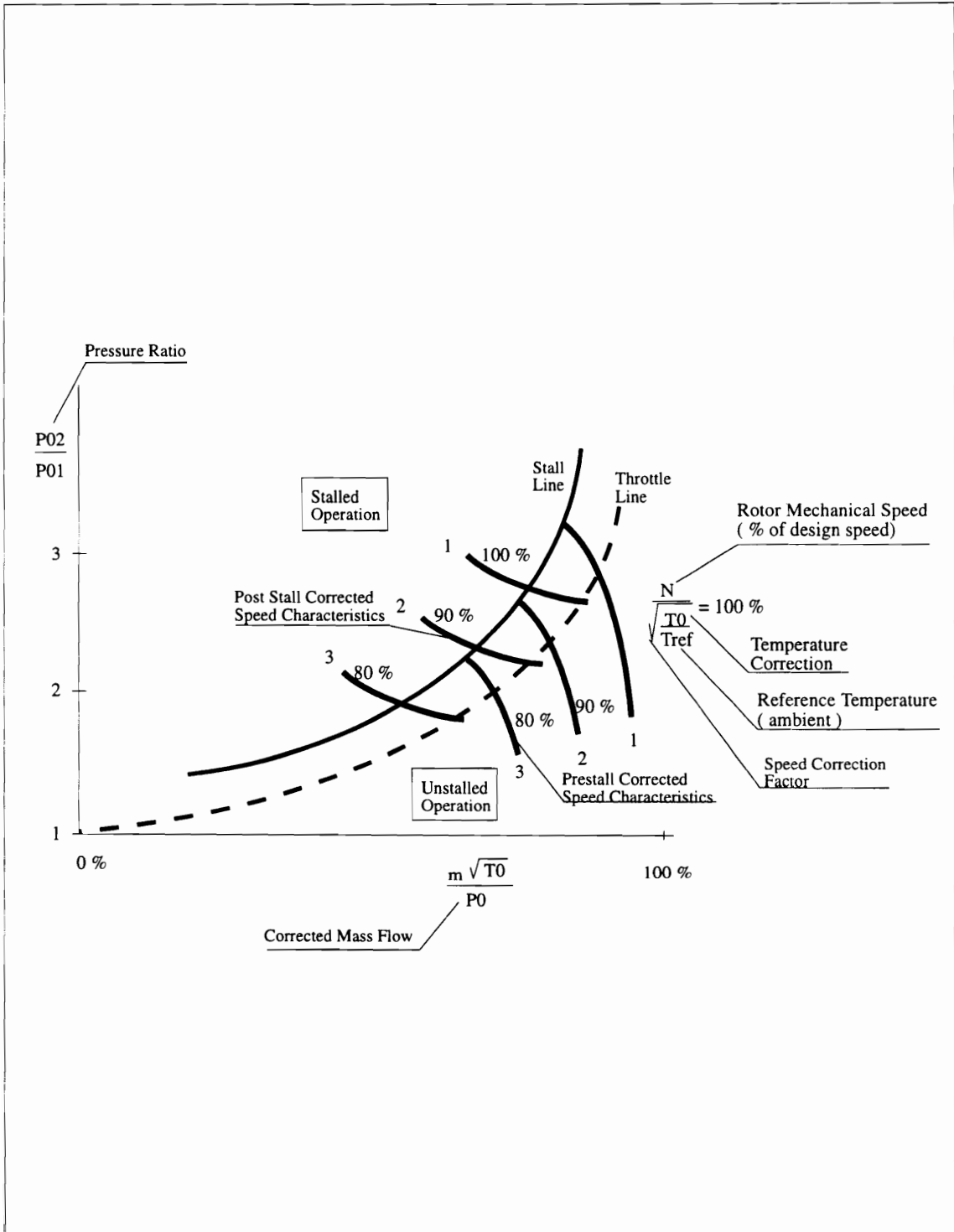


Figure 3.1 Compressor Performance Map

characteristic identifies the global relationship of pressure rise across the compressor to the amount of mass flow passing through the compressor to obtain that particular pressure rise. The speed characteristics are corrected with the compressor inlet total temperature, while the mass flow rate is corrected with the compressor inlet total pressure and total temperature.

The correction of the speed characteristics and the mass flow rate allows for flow density variations to be taken into account. This becomes significant when the temperature of the working fluid changes. The correction of the speed characteristics and the mass flow rate converts these two parameters into quantities that are analogous to compressor rotor Mach number and axial flow Mach number respectively. This ensures that the compressor blade velocity triangles remain similar for all operating conditions covered by a pair of values for corrected speed and corrected mass flow rate.

3.1.1 Compressor Rotor Blade Velocity/Mach Number Triangles

The velocity triangle for a compressor stage rotor blade is shown in Figure 3.2. The blade incidence is conventionally calculated from the velocities according to equation (3.1)

$$\beta = \tan^{-1} \left[\frac{U}{V_x} \right] \quad (3.1)$$

Blade Velocity Triangle

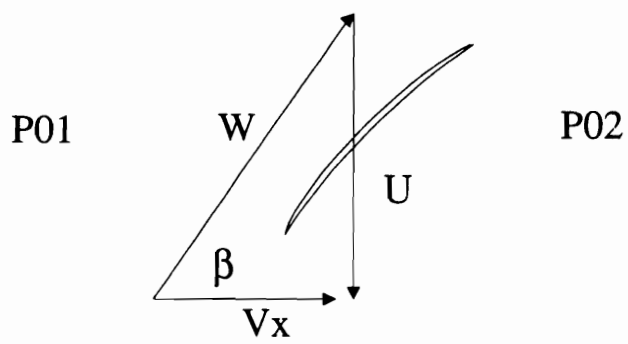


Figure 3.2 Blade Velocity Triangle

where U is the rotor velocity at a given blade radius and V_x is the axial flow velocity at that same blade radius. Equation (3.1) applies at any radius along the entire blade span for each individual stage of a compressor.

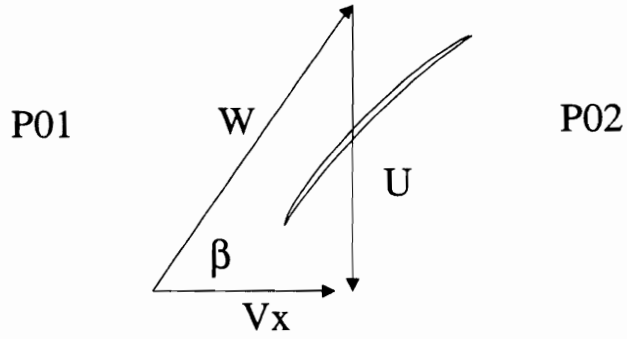
To account for compressibility effects associated with gas temperature changes, the velocities in the compressor blade velocity triangle are converted to Mach numbers. Figure 3.3 depicts a conventional compressor blade velocity triangle developed in terms of Mach numbers. The concept of a compressor blade Mach number triangle can be interpreted as a compressible blade velocity triangle. In addition to flow velocities, the blade Mach number triangle allows for flow density variations that are associated with flow temperature changes to be taken into account.

The concept of using Mach numbers in place of velocities can also be applied to the calculation of compressor stage rotor blade incidence. Equation (3.1) can be modified such that the blade incidence is calculated in terms of Mach numbers according to equation (3.2)

$$\beta = \tan^{-1} \left[\frac{Mu}{Mv_x} \right] \quad (3.2)$$

where Mu is the rotor Mach number at a given blade radius and Mv_x is the axial flow Mach number at that same blade radius. Equation (3.2) also applies at any radius along the entire blade span for each individual stage of a compressor. It analytically relates rotor blade incidence to not only velocity, as in equation (3.1), but also to the flow density variations that are produced by flow temperature changes.

Blade Velocity Triangle



Blade Mach Number Triangle

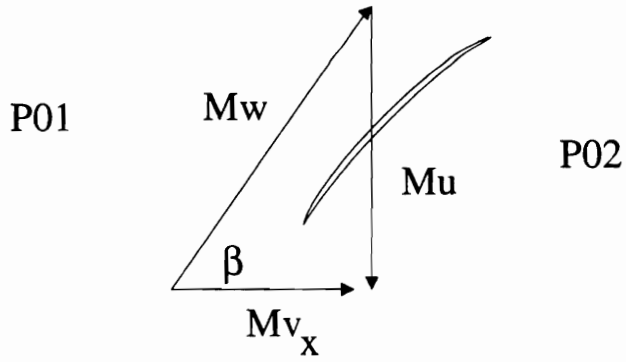


Figure 3.3 Blade Velocity/Mach Number Triangles

3.1.2 The Stall Line

Compressor speed characteristics are referred to as pre-and post-stall corrected speed characteristics. Figure 3.4 demonstrates that closing the throttle moves the operating point, initially at point (A), along the prestall corrected speed characteristic towards the left. This causes compressor pressure ratio to increase while decreasing the corrected mass flow passing through the compression system. The decreasing corrected mass flow rate translates into a decreasing axial flow Mach number. If the rotor mechanical speed and inlet temperature remain constant during this process, the rotor Mach number also remains constant. This causes an increase in blade incidence as shown by equation (3.2) and the blade Mach number triangles in Figure 3.4. When the operating point reaches the end of the prestall corrected speed characteristic at point (B), the blade incidence has been increased sufficiently to cause stall. Following stall, the operating point spontaneously moves to the corresponding post-stall corrected speed characteristic at point (C) as shown in Figure 3.4. This phenomenon occurs with all of the prestall corrected speed characteristics on the compressor performance map.

A line is introduced on the compressor performance map that connects the stall points associated with all of the prestall corrected speed characteristics. This line is called the **stall line** as shown in Figure 3.4 and represents the locus of stall points where the compressor stalls for the various corrected speeds. The compressor stalls if the operating point reaches or drifts beyond this line.

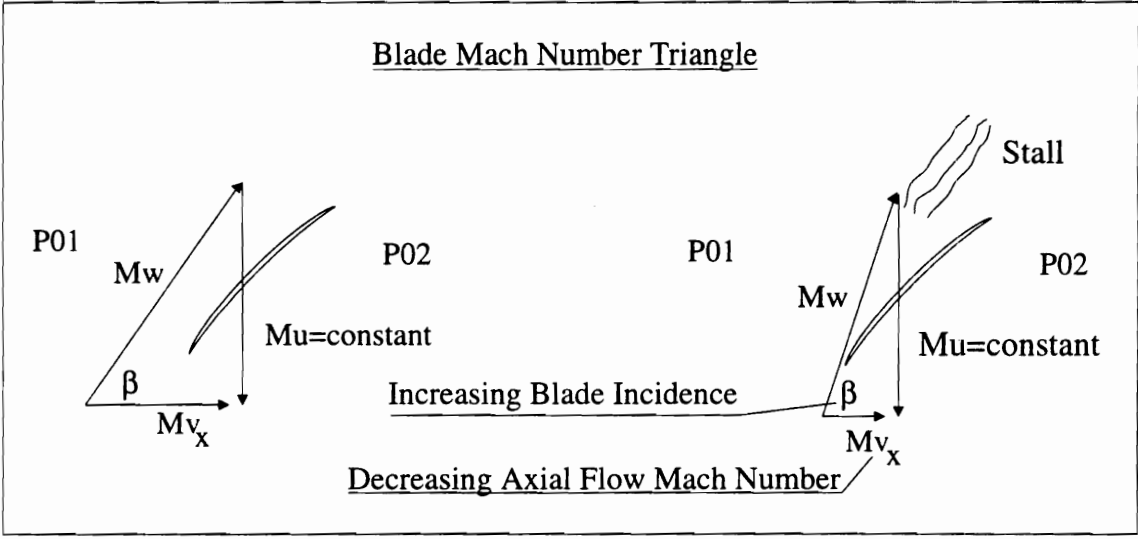
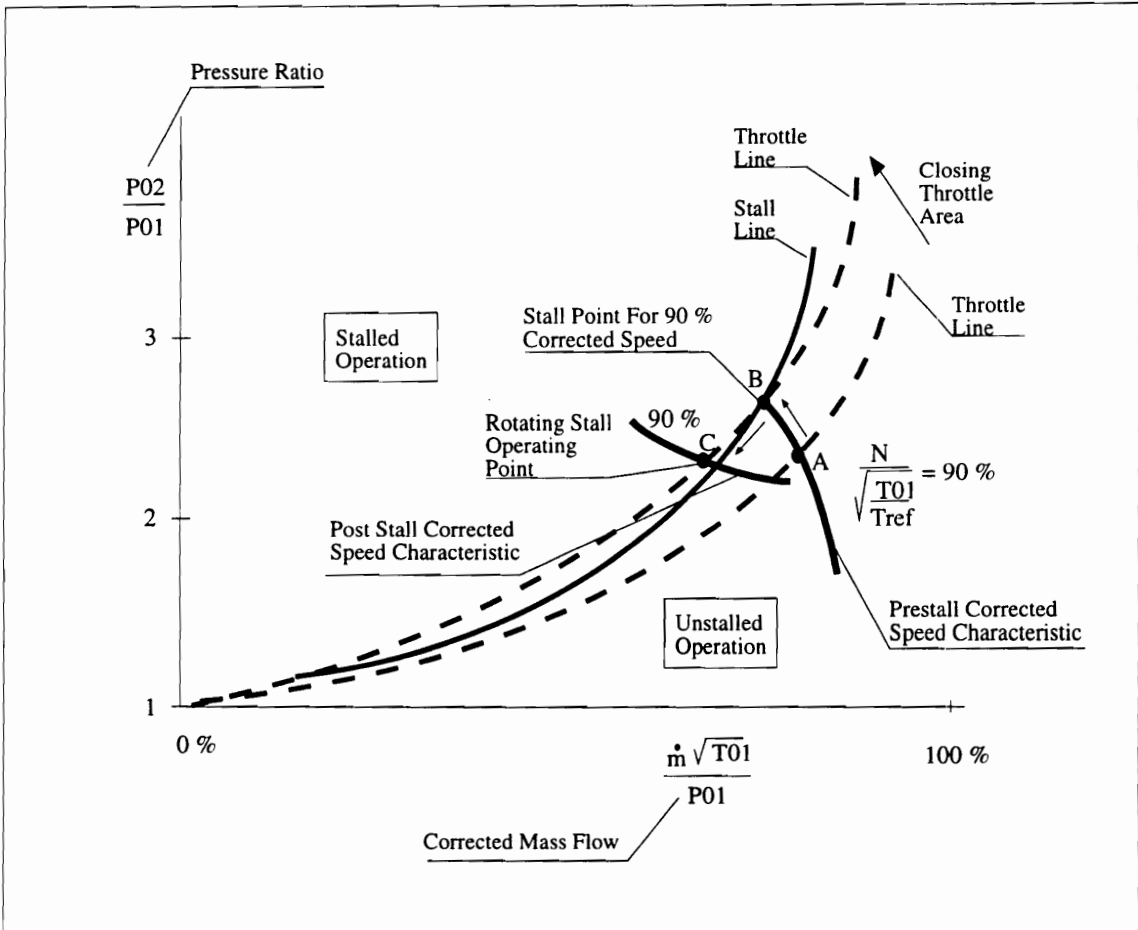


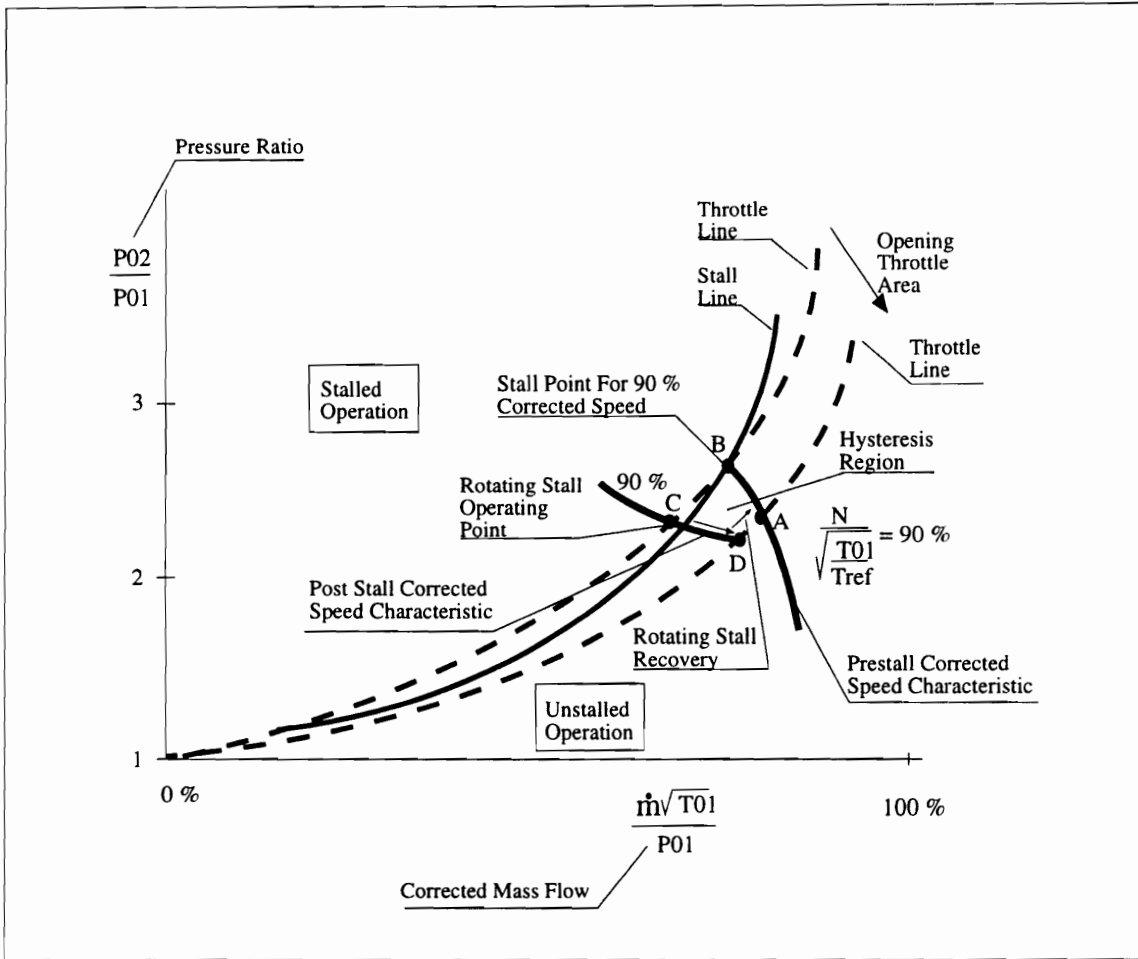
Figure 3.4 Closing The Throttle

3.1.3 The Recovery Line

Each prestall corrected speed characteristic has a corresponding post-stall corrected speed characteristic as shown for the three speeds in Figure 3.1. The post-stall corrected speed characteristics identify the global relationship between compressor pressure rise and mass flow rate when the compressor is in rotating stall operation. Following stall, opening the throttle moves the operating point along the post-stall corrected speed characteristic from point (C) towards the right as shown in Figure 3.5. This allows the corrected mass flow rate to increase through the compression system and increases the axial flow Mach number.

If the rotor mechanical speed and inlet temperature remain constant during this process, the rotor Mach number also remains constant. This causes a decrease in blade incidence as shown by equation (3.2) and the blade Mach number triangles in Figure 3.5. When the operating point reaches the end of the post-stall corrected speed characteristic at point (D), the blade incidence has been reduced sufficiently to allow the stalled flow to reattach to the blade surface. The operating point spontaneously returns to the corresponding prestall corrected speed characteristic to point (A) as shown in Figure 3.5. This phenomenon occurs with all of the post-stall corrected speed characteristics on the compressor performance map.

A new line is introduced on the compressor performance map that connects the rotating stall recovery points associated with all of the post-stall corrected speed



Blade Mach Number Triangle

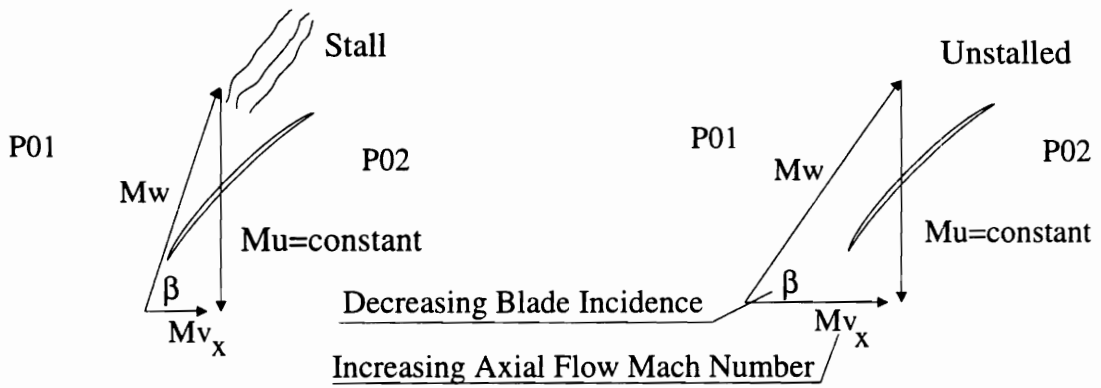


Figure 3.5 Opening The Throttle

characteristics and is called the **recovery line** as shown in Figure 3.6. The recovery line is analogous to the stall line, because the recovery line represents the locus of recovery points where the compressor will recover from rotating stall operation if the operating point reaches or drifts beyond this line.

3.2 Effect Of Inlet Temperature Increase On Compressor Pressure Rise

The effect of an inlet temperature increase on *compressor* (not compression system) pressure rise is demonstrated conceptually by the compressor performance map in Figure 3.7. The compressor is initially operating at point (A) when a quasi-steady temperature increase is applied across the compressor inlet. As the inlet temperature increases, corrected rotor speed, corrected mass flow rate, and compressor pressure ratio all decrease as shown by the operating point movement from point (A) to points (B), (C), and finally to point (D) in Figure 3.7. It is observed that compressor pressure rise decreases as the inlet temperature increases. This is due to the fact that the density of the working fluid decreases as the inlet temperature increases. This is the expected response of a compression system subjected to a quasi-steady inlet temperature increase.

Figure 3.8 conceptually shows the time history of compressor pressure rise and inlet temperature during an inlet temperature transient. Figure 3.8 is representative of experimental measurements obtained from an actual compressor subjected to an inlet temperature transient. It is observed that as the inlet temperature increases, compressor

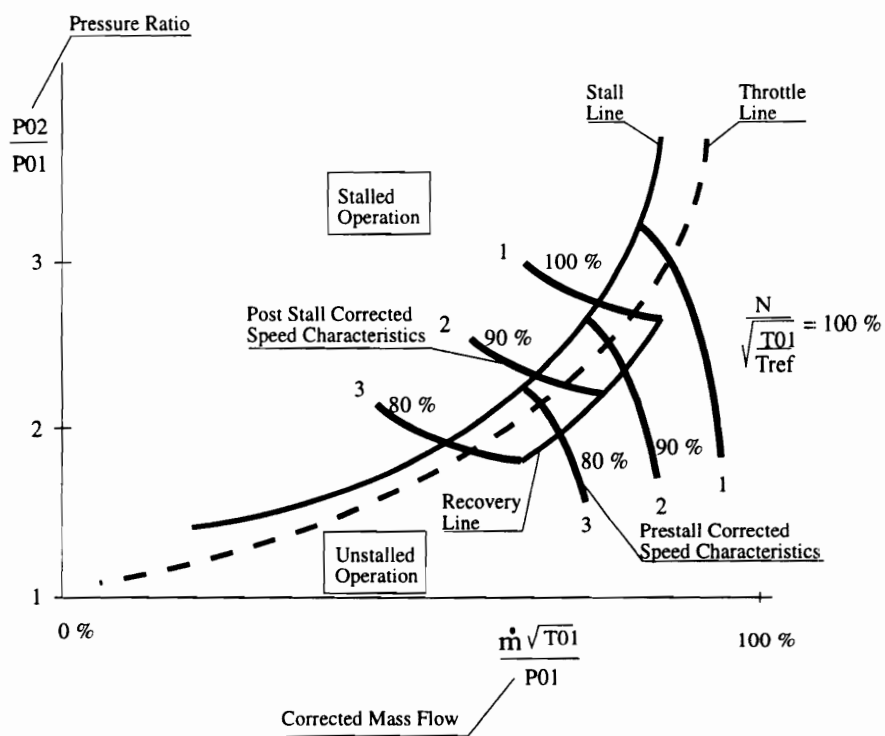


Figure 3.6 The Recovery Line

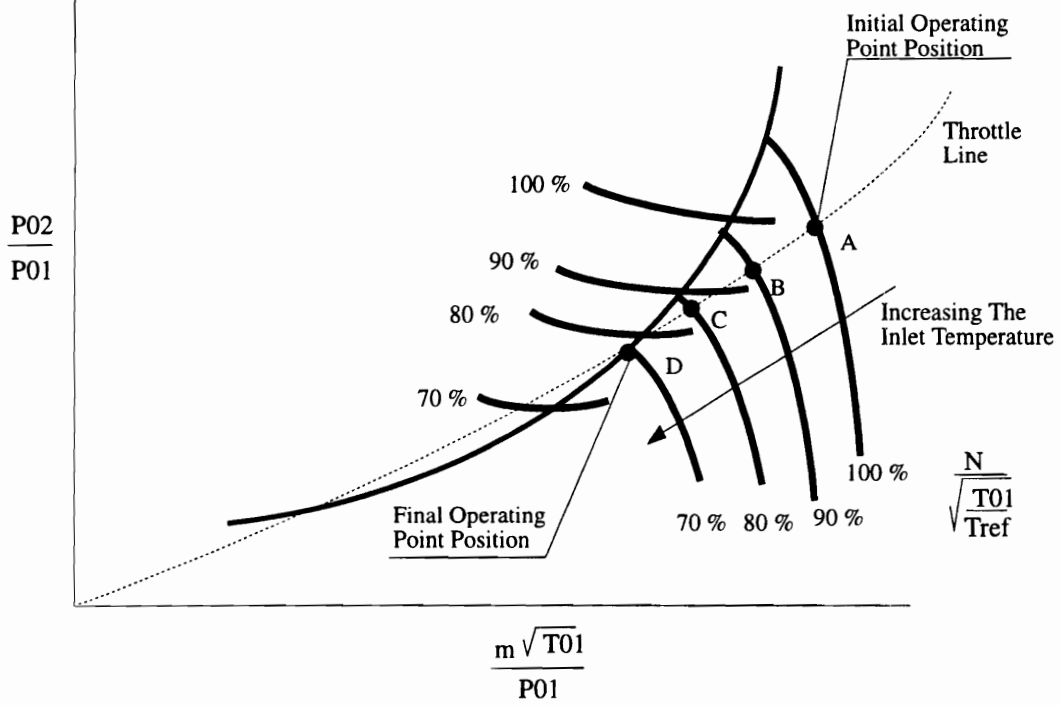


Figure 3.7 Compressor Response To Quasi-Steady Inlet Temperature Increase

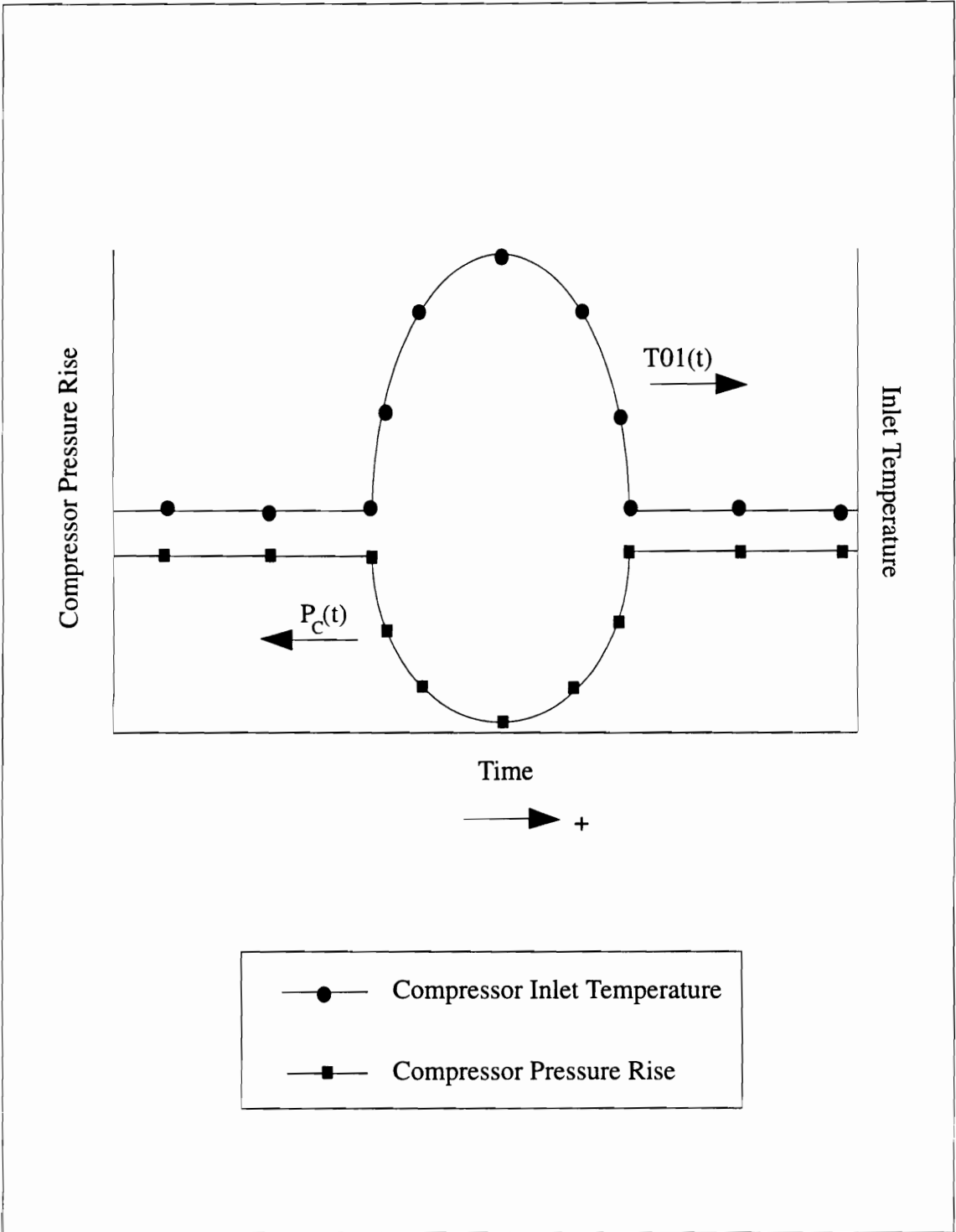


Figure 3.8 Time History of Compressor Pressure Rise and Inlet Total Temperature During An Inlet Temperature Transient

pressure rise decreases, indicating that compressor pressure rise is a function of inlet total temperature $P_C = P_C(T01)$. However, the numerical relationship of compressor pressure rise as a function of inlet total temperature $P_C = P_C(T01)$ is not easily determined.

It would be expected, and it has been observed experimentally, that compressor pressure rise is reduced as inlet temperature is increased. The shapes of the curves for inlet total temperature and compressor pressure rise in Figure 3.8 can be approximated as sinusoidal segments in time. These sinusoidal functions are reasonable approximations over the time interval when the temperature transient is applied across the compressor inlet and are based upon experimental observations. Inlet total temperature as a function of time can thus be approximated as

$$T01 = T01(t) = Ta + Tmax \text{ SIN}(\omega t + \phi) \quad (3.3)$$

where Ta is the ambient inlet temperature and $Tmax$ is the maximum absolute level of temperature obtained during the inlet temperature transient. Compressor pressure rise response as a function of time can be approximated as

$$P_C = P_C(t) = Pss - Pmin \text{ SIN}(\omega t + \phi) \quad (3.4)$$

where Pss is the steady state compressor pressure rise and $Pmin$ is the minimum absolute level of pressure rise that occurs during the inlet temperature transient. Since time is the independent variable in equations (3.3) and (3.4), it is clear that $P_C = P_C(T01)$.

3.3 Compression System Helmholtz Resonator Model

The dynamics of a *compression system* subjected to transient inlet temperature excursions may be ideally modeled as a classical Helmholtz resonator. A schematic of the compression system Helmholtz resonator model is shown in Figure 3.9. It consists of a plenum of volume (V_0), a circular compressor duct of constant area (A_c) and length (L). The compressor is represented by an actuator disk that accounts for the pressure rise across the compressor. The fluid in the compressor duct moves as a unit to provide a *mass* element. The acoustic pressure within the plenum provides a *stiffness* element and the opening radiates sound as a simple source does, thus providing a *resistance* element. The Helmholtz resonator and corresponding compression system can thus be analyzed by calculating the parameters of the analogous mechanical vibration system. The derivation of the differential equation of motion for the Helmholtz resonator is based upon the derivation in reference (11).

3.3.1 Differential Equation Of Motion

A control volume can be drawn around the fluid contained within the compressor duct as shown in Figure 3.10. While mass is allowed to flow steadily through this control volume and at any instant in time, the mass contained within the control volume is assumed to be, on the average, constant. A free body diagram of the mass of fluid

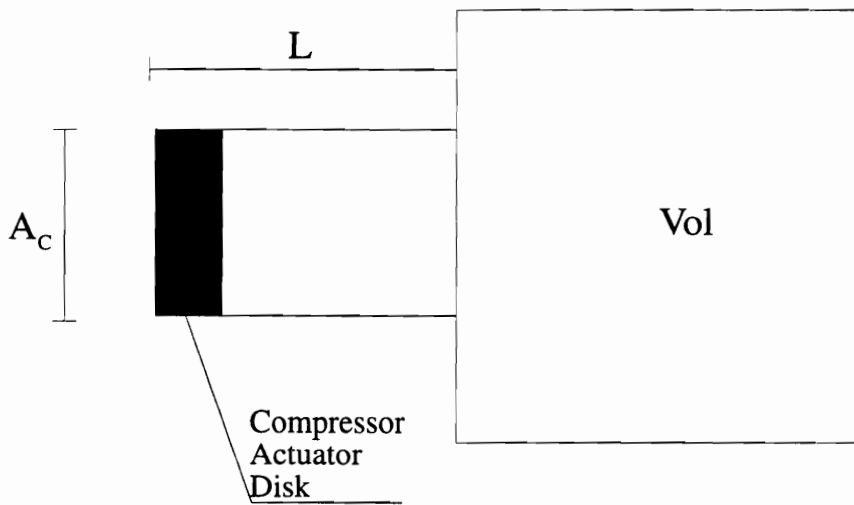
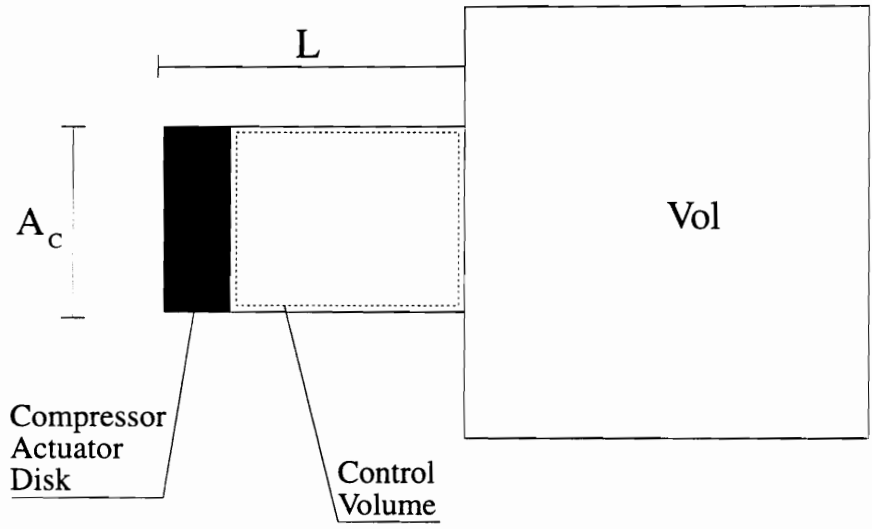


Figure 3.9 Compression System Helmholtz Resonator Model



Compressor Duct Fluid Control Volume

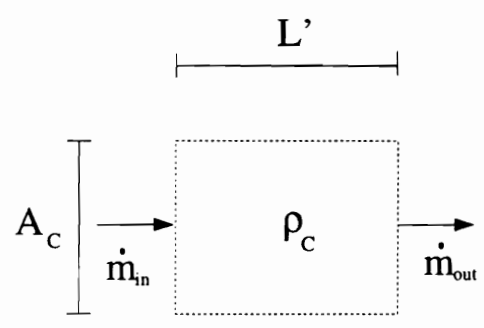


Figure 3.10 Compressor Duct Fluid Control Volume

contained within the compressor duct is shown in Figure 3.11. The resulting differential equation of motion for the inward displacement x of the fluid contained within the compressor duct is

$$m \frac{d^2 x}{dt^2} + \mathcal{R} \frac{dx}{dt} + cx = P_C A_C \sin(\omega t + \phi) \quad (3.5)$$

The fluid contained within the compressor duct has a total effective mass

$$m = \rho_C A_C L_{\text{eff}} \quad (3.6)$$

where L_{eff} , the effective length of the compressor duct, is longer than the physical length because of its radiation-mass loading as described in reference (11). The effective length of the compressor duct is calculated as

$$L_{\text{eff}} = L + 1.5r \quad (3.7)$$

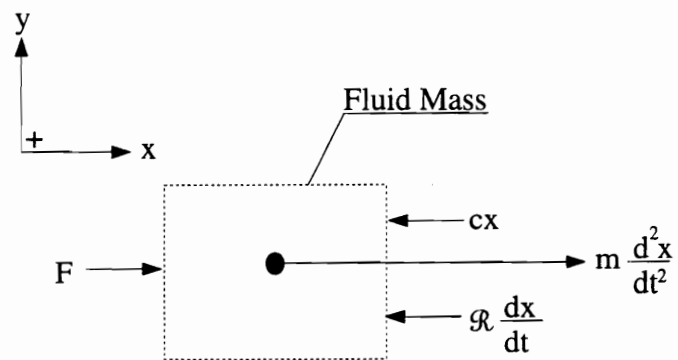
where r is the compressor duct radius and L is the physical compressor duct length.

To determine the stiffness of the system, consider the compressor duct to be fitted with an air-tight piston as shown in Figure 3.12. When this piston moves a distance x towards the plenum chamber, the volume in the plenum is changed by $\Delta V_{\text{ol}} = -A_C x$. The change in plenum volume $\Delta V_{\text{ol}} = -A_C x$, results in a condensation which by definition is

$$\frac{\Delta \rho}{\rho_C} = \frac{\rho - \rho_C}{\rho_C} \quad (3.8)$$

where ρ is the instantaneous density of the fluid within the compressor duct and ρ_C is the constant equilibrium density of fluid contained within the compressor duct. The

Free Body Diagram



$$\Sigma F = m \frac{d^2x}{dt^2}$$

Figure 3.11 Fluid Mass Free Body Diagram

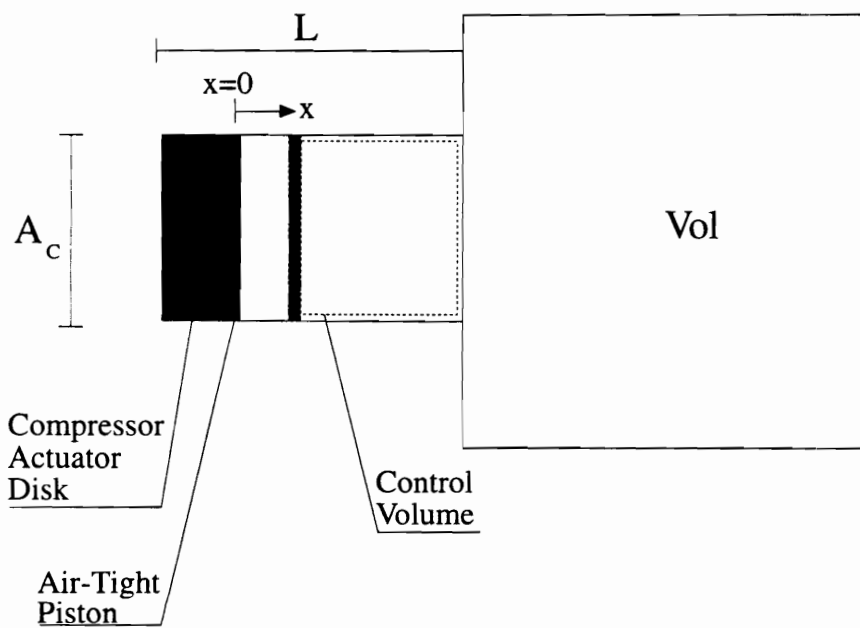


Figure 3.12 Air-Tight Piston

condensation can be expressed in terms of the change in volume as $\frac{\Delta\rho}{\rho} = \frac{-\Delta\text{Vol}}{\text{Vol}}$ by the

ideal gas equation of state. By substitution,

$$\frac{\Delta\rho}{\rho} = \frac{-\Delta\text{Vol}}{\text{Vol}} = \frac{A_c x}{\text{Vol}} \quad (3.9)$$

The acoustic pressure is defined as

$$p = \rho_c \left[\frac{\partial P}{\partial \rho} \right]_s \left[\frac{\rho - \rho_c}{\rho_c} \right] \quad (3.10)$$

where the term $\left[\frac{\partial P}{\partial \rho} \right]_s$ is the square of the definition of the isentropic speed of sound for

a gas

$$a = \sqrt{\left[\frac{\partial P}{\partial \rho} \right]_s} \quad (3.11)$$

Equation (3.10) can be rewritten using equations (3.8) and (3.9) as

$$p = \rho_c a^2 \left[\frac{\Delta\rho}{\rho_c} \right] \quad (3.12)$$

The pressure increase in the plenum chamber P_p , resulting from the displacement of the air-tight piston towards the plenum chamber, is equal to the acoustic pressure p and is expressed as

$$P_P = \rho = \rho_C a^2 \left[\frac{\Delta \rho}{\rho_C} \right] \quad (3.13)$$

Combining equation (3.13) with equation (3.9), the pressure increase in the plenum chamber as a result of the displacement of the air-tight piston towards the plenum chamber in terms of the volume change is

$$P_P = \rho_C a^2 \frac{A_C x}{Vol} \quad (3.14)$$

The force $F = P_P A_C$ required to maintain the displacement is $\rho_C a^2 \frac{A_C^2 x}{Vol}$. Therefore, the effective stiffness c is

$$c = \rho_C a^2 \frac{A_C^2}{Vol} \quad (3.15)$$

where $c = \frac{F}{x}$.

It is assumed that the moving fluid contained within the compressor duct radiates sound into the surrounding medium in the same manner as an open-ended pipe. Therefore, the radiation resistance is

$$R = \rho a \frac{k^2 A_C^2}{4\pi} \quad (3.16)$$

where $k = \omega / a$. The instantaneous driving force produced by a sound wave of amplitude P_C impinging on the resonator opening is

$$F = P_C A_C \sin(\omega t + \phi) \quad (3.17)$$

where ω is the driving frequency and ϕ is the phase angle.

It is recalled that the *compressor pressure rise* P_c was shown to be a function of the inlet temperature T_{01} . This is the link between an inlet temperature transient and the excitation of a dynamic response from a compression system, which shows that a dynamic compression system response may be induced by an inlet temperature transient. This link is accomplished through equation (3.5).

3.3.2 Solution To The Differential Equation Of Motion

Equation (3.5) is a second order, nonhomogeneous, constant coefficient ordinary differential equation for the Helmholtz resonator model, and is analogous to the mechanical vibration differential equation of motion of a driven oscillator. Therefore, the solution to equation (3.5) is the forced response of the Helmholtz resonator driven by the forcing function. The solution to equation (3.5) can also represent the dynamic response of a corresponding *compression system* driven by an inlet temperature transient. This is accomplished by replacing the forcing function in equation (3.5) with a function that represents the *compressor pressure rise* as a function of time during an inlet temperature transient. This function that represents *compressor pressure rise* as a function of time during an inlet temperature transient is the developed sinusoidal approximation of compressor pressure rise as a function of time during an inlet temperature transient, as previously discussed.

The decrease in compressor pressure rise during the inlet temperature transient will be the driving force for the Helmholtz resonator model, and the corresponding compression system dynamic response. By using developed forcing functions that represent compressor pressure rise as functions of time during high and low magnitude inlet temperature transients, the forced response of the Helmholtz resonator and the corresponding compression system, subjected to high and low magnitude inlet temperature transients, can be observed.

Figure 3.13 is the solution to equation (3.5) for two different continuous compressor pressure rise sinusoidal forcing functions developed for representing two different inlet temperature transients. One forcing function represents the compressor pressure rise during a low magnitude inlet temperature transient, and the other forcing function represents the compressor pressure rise during a high magnitude inlet temperature transient. The fact to be observed in Figure 3.13 is that the higher the magnitude of the inlet temperature transient, the larger the dynamic response from the Helmholtz resonator model and corresponding compression system. Figure 3.13 represents the dynamic response of the Helmholtz resonator model and corresponding compression system as if they were being continually driven by periodic inlet temperature transients.

Figure 3.14 represents the dynamic response of the Helmholtz resonator model and corresponding compression system after the inlet temperature transients are removed from the compressor inlet. Removal of the inlet temperature transient from the

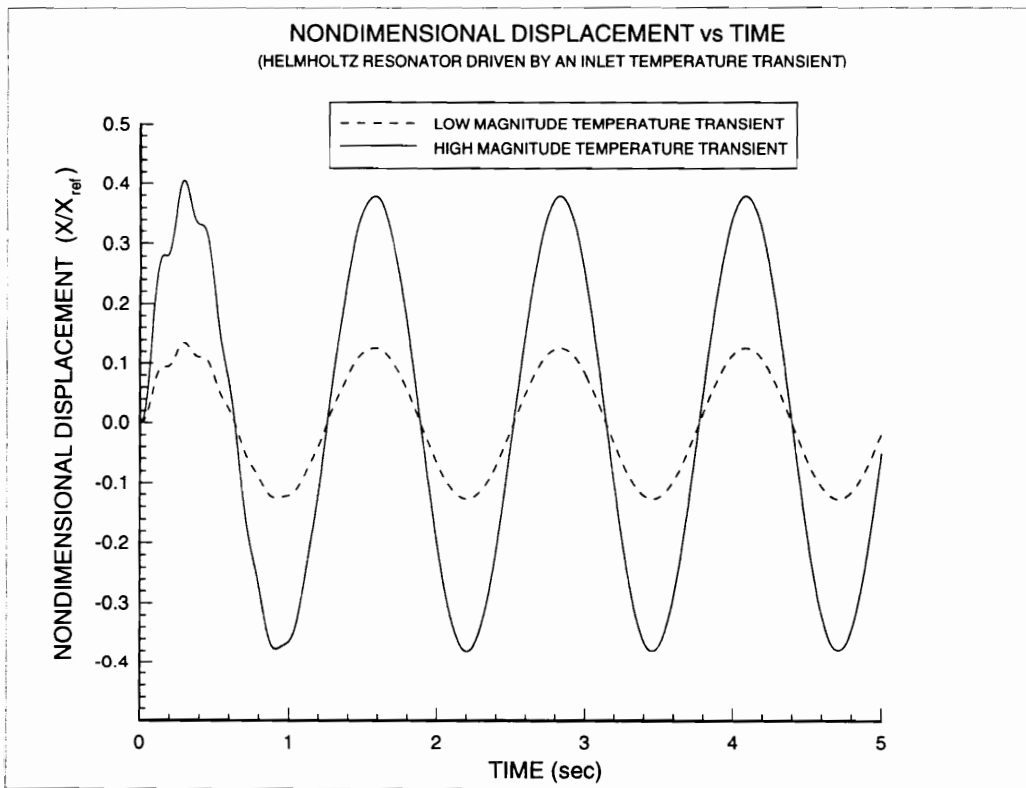


Figure 3.13 Helmholtz Resonator Driven By An inlet Temperature Transient

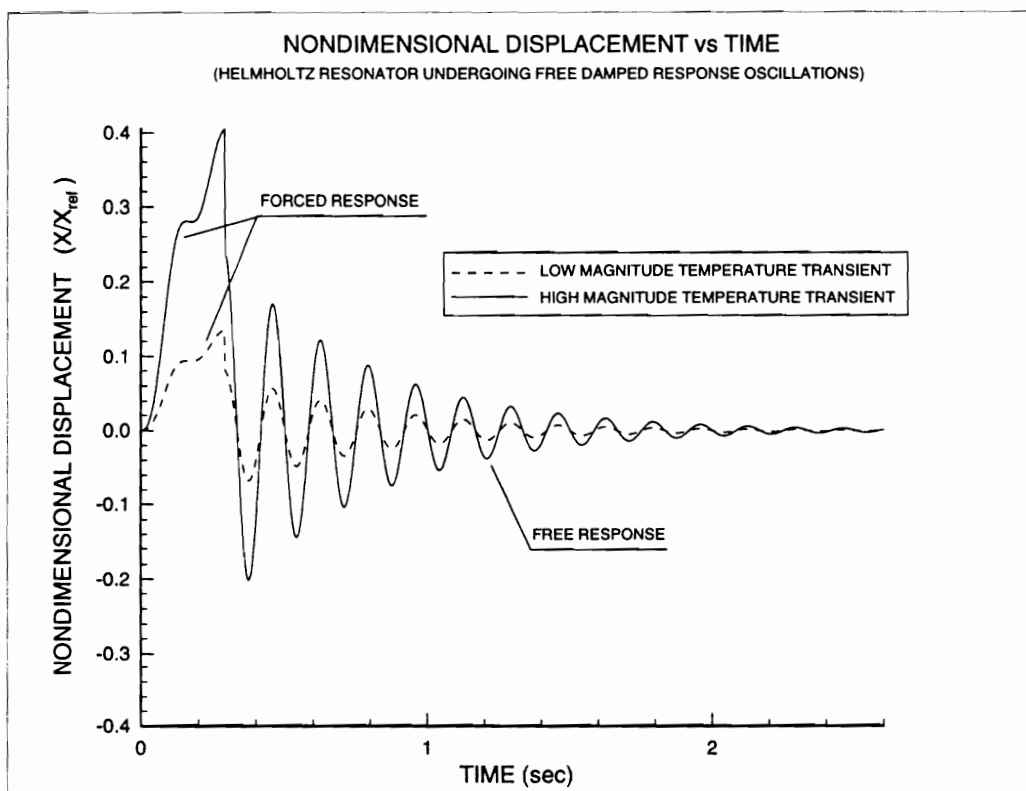


Figure 3.14 Helmholtz Resonator Undergoing Free Damped Response Oscillations

compressor inlet implies removal of the compressor pressure rise forcing function from equation (3.5) in this case, the end of a temperature transient. This allows the right hand side of equation (3.5) to be set equal to zero, causing the dynamic response of the Helmholtz resonator model and corresponding compression system to undergo free damped vibrational motion as shown in Figure 3.14. It is observed from Figure 3.14 that as the dynamic response of the Helmholtz resonator model undergoes free damped vibrational motion, the amplitude of the damped oscillations associated with the high magnitude inlet temperature transient are greater than the amplitude of the damped oscillations associated with the low magnitude inlet temperature transient.

3.4 Compression System Dynamic Response On Compressor Performance Map

According to the predictions of the previously presented model, a large dynamic increase in compressor inlet temperature, which is associated with a high magnitude inlet temperature transient, corresponds to a large dynamic decrease in compressor pressure rise and induces a large compression system dynamic response. Similarly, a small dynamic increase in compressor inlet temperature, which is associated with a low magnitude inlet temperature transient, corresponds to a small dynamic decrease in compressor pressure rise and induces a small compression system dynamic response.

Compression system dynamic response is a change in both the compressor pressure ratio and corrected mass flow of the compression system. A large compression

system dynamic response produces large changes in compressor pressure ratio and corrected mass flow while a small compression system dynamic response produces small changes in compressor pressure ratio and corrected mass flow. During a compression system dynamic response, the changes in compressor pressure ratio and corrected mass flow produce a “loop” on a compressor performance map as illustrated in Figure 3.15. The “loop” represents the path taken by the compression system operating point while in dynamic transit to a new operating condition.

That a “loop” trace on the compressor performance map would be formed follows from consideration of the response characteristics of a second-order mechanical system. The response (x / x_{ref}) of such a system is always at a phase angle ϕ with respect to the forcing function. The corrected mass flow will respond to the sinusoidal temperature forcing function with another phase angle, (near zero degrees), since

$$\dot{m}_C = \frac{\dot{m}\sqrt{T01}}{P01} \quad (3.18)$$

and

$$T01 = Ta + Tmax \text{ SIN}(\omega t) \quad (3.19)$$

while P01 is constant, and \dot{m} is, on the average, assumed constant. Thus, with (P02/P01)

at phase angle ϕ , and $\frac{\dot{m}\sqrt{T01}}{P01}$ at phase angle zero, an ellipse or circle will be generated

on the compressor performance map plot as T01 varies sinusoidally.

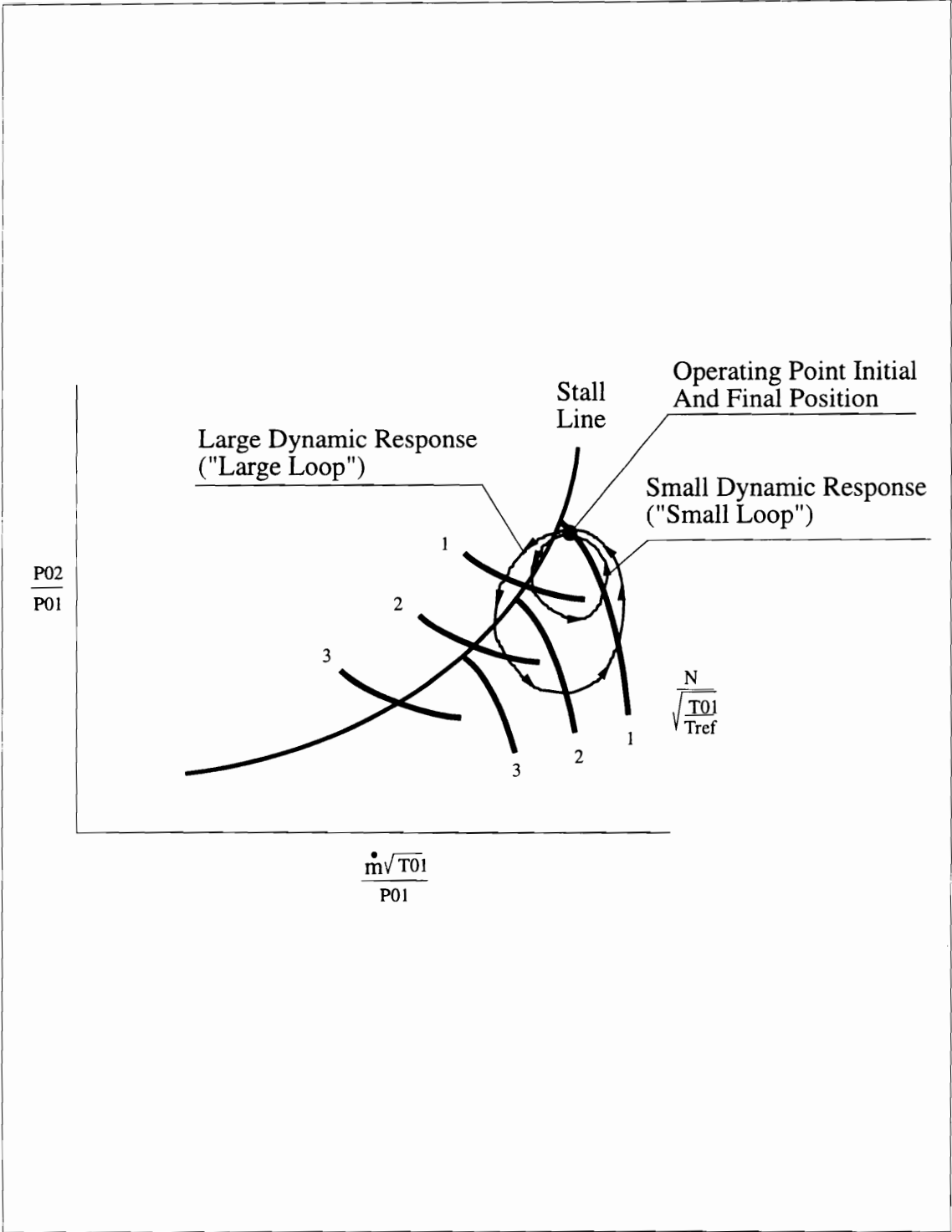


Figure 3.15 Conceptual Compression System Dynamic Response Paths

Figure 3.15 is a compressor performance map with conceptual compression system dynamic response paths indicated. A high magnitude inlet temperature transient causes a large compression system dynamic response, with large changes in compressor pressure ratio and corrected mass flow, producing a “large loop” on the compressor performance map as indicated in Figure 3.15. Similarly, a low magnitude inlet temperature transient causes a small compression system dynamic response, with small changes in compressor pressure ratio and corrected mass flow, producing a “small loop” on the compressor performance map as indicated in Figure 3.15.

3.5 Energized Compression System Rotating Stall And Recovery Hypotheses

The significance of the stall and recovery lines, and what they imply with respect to the flow passing over the actual blades on the compressor rotor, becomes evident when demonstrating how a compressor dynamically stalls or recovers from rotating stall operation during an inlet temperature transient. The addition of energy to a compression system in the form of a transient inlet temperature excursion energizes a dynamic response from the compression system. As previously discussed, the compression system dynamic response is a change in both the compressor pressure ratio and corrected mass flow of the compression system, producing a “loop” on the compressor performance map. This “loop” represents the path taken by the compression system operating point while in dynamic transit to a new operating condition.

The compression system dynamic response produces dissimilar blade Mach number triangles during the compression system dynamic transit, that deviate from the similar blade Mach number triangles associated with a quasi-steady inlet temperature increase. This results in variations in rotor blade incidence and flow angle of attack according to equation (3.2). Therefore, in response to a temperature transient applied across the compressor inlet, the compression system may traverse stalled and unstalled states on the quasi-steady performance map while in dynamic transit to a new operating condition, providing the potential for rotating stall and rotating stall recovery processes which would not be possible with quasi-steady system response.

3.5.1 Compression System Rotating Stall Hypothesis

If the dynamic response of the energized compression system drives the operating point across the stall line, the compressor rotor blades will experience a transient increase in blade incidence and flow angle of attack sufficient to induce rotating stall. Figure 3.16 conceptually shows the rotating stall hypothesis. The compressor is initially operating unstalled at point (A) on the 90 % prestall corrected speed characteristic in Figure 3.16 when an inlet temperature transient is applied across the compressor inlet. The dynamic response of the compression system drives the operating point across the stall line. This is demonstrated by the path taken by the operating point during the inlet temperature transient in Figure 3.16. As the operating

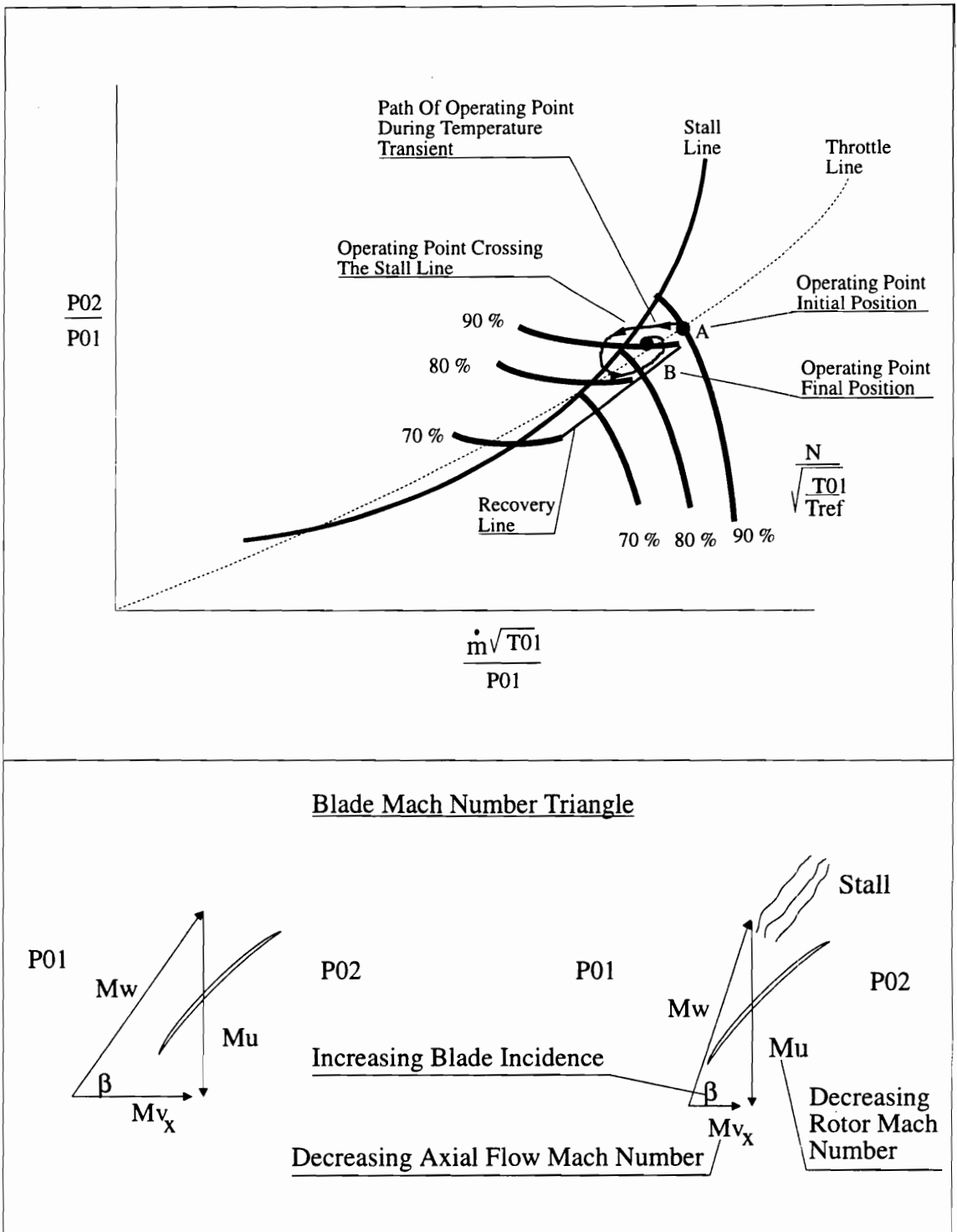
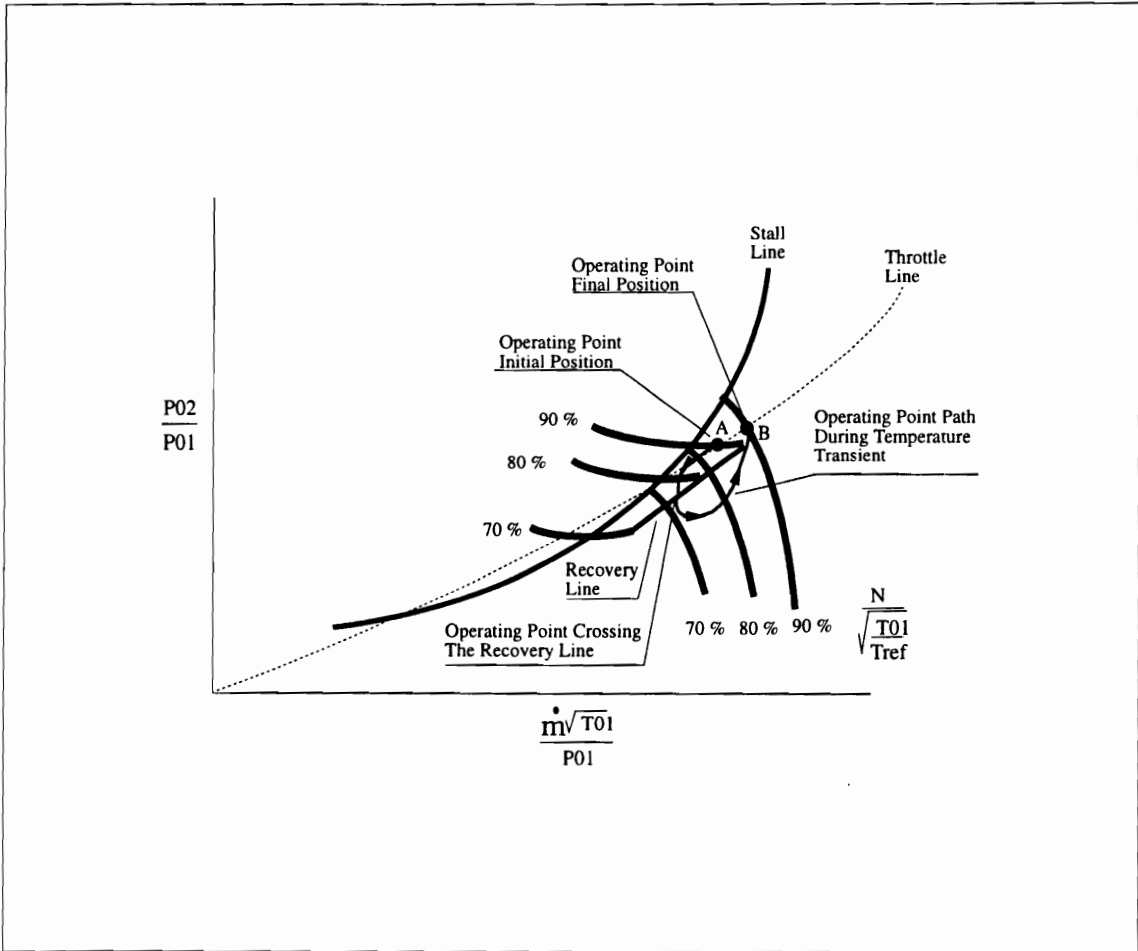


Figure 3.16 Compressor Dynamic Stall By Inlet Temperature Transient

point crosses the stall line, the compressor rotor blades experience a transient increase in blade incidence and flow angle of attack sufficient for inducing rotating stall. The operating point then settles on the corresponding 90 % post-stall corrected speed characteristic at point (B) as the inlet temperature decays back to the ambient inlet temperature, indicating that the compressor is now operating in fully developed rotating stall.

3.5.2 Compression System Rotating Stall Recovery Hypothesis

If the transient response of the energized compression system drives the operating point across the recovery line, the compressor rotor blades will experience a transient decrease in blade incidence and flow angle of attack sufficient for inducing rotating stall recovery. Figure 3.17 conceptually shows the rotating stall recovery hypothesis. The compressor is initially operating in fully developed rotating stall at point (A) on the 90 % post-stall corrected speed characteristic in Figure 3.17 when an inlet temperature transient is applied across the compressor inlet. The dynamic response of the compression system drives the operating point across the recovery line inducing rotating stall recovery. This is demonstrated by the path taken by the operating point during the inlet temperature transient in Figure 3.17. As the operating point crosses the recovery line, the compressor rotor blades experience a transient decrease in blade incidence and flow angle of attack sufficient for inducing rotating stall recovery. The



Blade Mach Number Triangle

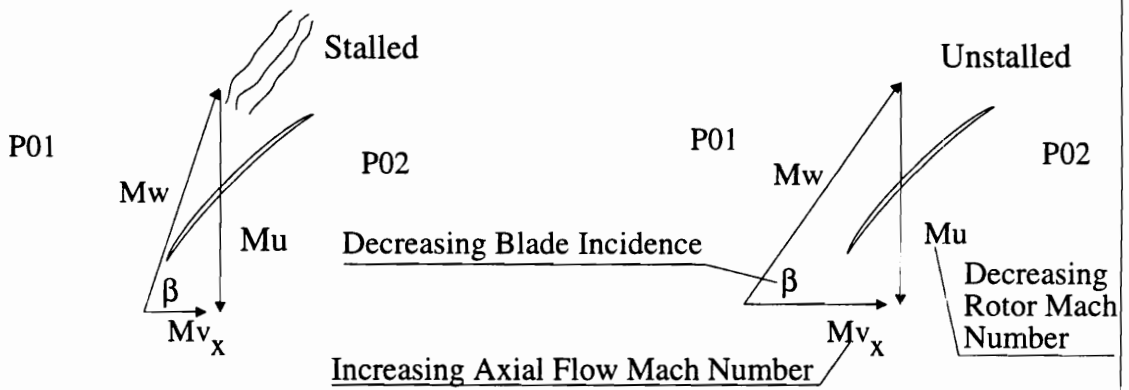


Figure 3.17 Compressor Dynamic Recovery From Rotating Stall By Inlet Temperature Transient

operating point then settles on the corresponding 90 % prestall corrected speed characteristic at point (B) as the inlet temperature decays back to the ambient inlet temperature, indicating that the compressor recovered from the rotating stall operating condition.

3.6 Summary Of The Theory

The addition of energy to a compression system in the form of transient inlet temperature excursions energizes a dynamic response from the compression system. The compression system dynamic response is a change in both the compressor pressure ratio and corrected mass flow of the compression system, producing a “loop” on the compressor performance map. This “loop” represents the path taken by the compression system operating point while in dynamic transit to a new operating condition.

A high magnitude inlet temperature transient causes a large compression system dynamic response, with large changes in compressor pressure ratio and corrected mass flow, producing a “large loop” on the compressor performance map. A low magnitude inlet temperature transient causes a small compression system dynamic response, with small changes in compressor pressure ratio and corrected mass flow, producing a “small loop” on the compressor performance map. The compression system dynamic response produces dissimilar compressor blade Mach number triangles during the compression system dynamic transit, resulting in variations in rotor blade incidence and flow angle of

attack relative to the compressor blades. Therefore, the compression system may traverse stalled and unstalled states on the quasi-steady performance map while in dynamic transit to a new operating condition, providing the potential for rotating stall and rotating stall recovery processes which would not be possible with quasi-steady system response. An experiment to be described will demonstrate these concepts.

4. DESCRIPTION OF EXPERIMENT

A special test facility was developed for an experimental demonstration of the theory. It is located at the Virginia Polytechnic Institute and State University Airport, and shown in Figure 4.1.

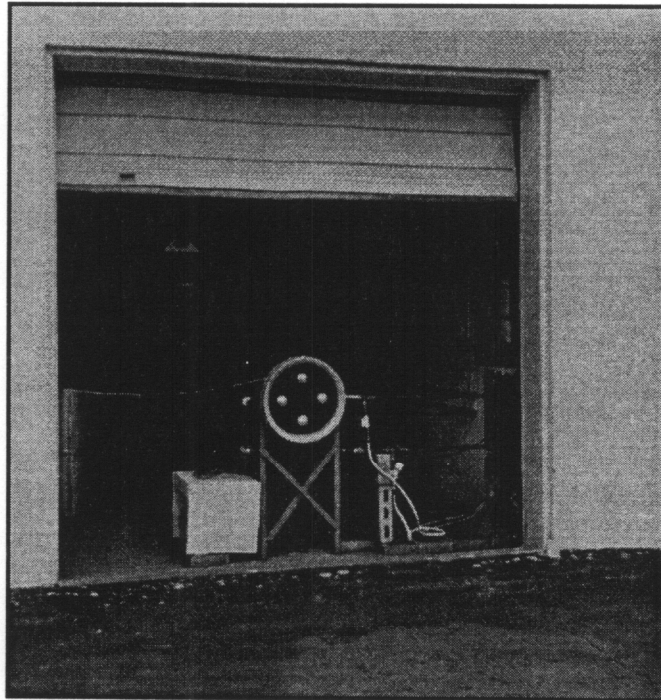


Figure 4.1 Test Facility

It is now part of the Mechanical Engineering Department's Turbomachinery and Propulsion Research Laboratory. This special combustion test cell was designed and developed to operate a temperature transient generator in the inlet of a low speed two stage axial flow compressor.

4.1 Test Cell

The basic layout of the test cell is shown in Figure 4.2. The test cell is rectangular in shape, having a length of 25 ft (7.6 m), a width of 12.5 ft (3.8 m), and a height of 15 ft (4.6 m). Two rectangular windows, made of lexane glass, are installed in the wall to allow sight into the test cell from the adjacent control room. The windows are 3 ft (0.91 m) long, 1.5 ft (0.46 m) wide, and 0.25 inches (0.006m) thick. One window is installed in the front of the cell and the other window is installed in the rear. The two windows are positioned with their center 4 ft (1.2 m) off of the test cell floor. The rear window is positioned 7 ft (2.1 m) from the cell back wall. The lexane glass is shatter proof and provides protection against shrapnel and debris in the event of an explosion or a compressor rotor disk rupture.

4.2 Compressor

The test article used in this experiment is a General Electric, two stage, subsonic, axial flow compressor as shown in Figure 4.3. This compressor has a diameter of 19 inches (0.48 m) and is driven by a 5 HP General Electric electrical motor. Each rotor has 24 blades that are RAF-6 airfoil sections as shown in Figure 4.4. The blades have a span of 2.75 inches (0.07 m) and a tip to hub ratio of 1.4074 producing a compressor flow area of 0.975 ft² (0.09 m²). An aluminum circular centerbody cone is positioned at the compressor inlet to contract the flow area at the entrance to the first rotor. This cone has a base diameter of 13.5 inches (0.34 m), an altitude of 18 inches (0.46 m), and a tip radius of 1.5 inches (0.038 m). The compressor is anchored to the floor in the rear of the test cell

Experimental Test Facility

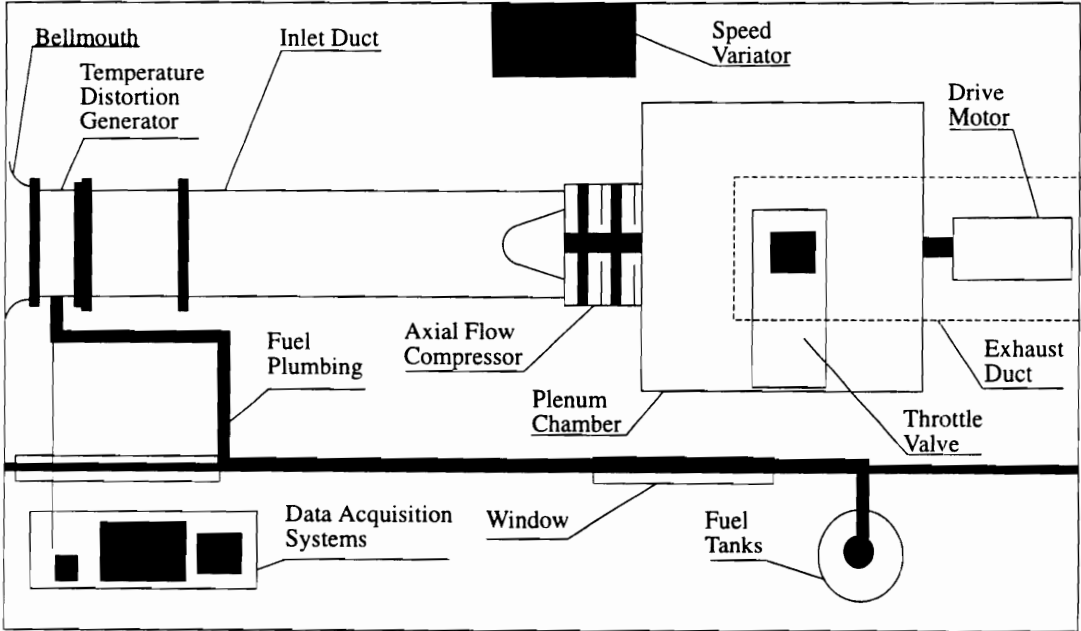


Figure 4.2 Test Cell

and stands with its center 3 ft (0.91 m) above the test cell floor. The top speed of this compressor is 2500 RPM.

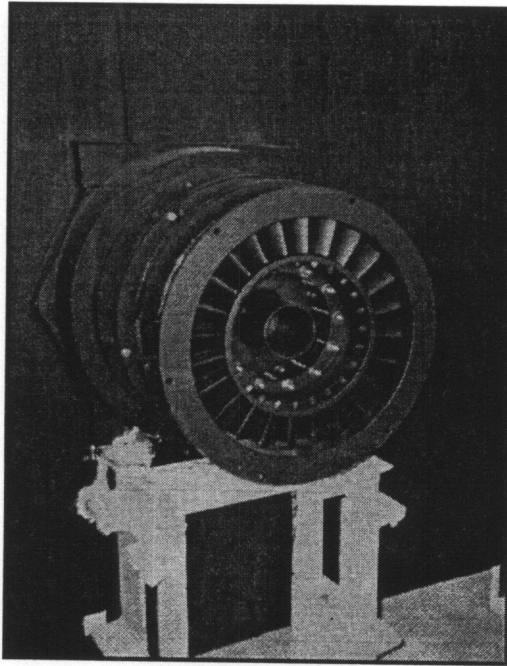


Figure 4.3 Two Stage Low Speed Compressor

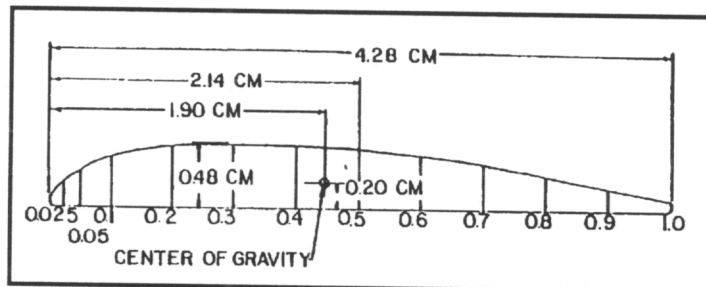


Figure 4.4 RAF- Airfoil Section

4.3 Plenum Chamber

The compressor discharges into a rectangular wooden plenum chamber 6 ft x 6 ft x 4 ft (1.8 m x 1.8 m x 1.2 m). This produces a volume of 144 ft³ (4 m³), which is sufficient to allow the compressor to operate in rotating stall. The rotor mechanical speed and pressure ratio are too low to allow a surge to occur. The inner walls of the plenum are treated with a fire retardant to protect the wood against fire and heat associated with combustion from the temperature transient generator. A photograph of the plenum chamber is shown in Figure 4.5.

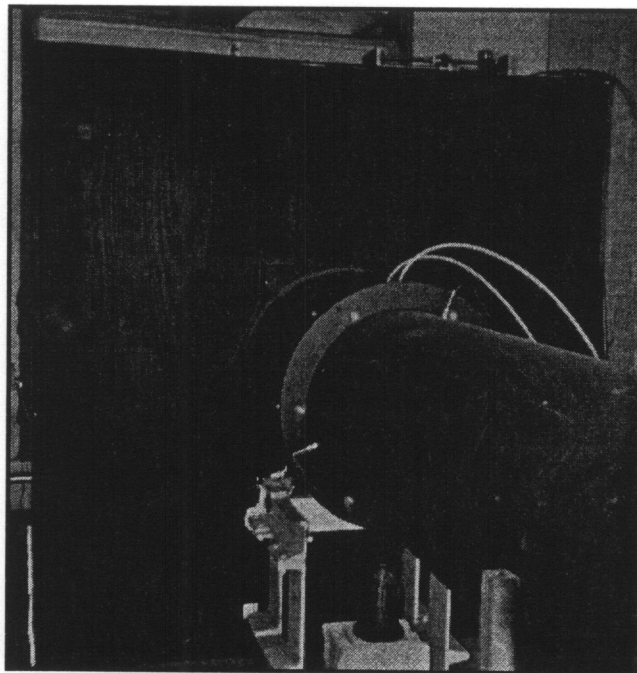


Figure 4.5 Plenum Chamber

4.4 Throttle Valve

A mechanical throttle valve is positioned in the center of the top of the plenum chamber a shown in Figure 4.6.

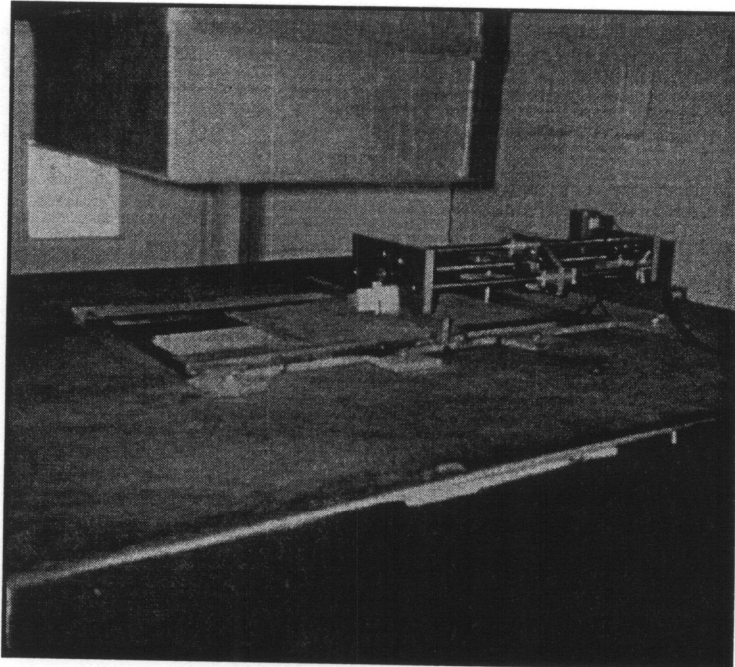


Figure 4.6 Throttle Valve

This throttle valve is fabricated from aluminum and is driven by an electric traverse mechanism. The traverse consists of an electric stepper motor, worm gear, mechanical worm, and a potentiometer. The traverse mechanism moves a flat aluminum plate in linear translation motion between two tracks. The plenum flow discharge area is located under these tracks and decreases as the plate slides between the tracks. Therefore, throttling the compressor is accomplished by sliding the flat plate between the tracks.

4.5 Inlet Duct System

A 12 ft (3.7 m) circular inlet duct is positioned in front of the compressor inlet. This inlet duct is steel and 19 inches (0.48 m) in diameter. A short radius aluminum bellmouth is positioned at the inlet of the temperature transient generator. A photograph of the inlet duct is shown in Figure 4.7.

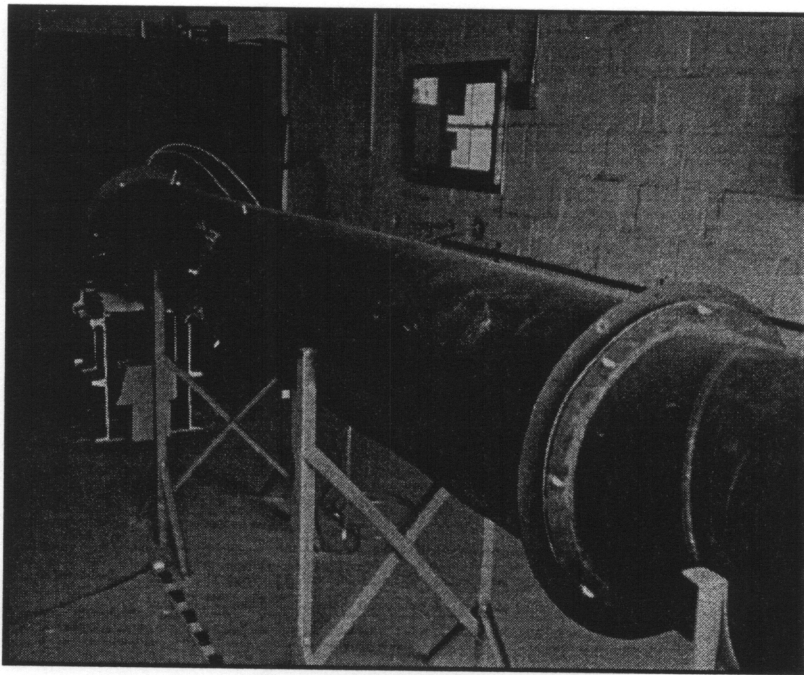


Figure 4.7 Inlet Duct

4.6 Temperature Transient Generator

Figure 4.8 shows the experimental inlet temperature transient generator. Four cylindrical propane burners are mounted in the four quadrants of the burner. Steel support struts hold the burners in position. A set of three holes are drilled in the outer casing for each of the

four cylindrical burners. The first hole accommodates an air hose that attaches to each cylindrical burner in each of the quadrants. This hose delivers the oxidizer to the burner for the combustion reaction which was compressed air for this experiment. The second hole allows for a fuel pipe to attach to each cylindrical burner in each of the quadrants. The fuel burned in this experiment was liquid propane. The third hole allows an ignition wire to be attached to each ignition plug on each of the cylindrical burners. The ignition system is electrical and utilizes capacitive discharge ignition. Specifications associated with ignition system hardware are contained in Appendix E. Details regarding the uniformity of the temperature distortions produced can be found in reference (13).

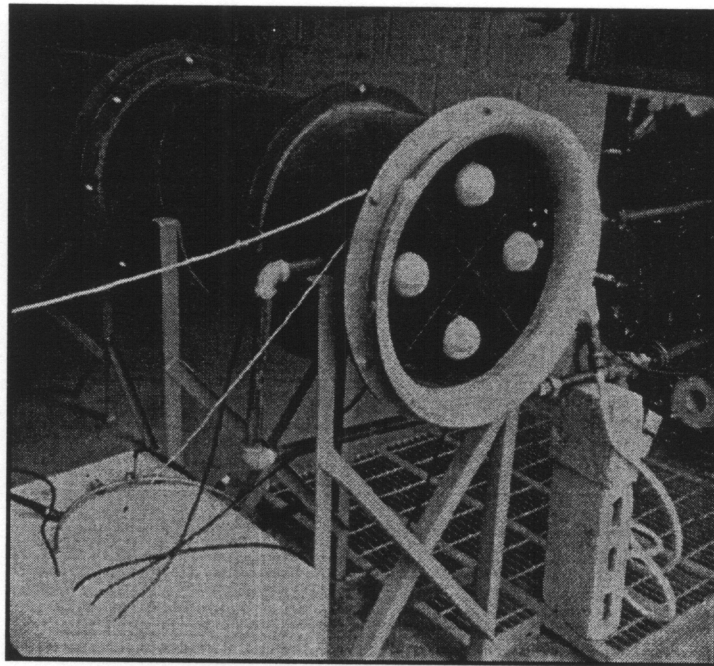


Figure 4.8 Temperature Transient Generator

4.7 Fuel Delivery and Control

The propane fuel is stored in two 100 lbf (0.45 kN) cylinders and delivered from the tanks to the burners by high pressure rubber hoses as shown in Figure 4.9. Each tank provides fuel

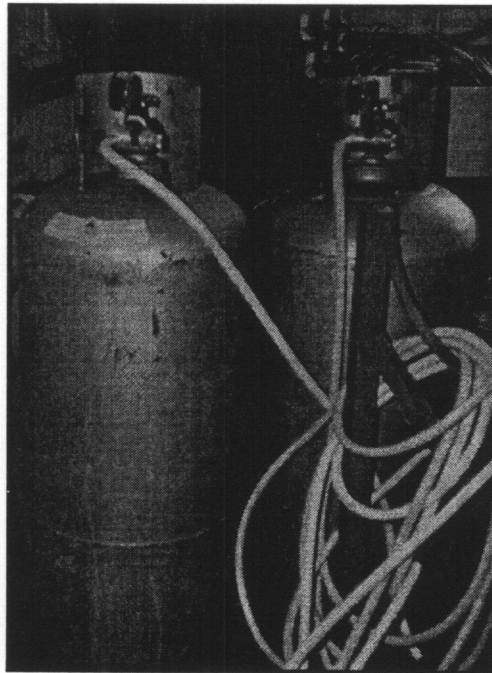


Figure 4.9 Propane Tanks

for two quadrants in the temperature transient generator. Thus, four fuel lines are connected to the temperature transient generator, one fuel line per quadrant. Each fuel line terminates with a 0.75 inch (0.019 m) electronic solenoid valve just before its attachment to the temperature transient generator. This electronic solenoid valve opens when it is energized by an electric current. The specifications on the solenoid valves are contained in Appendix E. Attached directly to each solenoid valve exit is a 0.75 inch

(0.019 m) regulator gate valve. The exit of each gate valve connects directly to a cylindrical burner in each quadrant of the temperature transient generator with 0.75 inch (0.019 m) black iron pipe. The function of the two storage tanks is to supply the fuel at a high pressure and flow rate. The high pressure hoses deliver the fuel to the respective quadrants. The function of the solenoid valves are to open and close to control the fuel discharge to their respective burners. The function of the gate valve is to regulate the amount of fuel delivered to the burner. This allows the fuel-to-air ratio to be varied and also allows control of the combustion temperature. The gate regulator valves are manually controlled by the operator.

4.8 Instrumentation

High response instrumentation was used to gather the data for the experiment. Instrumentation was positioned throughout the inlet duct system, compressor, and plenum chamber. The instrumentation used in obtaining data consists of three Edison 286 computers, 14 type K chromel alumel thermocouples, and five pressure transducers. All instrumentation was calibrated in the Mechanical Engineering Department Instrument Shop before it was installed.

4.8.1 Computer

Three Edison 286 computers were used to operate, control, and gather data for the experiment. Each computer contained a DT2805 Data Translation board, which is a high response data acquisition board. The specifications of this data acquisition board are contained in the Appendix E. Connected to each data acquisition board was a DT707-T

external screw terminal panel. This particular screw terminal panel provides a thermocouple reference cold junction compensation circuit by which the user can determine the temperature of the screw terminal panel. A user-written program compensates for the cold junction thermocouple formed at the DT707-T. When the cold-junction compensation circuit is calibrated, the sensor output is $0.4\text{mV}/(\text{C})$. The specifications on the DT707-T screw terminal panel are contained in Appendix E. Each card could read up to seven channels for data.

Two computers were designated to read thermocouple measurements only while the third computer read pressure data. The computers were synchronized such that when a trigger signal was sent to the data acquisition card, all computers would begin sampling at the same rate. The trigger signal was produced by a square wave generator. The computer sample rate was 30 samples per second or 0.033 sec/sample . The raw data was measured in voltages and stored in an array. After the data run was terminated, the computer automatically converted the voltages to temperatures and pressures. The temperatures and pressures were stored in individual arrays according to channel from which they were measured. Post processing allowed these arrays to be analyzed and plotted with TECPLOT. The sample rate allowed 24 seconds of data sampling per data run. For the experimental operational speed of 2000 RPM, preliminary tests revealed that sampling data at 30 samples per second was sufficient for capturing the phenomena of interest associated with the inlet temperature transient. These tests revealed a clear distinction between unstalled and stalled operation of the compressor.

4.8.2 Thermocouples

Fourteen OMEGA type K chromel alumel thermocouples were used to obtain the experimental thermal data. Each thermocouple was a bare wire exposed junction type K thermocouple. The thermocouples were fabricated from 0.005 inch (0.00013 m) diameter wire with a response time of 0.08 seconds. The response time or “time constant” is defined as the time required to reach 63.2% of an instantaneous temperature change. This time constant was used in a first order time lag equation to adjust the thermal data to account for the response time of the thermocouple wire being used. Each thermocouple was installed in a 0.125 inch (0.003 m) diameter stainless steel sheath for mounting to the inlet duct system and compressor. The thermocouple sheath was sealed with high temperature resistant silicon with the exposed wire junction extending out one end of the sheath.

The thermocouples were mounted around the circumference of the compressor in 60 degree circumferential increments. Six were mounted in front of the rotor of stage one and six were mounted in front of the rotor of stage two as shown in Figure 4.10. The thermocouples were positioned approximately 0.25 inches (0.006 m) away from the rotors and extended into the casing such that the temperature measurements were made at the mean radius of the compressor.

A thermocouple was positioned at the throttle exit and another was positioned in the center of the plenum chamber as shown in Figure 4.11. The wire ends of the thermocouples were attached to the DT707-T external screw terminal panels of the computers. The measurement error associated with these thermocouples is found in Appendix E.

Thermocouple Position (Compressor)

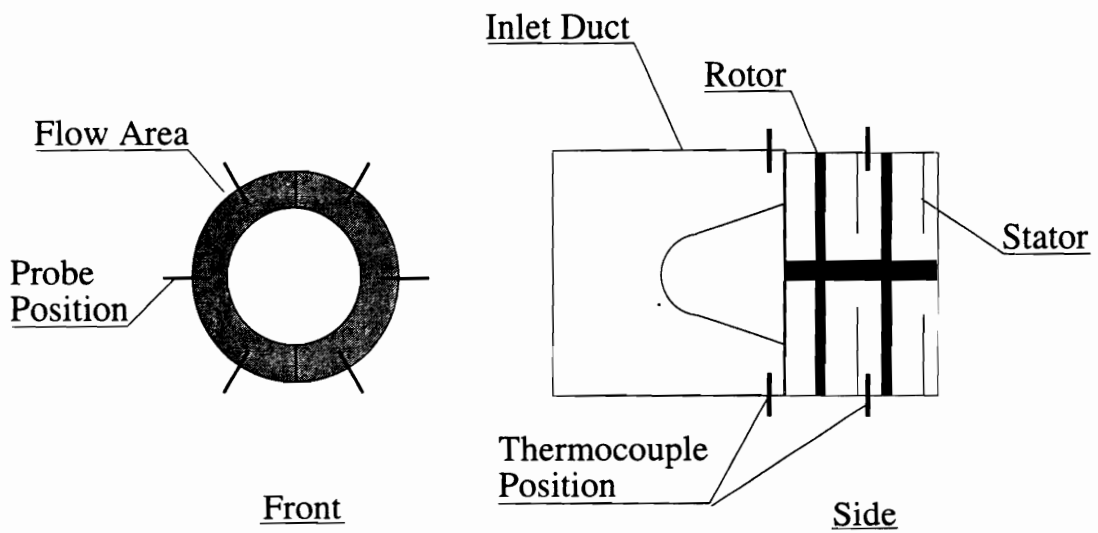


Figure 4.10 Thermocouple Position (Compressor)

Thermocouple Position (Plenum Chamber)

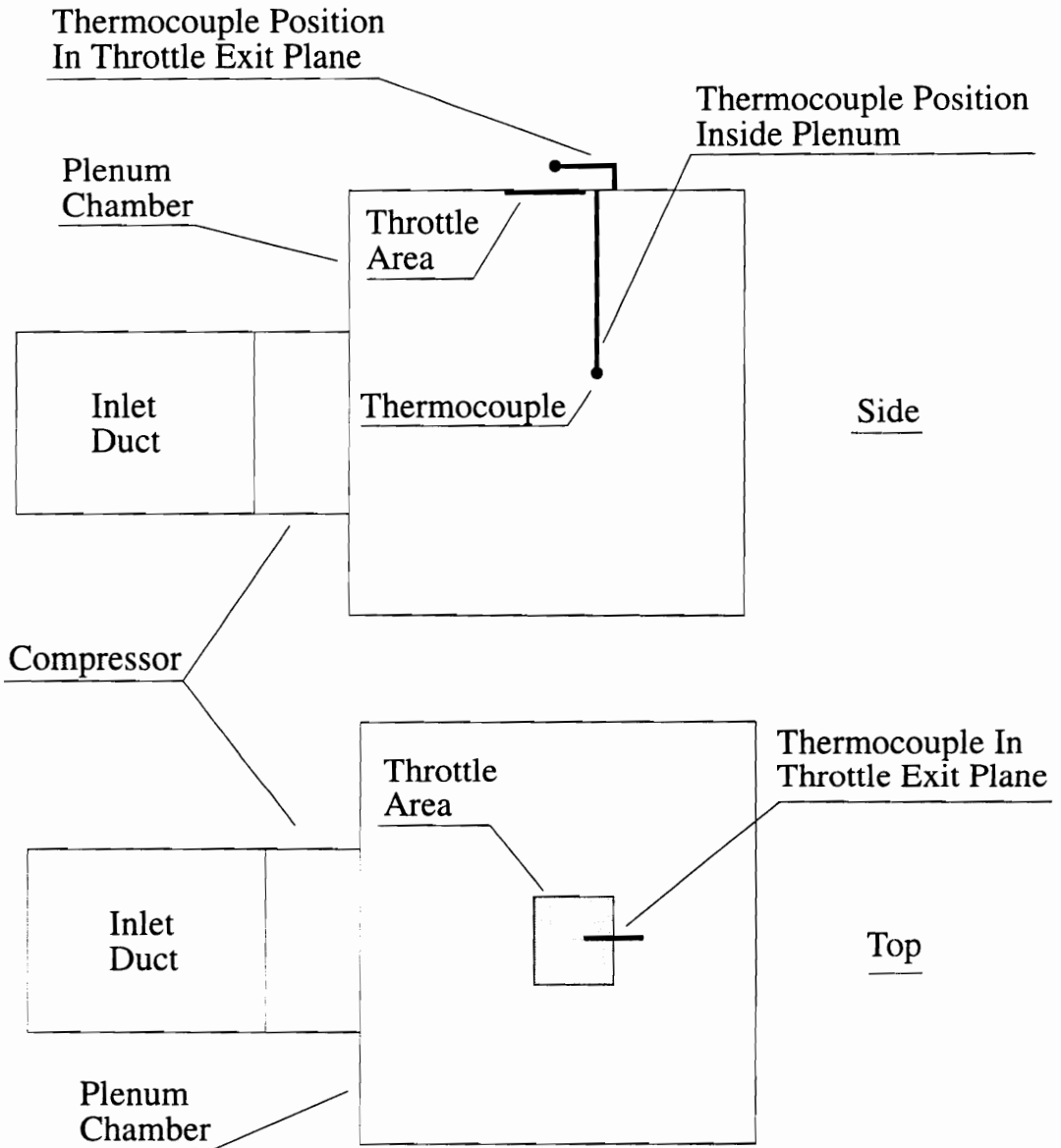


Figure 4.11 Thermocouple Position (Plenum)

4.8.3 Pressure Transducers

Three Datametrics Type 590 Integral Barocel pressure transducers and two OMEGA PX800-001GV high accuracy pressure transducers were used to obtain pressure data from the compression system. The Barocel pressure transducers were used to measure the pressure rise across the two stages of the compressor and to measure the total pressure in the throttle exit plane. The OMEGA pressure transducers were used to measure the static pressure in the plenum chamber and in the inlet duct.

Trial runs conducted with these pressure transducers verified that they were able to capture the phenomena of interest associated with the inlet temperature transient. These tests revealed a clear distinction between unstalled and stalled operation of the compressor. The pressures measured by the transducers were gage pressures. A pressure rise of zero was measured by the transducer when the transducer measured atmospheric pressure. This made these particular transducers excellent for measuring the low pressure rise across the compressor. The transducers were calibrated against a known pressure in the Mechanical Engineering Department Instrument Shop before installation. The pressure transducer calibration procedure is discussed in Appendix B.

A total pressure probe was positioned directly behind each of the two rotors in the compressor as shown in Figure 4.12. The probes were positioned in the casing such that they would measure the total pressure at the mean radius of each compressor rotor at the same circumferential location. A pressure transducer was positioned in the inlet duct to measure the static pressure in front of the first stage rotor as shown in Figure 4.12. A total pressure probe was positioned at the throttle exit plane and a static pressure tap was positioned on the plenum chamber as shown in Figure 4.13. Tygon tubing connected the pressure probes to the pressure transducers in the test cell.

Pressure Probe Position (Compressor)

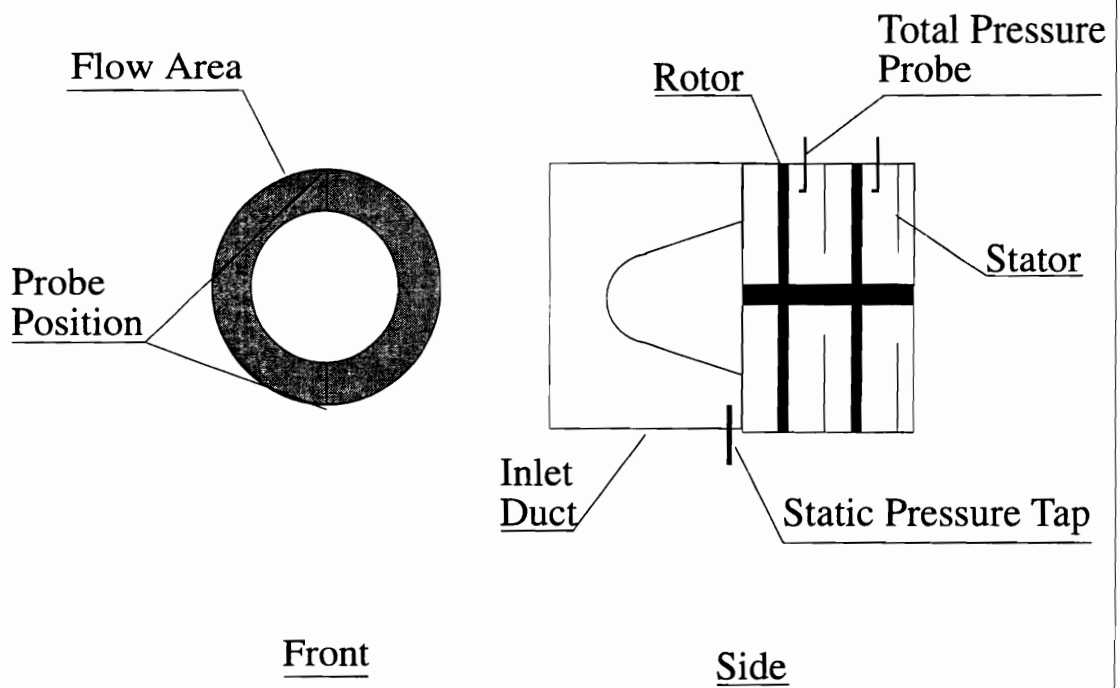


Figure 4.12 Pressure Probe Position (Compressor)

Pressure Probe Position

(Plenum Chamber)

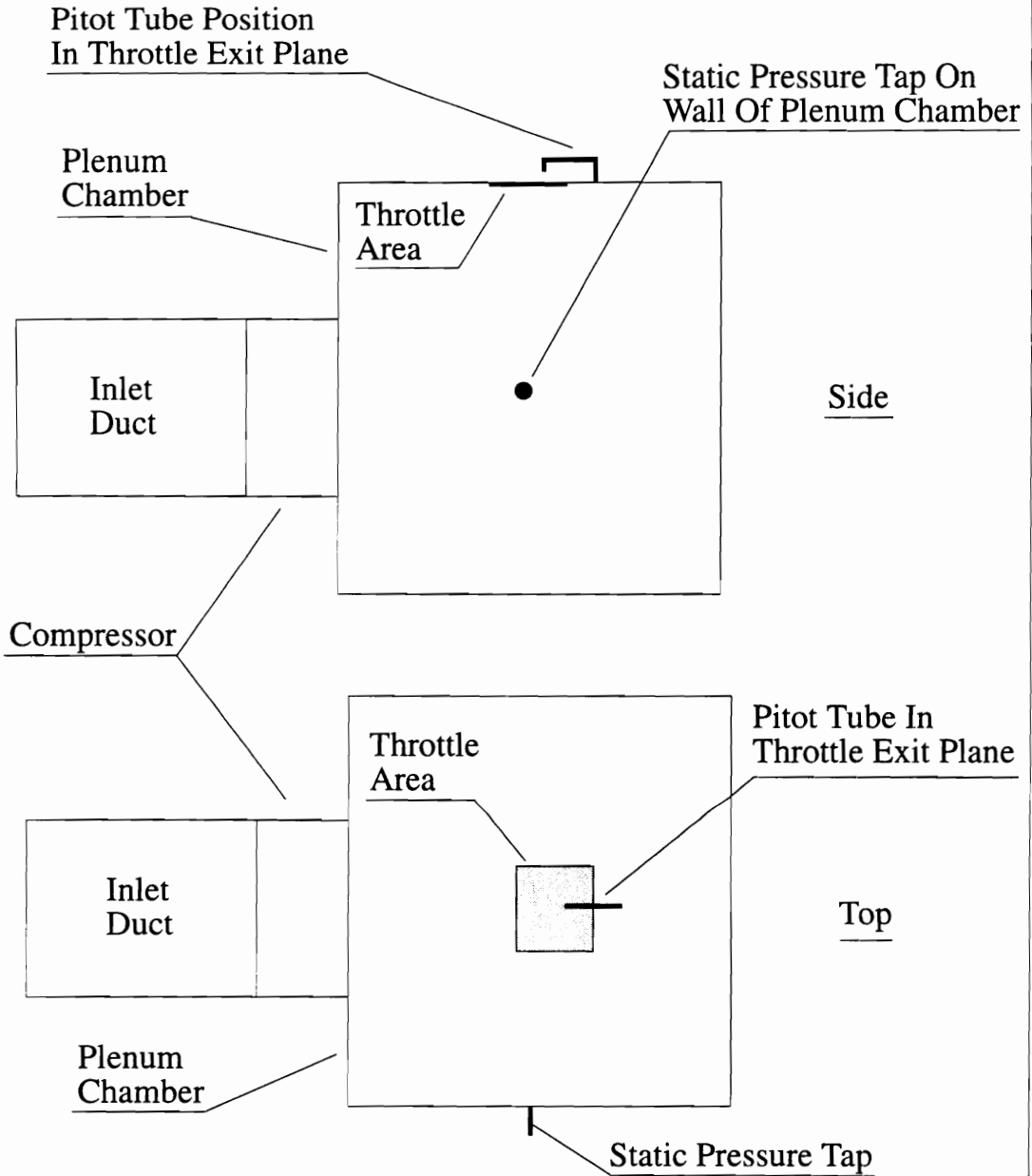


Figure 4.13 Pressure Probe Position (Plenum)

5. DATA REDUCTION AND ANALYSIS

Data from the compression system were collected from the pressure transducers and thermocouples as described in the Description Of Experiment chapter. The experiments were conducted and the data were analyzed using the following procedure.

Figure 5.1 is a schematic of the compression system with all data measuring stations identified with numbers. Station (1) represents the compressor inlet. Stations (2) and (3) represent the positions directly behind each of the two compressor stage rotors. Station (2) is behind the rotor of stage (1) and station (3) is behind the rotor of stage (2). Station (4) represents the plenum chamber and station (5) is the throttle exit plane.

As previously described in the Description Of Experiment chapter, two total pressure probes are positioned directly behind each of the two compressor stage rotors at the rotor mean radius. These probes measure the total pressure rise across each rotor. The pressure P02 is the total pressure rise for stage 1 and the pressure P03 is the total pressure rise for stage 2. The total pressure probe measuring stations are denoted as stations (2) and (3) in Figure 5.1. Using the inlet total pressure P01, the pressure ratios across each individual stage and the entire compressor are determined directly from the total pressure measurements by

$$\frac{P02}{P01} \quad (\text{compressor pressure ratio across stage 1})$$

$$\frac{P03}{P02} \quad (\text{compressor pressure ratio across stage 2})$$

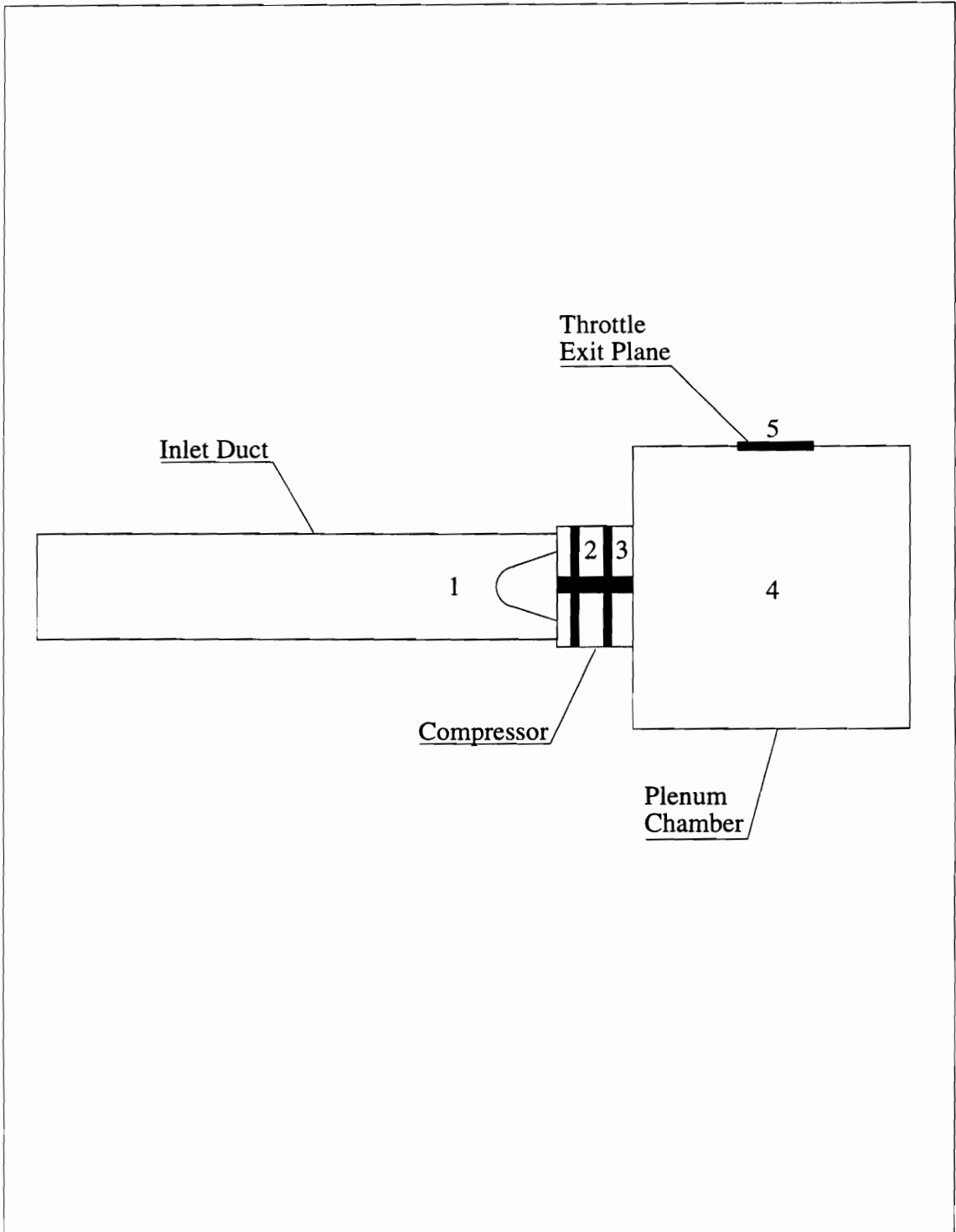


Figure 5.1 Compression System Data Measuring Stations

$$\frac{P03}{P01} \quad (\text{compressor pressure ratio across entire compressor})$$

Thermocouples are positioned around the circumference of the compressor in 60 degree circumferential increments as described in the Description Of Experiment chapter. Six thermocouples are positioned in front of stage 1 at station (1) in Figure 5.1 and six thermocouples are positioned in front of stage 2 at station (2) in Figure 5.1. The thermocouples extend into the compressor casing such that all temperature measurements are made at the compressor mean radius. The total temperatures obtained by each set of six thermocouples positioned in front of each stage are arithmetically averaged to obtain a stage inlet total temperature. T01 is the total temperature for stage 1 and T02 is the total temperature for stage 2.

The mass flow rate passing through the compression system \dot{m}_C is obtained by the measurements and procedure discussed in Appendix C. Using the mass flow rate and the inlet total pressures and temperatures obtained for each individual stage, the corrected mass flow rate for each individual stage is calculated from

$$\frac{\dot{m}_C \sqrt{\frac{T01}{T_{ref}}}}{\frac{P01}{P_{ref}}} \quad (\text{corrected mass flow rate for stage 1})$$

$$\frac{\dot{m}_C \sqrt{\frac{T02}{T_{ref}}}}{\frac{P02}{P_{ref}}} \quad (\text{corrected mass flow rate for stage 2})$$

Airflow velocities are extremely low in this experiment, and the flow is assumed to be incompressible. Therefore, total and static properties are considered to be equal. The flow density at the inlet to each stage is calculated using the ideal gas equation of state and the total properties according to

$$\rho_1 = \rho_{01} = \frac{P01}{R T01} \quad (\text{flow density at inlet to stage 1}) \quad (5.1)$$

$$\rho_2 = \rho_{02} = \frac{P02}{R T02} \quad (\text{flow density at inlet to stage 2}) \quad (5.2)$$

The mass flow rate, flow density, and constant compressor flow area allow the axial flow velocity at the inlet to each stage to be calculated from the mass flow rate equation according to

$$V_{x1} = \frac{\dot{m}_C}{\rho_1 A_C} \quad (\text{axial flow velocity at inlet to stage 1 at compressor mean radius}) \quad (5.3)$$

$$V_{x2} = \frac{\dot{m}_C}{\rho_2 A_C} \quad (\text{axial flow velocity at inlet to stage 2 at compressor mean radius}) \quad (5.4)$$

The axial velocities represent average axial flow velocities at the compressor mean radius where all data measurements occur. The compressor rotor blade velocity is calculated at the compressor mean radius according to

$$U_1 = U_2 = \Omega r_{\text{mean}} \quad (\text{rotor blade velocity at rotor mean radius}) \quad (5.5)$$

Since both rotors have identical geometry, the rotor blade velocity U calculated at the compressor mean radius is identical for both stages.

The isentropic speed of sound is calculated at the inlet to each stage using the inlet total temperature for each stage according to

$$a_1 = \sqrt{\gamma RT_{01}} \quad (\text{isentropic speed of sound at the inlet of stage 1}) \quad (5.6)$$

$$a_2 = \sqrt{\gamma RT_{02}} \quad (\text{isentropic speed of sound at the inlet of stage 2}) \quad (5.7)$$

Using the axial flow velocity, rotor blade mean radius velocity, and the isentropic speed of sound calculated for each individual stage, the corresponding axial flow and rotor Mach numbers are calculated at the compressor mean radius according to

$$Mv_{x1} = \frac{V_{x1}}{a_1} \quad (\text{axial flow Mach number at inlet to stage 1 at mean radius}) \quad (5.8)$$

$$Mv_{x2} = \frac{V_{x2}}{a_2} \quad (\text{axial flow Mach number at inlet to stage 2 at mean radius}) \quad (5.9)$$

$$Mu_1 = \frac{U_1}{a_1} \quad (\text{rotor Mach number at compressor mean radius for stage 1}) \quad (5.10)$$

$$Mu_2 = \frac{U_2}{a_2} \quad (\text{rotor Mach number at compressor mean radius for stage 2}) \quad (5.11)$$

The corresponding compressor rotor blade Mach number triangle can be constructed from the Mach numbers calculated at the compressor mean radius and is shown conceptually in Figure 5.2.

The compressor rotor blade incidence for each individual stage can be calculated at the compressor mean radius according to

$$\beta_1 = \tan^{-1} \left[\frac{Mu_1}{Mv_{x1}} \right] \quad (\text{rotor blade incidence for stage 1 at mean radius}) \quad (5.12)$$

$$\beta_2 = \tan^{-1} \left[\frac{Mu_2}{Mv_{x2}} \right] \quad (\text{rotor blade incidence for stage 2 at mean radius}) \quad (5.13)$$

The chordline for the rotor blades on the axial flow compressor used in this experiment is the bottom surface of the airfoil as shown by the airfoil cross section in the Description Of Experiment chapter. The geometric stagger angle ξ is the geometric angle between the blade chordline and the rotor rotational axis as shown in Figure 5.2. Therefore, the angle between the chordline and the relative Mach number vector Mw , which is the blade angle of attack α , can be calculated from the blade incidence and the stagger angle for each individual stage of the compressor according to

$$\alpha_1 = \beta_1 - \xi_1 \quad (\text{rotor blade angle of attack for stage 1 at mean radius}) \quad (5.14)$$

$$\alpha_2 = \beta_2 - \xi_2 \quad (\text{rotor blade angle of attack for stage 2 at mean radius}) \quad (5.15)$$

These angles of attack are the angles of attack for each individual stage at the compressor mean radius.

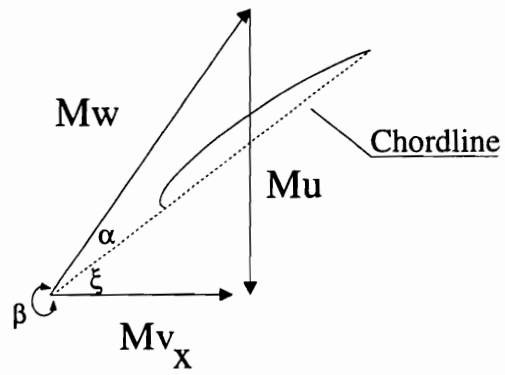


Figure 5.2 Rotor Blade Chordline/Stagger Angle

6. RESULTS AND DISCUSSION

Five experiments were conducted to demonstrate compression system dynamic response to inlet temperature transients and to test the two hypotheses developed in chapter 3. The first two experiments involved a compressor rotating stall recovery with the compressor initially operating in rotating stall. In the first experiment, recovery from rotating stall was induced and in the second experiment recovery was not obtained and the compression system remained in rotating stall operation. The third and fourth experiments involved a compressor stall with the compressor initially operating unstalled. In the third experiment, a successful rotating stall was induced and in the fourth experiment the compressor was not driven into rotating stall operation. The fifth experiment involved an induced compressor rotating stall followed by an immediate recovery from the rotating stall operating condition.

The shapes of the curves for rotor blade angle of attack are identical to the shapes of the curves for rotor blade incidence contained in Appendix A. This is due to the fact that there is only a geometrical relationship between rotor blade incidence and rotor blade angle of attack. Therefore, the trends observed for rotor blade angle of attack will be identical to the trends for rotor blade incidence.

Equation (3.2) applies along the entire span of the rotor blade where the rotor and axial flow Mach numbers vary with blade radius. Therefore, rotor blade incidence and rotor blade angle of attack also vary along the entire span of the rotor blade. To determine how rotor blade incidence and rotor blade angle of attack vary during an inlet temperature

transient, a specific rotor blade radius was selected for the data analysis. The compressor mean radius was selected as the logical location to apply equation (3.2) for these experiments to evaluate rotor blade incidence and rotor blade angle of attack. Data taken at a particular rotor blade radius identifies how rotor blade incidence and rotor blade angle of attack vary during an inlet temperature transient.

6.1 Rotating Stall Recovery

The first experiment conducted was a compressor rotating stall recovery induced by an inlet temperature transient. Figure 6.1 identifies the compressor performance map for the overall compressor. The performance map shows the transient path taken by the operating point during the transient inlet temperature excursion. The inlet temperature transient applied can be seen in Figures 6.2, 6.3, 6.4, and 6.5. The compressor was initially operating in rotating stall, at point (A) on the 80 % post-stall corrected speed characteristic, when energy was added to the compression system in the form of an inlet temperature transient. The dynamic response of the compression system moved the operating point towards and beyond the recovery line to point (B), which induced rotating stall recovery. The operating point then moved to the 80 % prestall corrected speed characteristic to point (C) as the inlet temperature decayed back to the ambient temperature.

Metric Conversions

$$\frac{\text{kg}}{\text{s}} = \frac{\text{lbm}}{\text{sec}} (0.45359237)$$

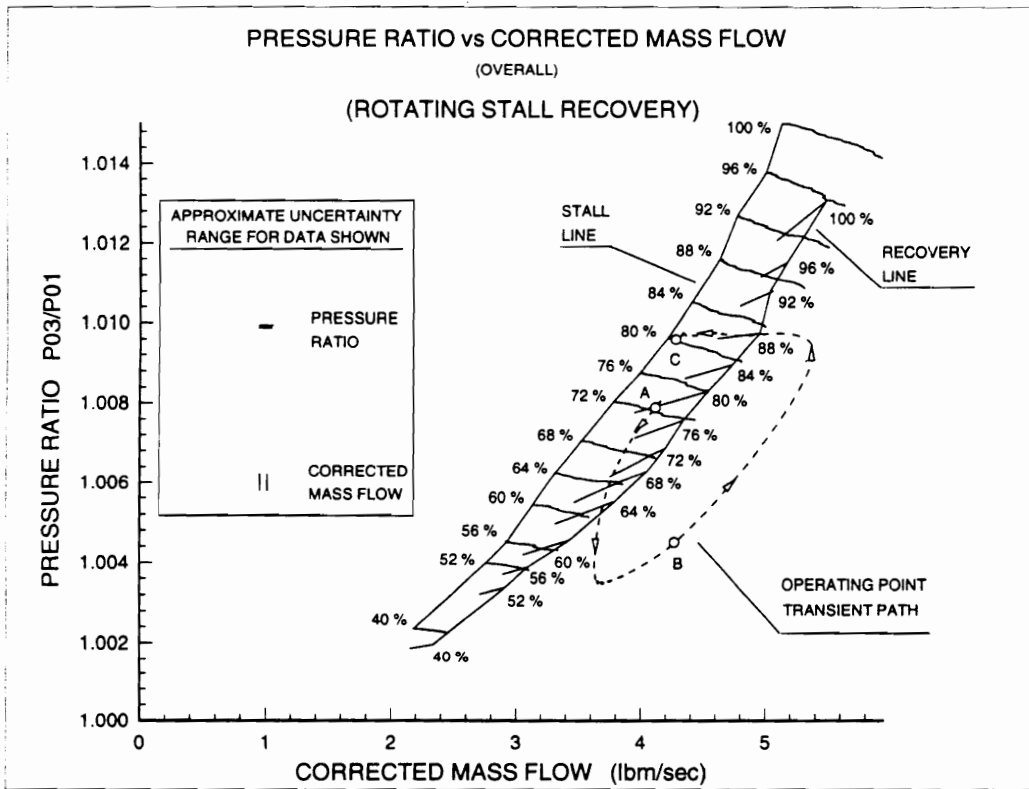


Figure 6.1 Compressor Performance Map (Overall)
(Rotating Stall Recovery)

Metric Conversions

$$K = 273.0 + \frac{5}{9} [R - 492.0]$$

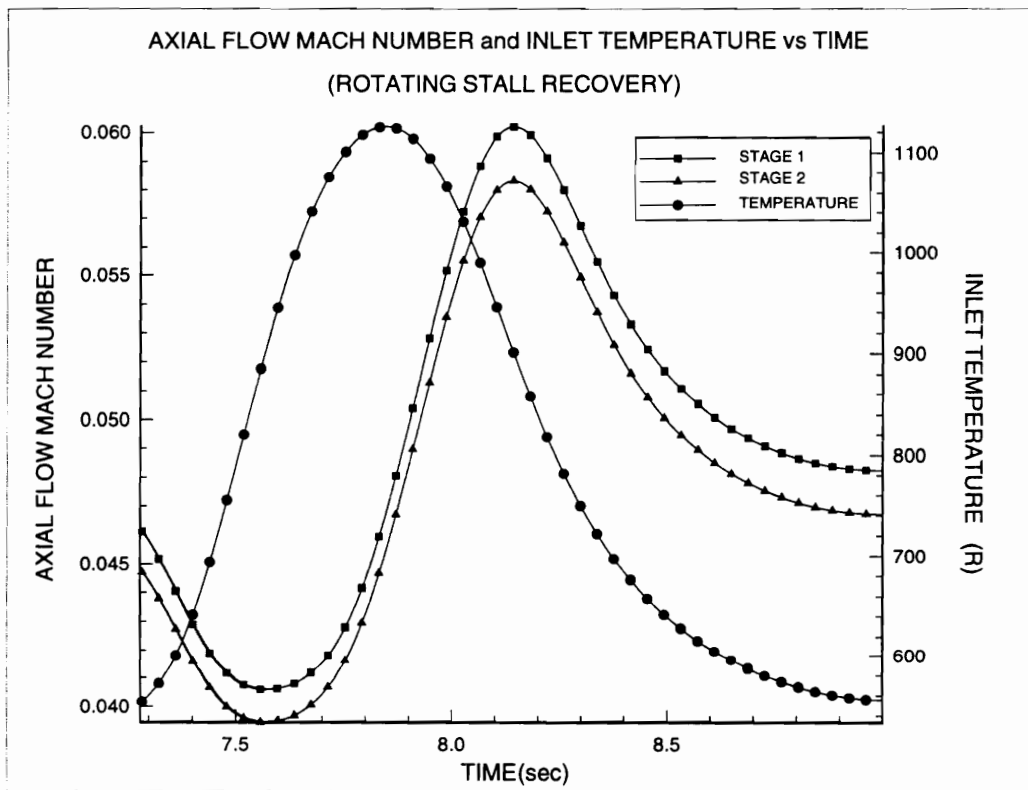


Figure 6.2 Axial Flow Mach Number and Inlet Temperature vs Time
(Rotating Stall Recovery)

Metric Conversions

$$K = 273.0 + \frac{5}{9}[R - 492.0]$$

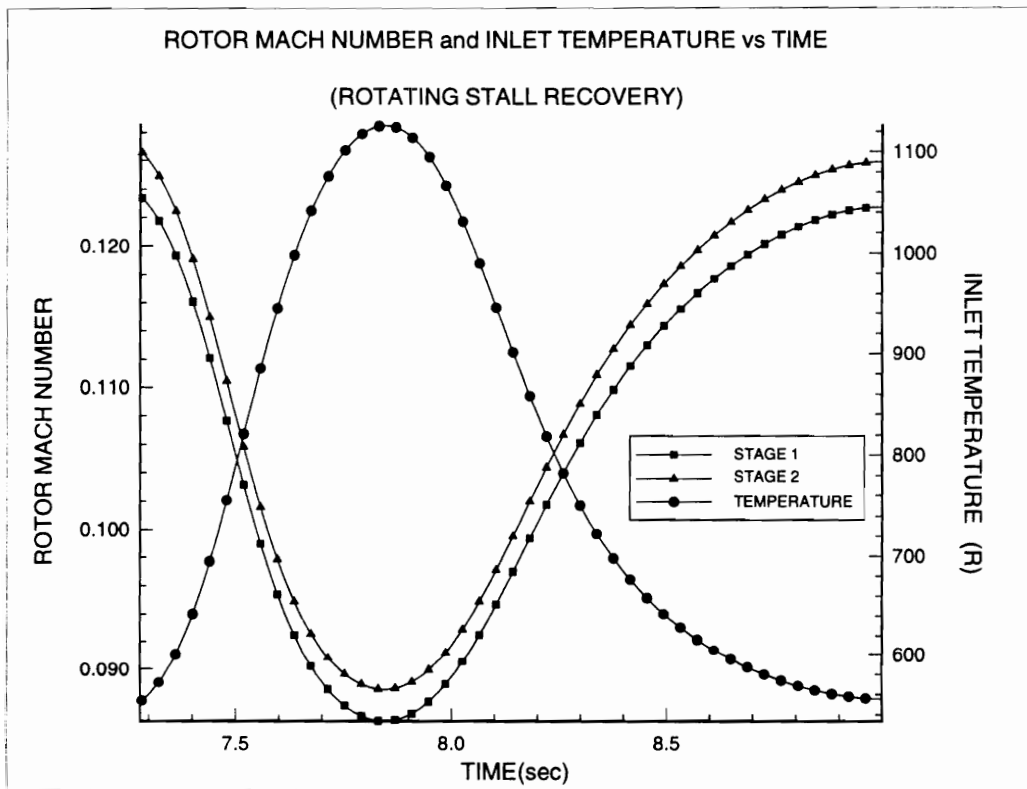


Figure 6.3 Rotor Mach Number and Inlet Temperature vs Time (Rotating Stall Recovery)

Metric Conversions

$$K = 273.0 + \frac{5}{9}[R - 492.0]$$

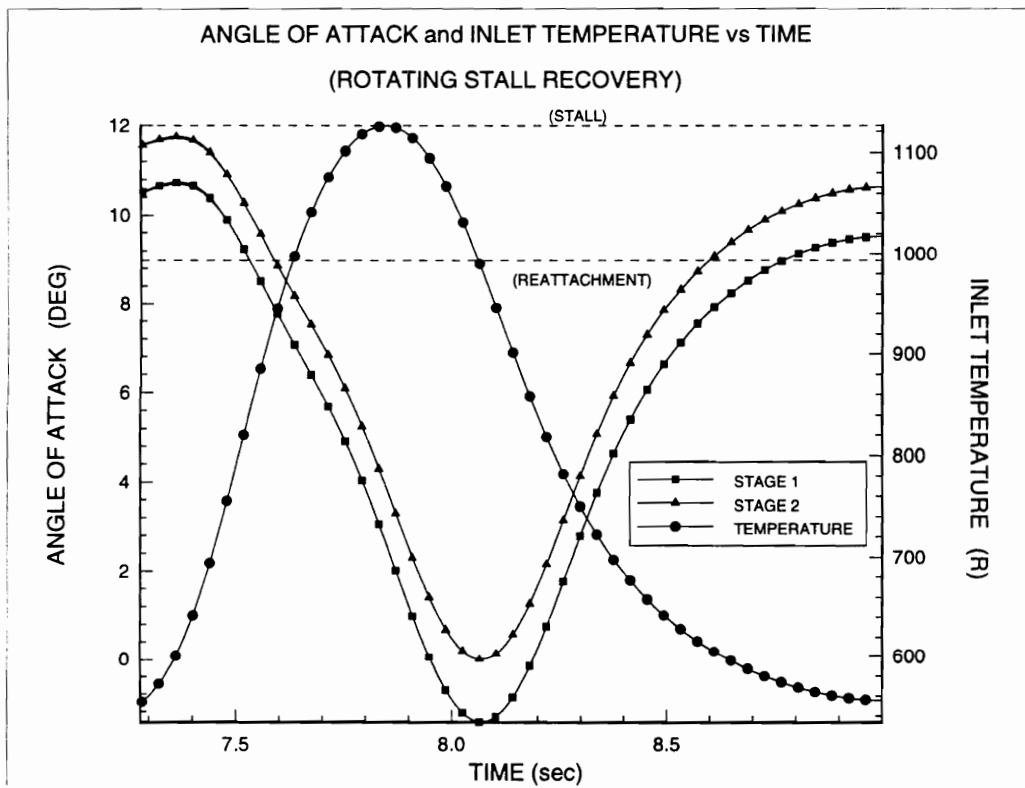


Figure 6.4 Blade Angle of Attack and Inlet Temperature vs Time (Rotating Stall Recovery)

Metric Conversions

$$K = 273.0 + \frac{5}{9}[R - 492.0]$$

$$\frac{N}{m} = \frac{\text{lbf}}{\text{ft}} (47.87488)$$

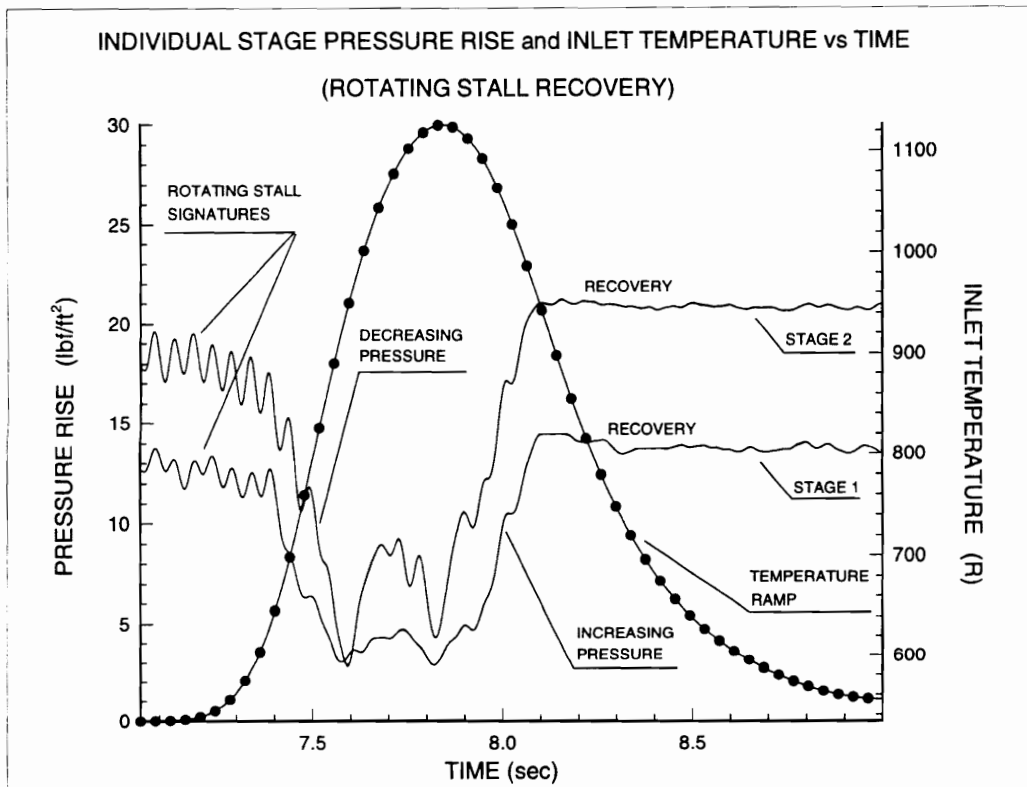


Figure 6.5 Individual Stage Pressure Rise and Inlet Temperature vs Time (Rotating Stall Recovery)

During the beginning part of the inlet temperature transient, corrected mass flow and corrected speed initially decreased as the inlet temperature increased. This is shown by the path of the process identified in Figure 6.1. This implies that the axial flow and rotor Mach numbers also decreased, as shown by the data results of Figure 6.2 and Figure 6.3. Figure 6.2 is a plot of calculated axial flow Mach number and inlet temperature versus time for stages one and two at the compressor mean radius. Figure 6.3 is a plot of calculated rotor Mach number and inlet temperature versus time for stages one and two at the compressor mean radius.

As the operating point began to move toward the recovery line to point (B) on Figure 6.1, it was observed that corrected mass flow rate began to increase. This implies that axial flow Mach number began to increase. This is supported by the data taken at the compressor mean radius in Figure 6.2. During this part of the compression system dynamic response, there was a significant change in the rotor blade Mach number triangle because axial flow Mach number increased sooner, and at a faster rate than rotor Mach number as shown by the data taken at the compressor mean radius in Figure 6.2 and Figure 6.3. This caused a transient decrease in rotor blade incidence and rotor blade angle of attack as shown by the results in Figure 6.4. When the operating point reached the recovery line on Figure 6.1, the rotor blade incidence and rotor blade angle of attack had been reduced sufficiently to cause the stalled flow to reattach to the rotor blade surface by definition of the recovery line. According to the energized compression system dynamic response hypothesis for rotating stall recovery, driving the operating point across the

recovery line implies that the rotor blade incidence and rotor blade angle of attack will have been sufficiently reduced to allow stalled flow reattachment.

Figure 6.4 is a plot of calculated rotor blade angle of attack and inlet temperature versus time for stages one and two at the compressor mean radius. Identified on this plot are the maximum angle of attack for stall for this particular rotor blade airfoil cross section, and the angle at which the rotor blade angle of attack must be reduced to allow the stalled flow to reattach to the rotor blade surface following stall. This information can be found in reference (17). This plot clearly demonstrates that the transient rotor blade angle of attack decreased at the compressor mean radius for both stages during the temperature excursion. In fact, the transient rotor blade angle of attack decreased by approximately 10 degrees for both stages, crossing the threshold necessary for the stalled flow to reattach to the rotor blade surface. With such a large decrease in rotor blade angle of attack, the compressor would be expected to recover from the rotating stall operating condition. This fact is verified by Figure 6.1 which identifies the operating point returning to the 80 % prestall corrected speed characteristic.

Figure 6.5 is a plot of individual stage pressure rise and inlet temperature versus time for stages one and two of the compressor during the inlet temperature transient. This plot clearly shows that both stages are initially stalled. The rotating stall signatures are clearly identified for both stages. It can be seen that individual stage pressure rise begins to decrease for both stages as the compressor inlet temperature increases. This is due to the fact that the density of the working fluid decreases as the inlet temperature increases. As the inlet temperature begins to decay back to the ambient temperature, individual stage

pressure rise begins to increase for both stages. Upon return of the inlet temperature back to the ambient temperature, it can be seen that individual stage pressure rise for both stages is higher than before the temperature transient was applied across the compressor inlet. The rotating stall signatures have vanished from both stages, indicating that both stages recovered from the rotating stall operating condition.

The results shown in Figures 6.1, 6.4, and 6.5 support the energized compression system dynamic response rotating stall recovery hypothesis. They clearly demonstrate that energizing a compression system operating in rotating stall with an inlet temperature excursion can induce a dynamic response that drives the operating point across the recovery line. The results also illustrate that the crossing of the recovery line by the operating point during the energized dynamic response implies that the rotor blade flow angle of attack will have been sufficiently reduced to allow the compression system to recover from the rotating stall operating condition.

6.2 No Rotating Stall Recovery

A second experiment was conducted with the compressor initially operating in rotating stall at 80 % post-stall corrected speed, as in the first experiment. This second experiment demonstrated that if the operating point did not cross the recovery line during an energized compression system dynamic response, the compressor would not recover from the rotating stall operating condition. Figure 6.6 shows the compressor performance map for the overall compressor. The performance map shows the transient path taken by

the operating point during the transient inlet temperature excursion of the second experiment. The inlet temperature transient applied can be seen in Figures 6.7, 6.8, 6.9, and 6.10. The compressor was initially operating in rotating stall, on the 80 % post-stall corrected speed characteristic at point (A), when energy was deliberately added to the compression system in the form of a low level inlet temperature transient. The dynamic response of the compression system moved the operating point down, and back to point (A) after the inlet temperature transient decayed back to the ambient temperature. Returning to point (A), the compression system continued to operate in rotating stall on the 80 % post-stall corrected speed characteristic.

In this situation, the inlet temperature transient was not sufficient in magnitude to energize a dynamic response from the compression system that would drive the operating point beyond the recovery line. This is shown by the path of the process in Figure 6.6. The failure of the operating point to reach the recovery line during the compression system dynamic response implies that the rotor blade incidence and rotor blade angle of attack were not reduced sufficiently during the transient to relieve the rotor blade of the stalled flow condition by definition of the recovery line. Figure 6.7 shows the calculated axial flow Mach number and inlet temperature versus time for stages one and two at the compressor mean radius. Figure 6.8 shows the calculated rotor Mach number and inlet temperature versus time for stages one and two at the compressor mean radius. Figure 6.7 and Figure 6.8 reveal relatively small changes in axial flow and rotor Mach numbers at

Metric Conversions

$$\frac{\text{kg}}{\text{s}} = \frac{\text{lbm}}{\text{sec}} (0.45359237)$$

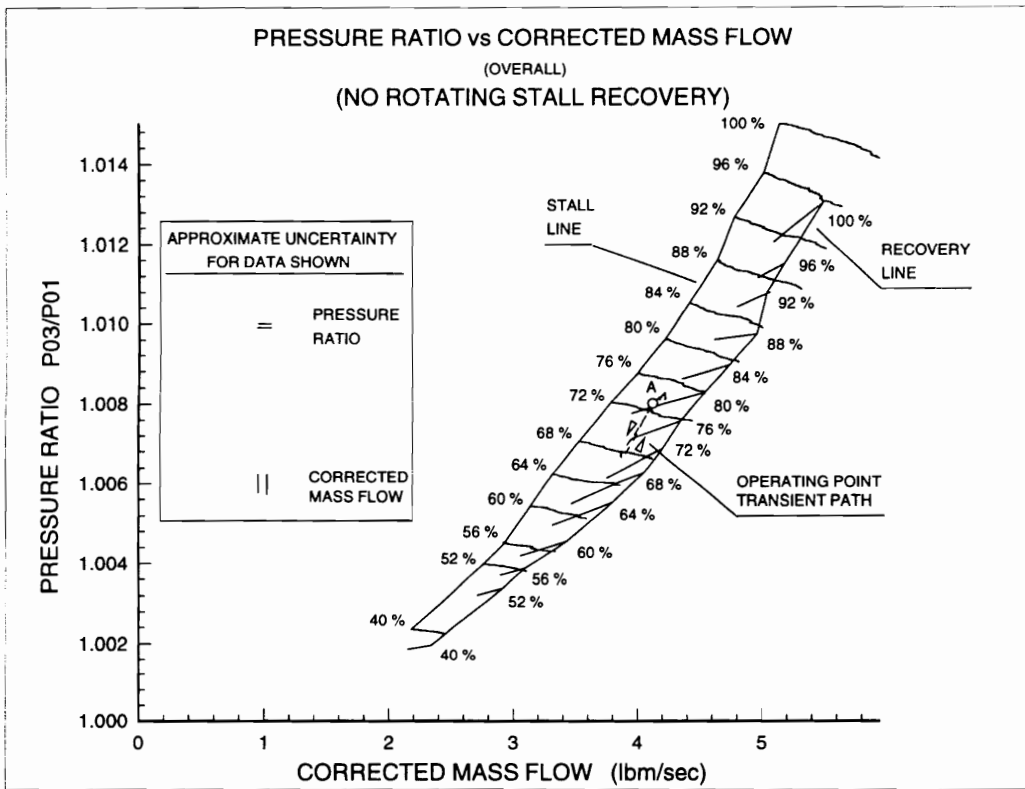


Figure 6.6 Compressor Performance Map (Overall)
(No Rotating Stall Recovery)

Metric Conversions

$$K = 273.0 + \frac{5}{9}[R - 492.0]$$

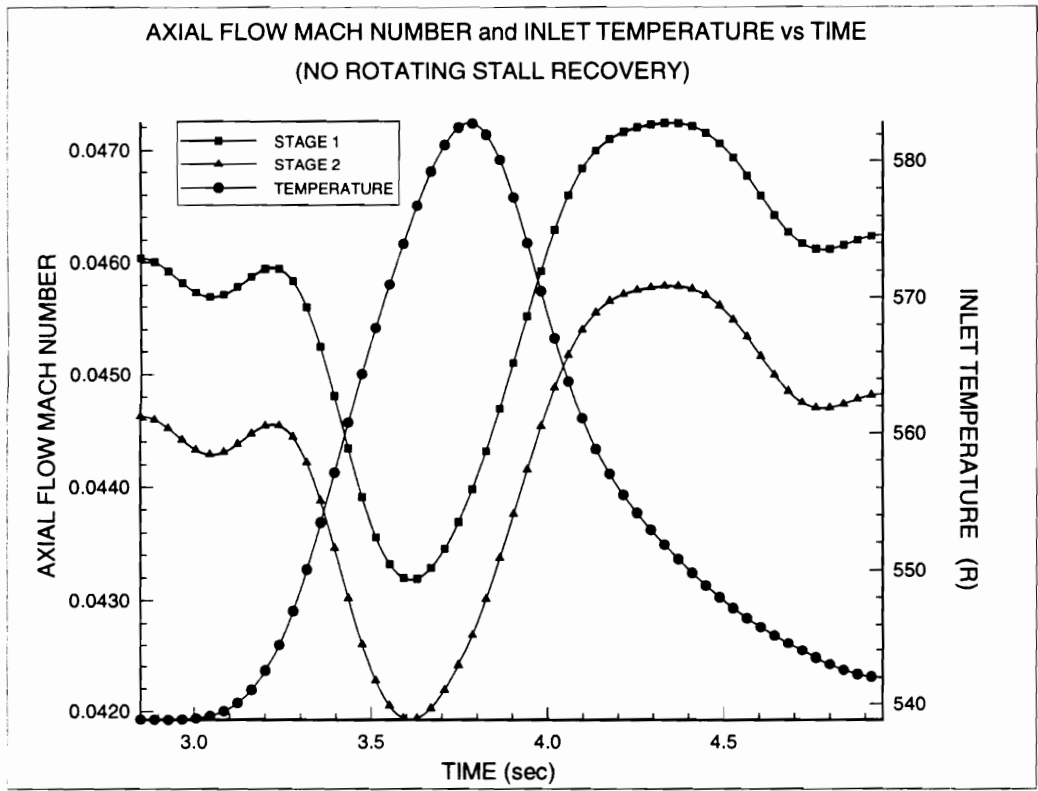


Figure 6.7 Axial Flow Mach Number and Inlet Temperature vs Time (No Rotating Stall Recovery)

Metric Conversions

$$K = 273.0 + \frac{5}{9}[R - 492.0]$$

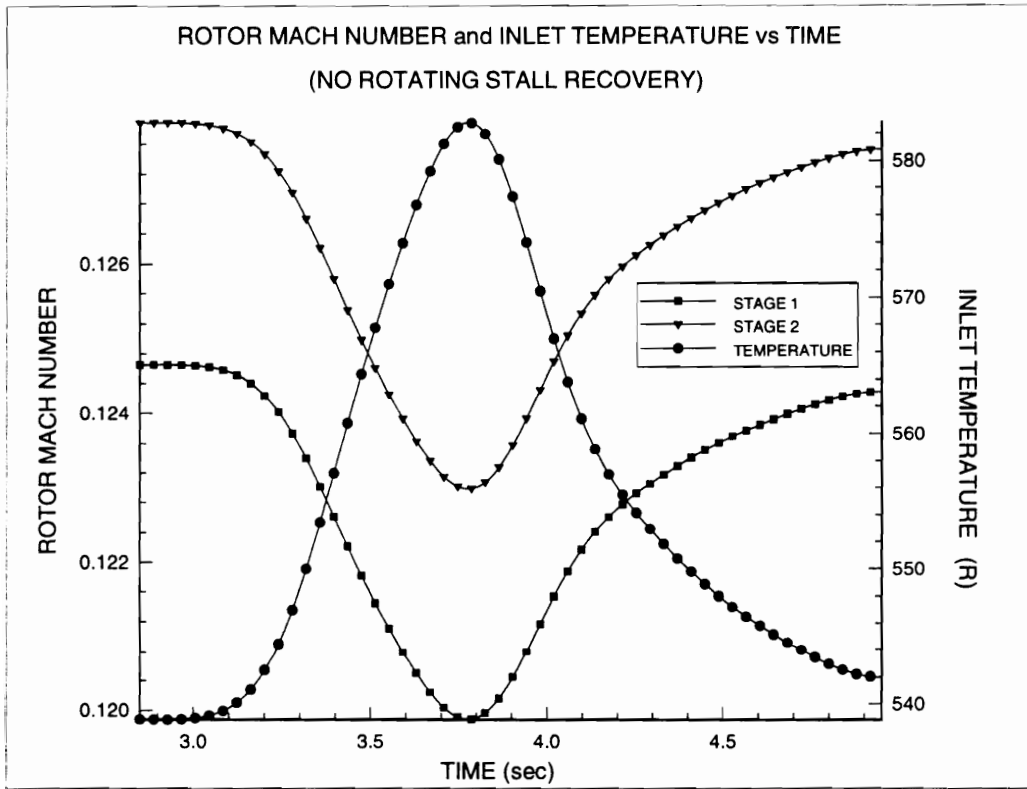


Figure 6.8 Rotor Mach Number and Inlet Temperature vs Time (No Rotating Stall Recovery)

Metric Conversions

$$K = 273.0 + \frac{5}{9}[R - 492.0]$$

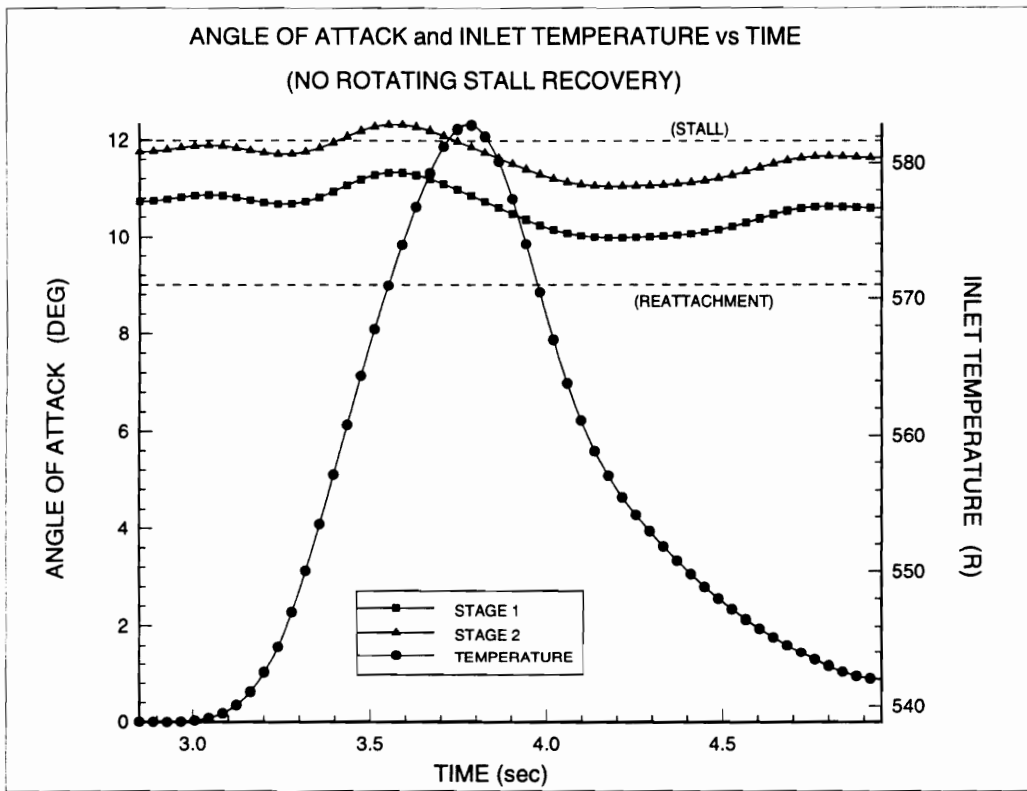


Figure 6.9 Blade Angle of Attack and Inlet Temperature vs Time
(No Rotating Stall Recovery)

Metric Conversions

$$K = 273.0 + \frac{5}{9}[R - 492.0]$$

$$\frac{N}{m} = \frac{lbf}{ft} (47.87488)$$

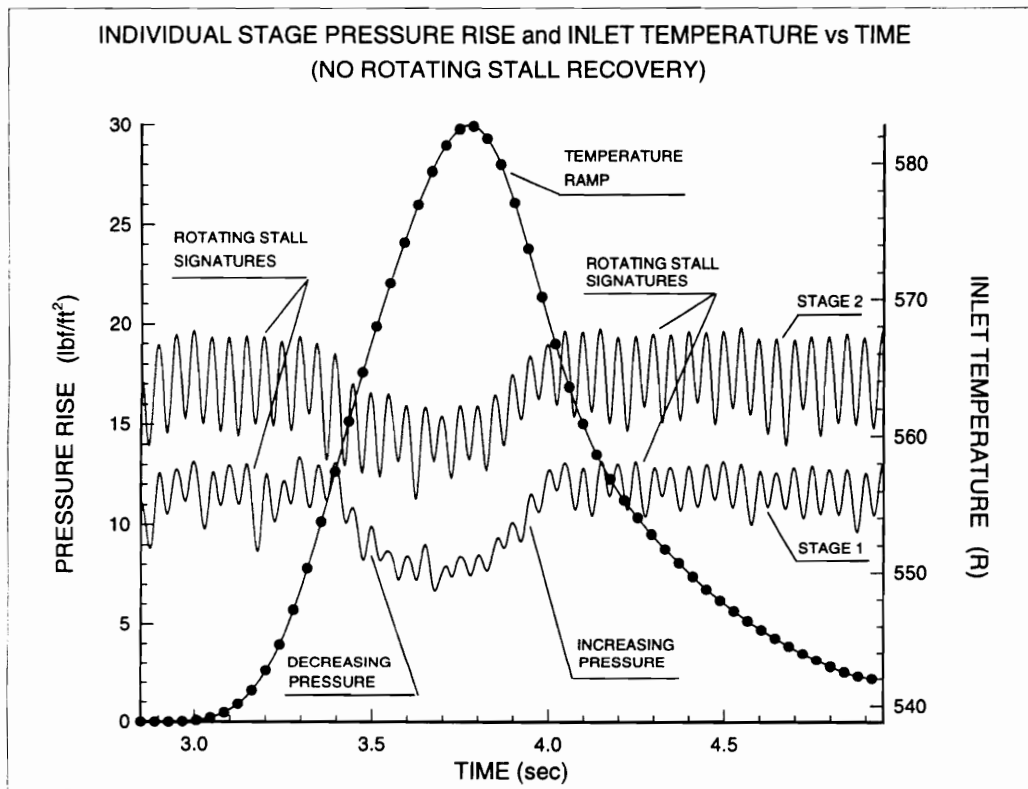


Figure 6.10 Individual Stage Pressure Rise and Inlet Temperature vs Time (No Rotating Stall Recovery)

the compressor mean radius. Therefore, there was not a significant transient change in the rotor blade Mach number triangle for this process.

Figure 6.9 is a plot of calculated rotor blade angle of attack and inlet temperature versus time for stages one and two at the compressor mean radius. This plot clearly demonstrates that the rotor blade angle of attack decreased for both stages at the compressor mean radius during the temperature excursion. However, the rotor blade angle of attack did not cross the threshold necessary for the stalled flow to reattach to the rotor blade surface. This implies that the compressor may not have recovered from the rotating stall operating condition. This fact is verified by Figure 6.6, which shows the operating point returning to the initial operating point position on the 80 % post-stall corrected speed characteristic.

Figure 6.10 is a plot of individual stage pressure rise and inlet temperature versus time for stages one and two of the compressor during the inlet temperature transient. This plot clearly shows that both stages are initially stalled. The rotating stall signatures are clearly identified for both stages. As seen with the larger inlet temperature transient, individual stage pressure rise begins to decrease for both stages as the compressor inlet temperature increases. As stated before, this is due to the fact that the density of the working fluid decreases as the inlet temperature increases. As the inlet temperature begins to decay back to the ambient temperature, individual stage pressure rise begins to increase for both stages. Upon return of the inlet temperature back to the ambient temperature, it can be seen that both stages continue to operate in rotating stall. Rotating stall signatures

are clearly identified for both stages indicating that the stages did not recover from the rotating stall operating condition.

The results of Figures 6.6, 6.9, and 6.10 for the second experiment, also provide support for the energized compression system dynamic response rotating stall recovery hypothesis. They clearly demonstrate that if insufficient energy is added to a compression system operating in rotating stall in the form of an inlet temperature excursion, the dynamic response may not drive the operating point across the recovery line. This implies that the transient decrease in rotor blade flow angle of attack will not be sufficient to allow the compression system to recover from the rotating stall operating condition.

6.3 Rotating Stall

In the third experiment conducted, a rotating stall was induced by an inlet temperature transient. Figure 6.11 identifies the compressor performance map for the overall compressor. The performance map shows the transient path taken by the operating point during the transient inlet temperature excursion. The inlet temperature transient applied can be seen in Figures 6.12, 6.13, 6.14, and 6.15. The compressor was initially operating on the 80 % prestall corrected speed characteristic at point (A), when energy was added to the compression system in the form of an inlet temperature transient. The dynamic response of the compression system moved the operating point across the stall line inducing rotating stall. As the inlet temperature decayed back to the ambient

Metric Conversions

$$\frac{\text{kg}}{\text{s}} = \frac{\text{lbm}}{\text{sec}} (0.45359237)$$

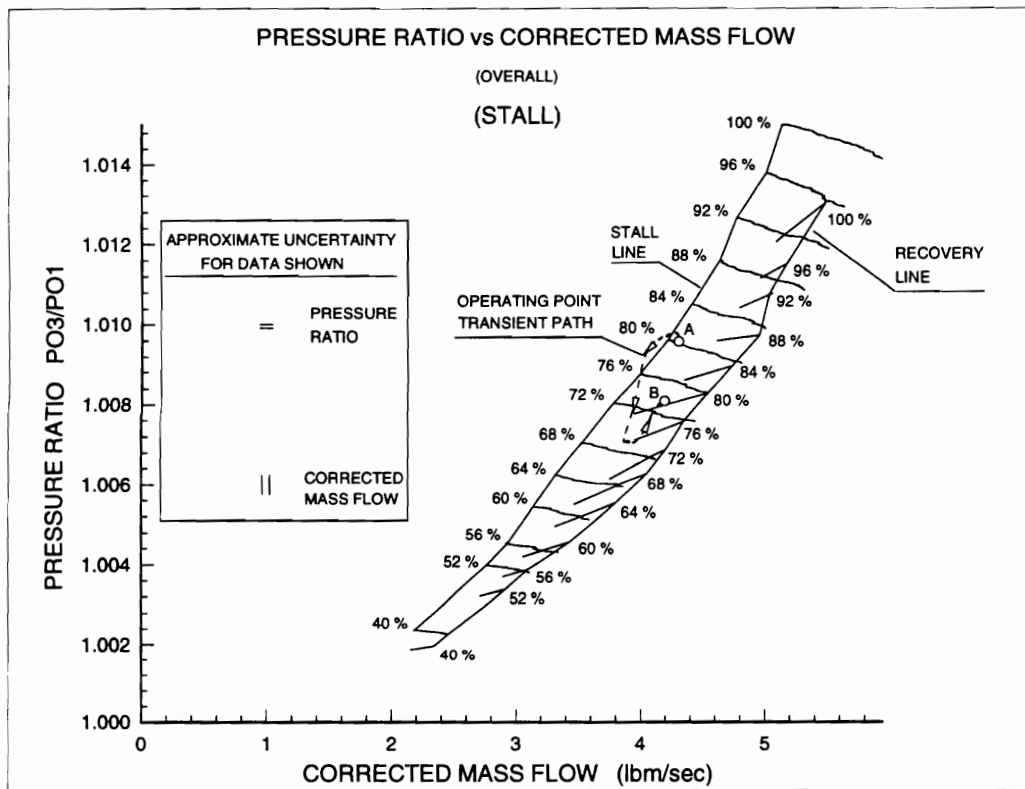


Figure 6.11 Compressor Performance Map (Overall)
(Stall)

Metric Conversions

$$K = 273.0 + \frac{5}{9}[R - 492.0]$$

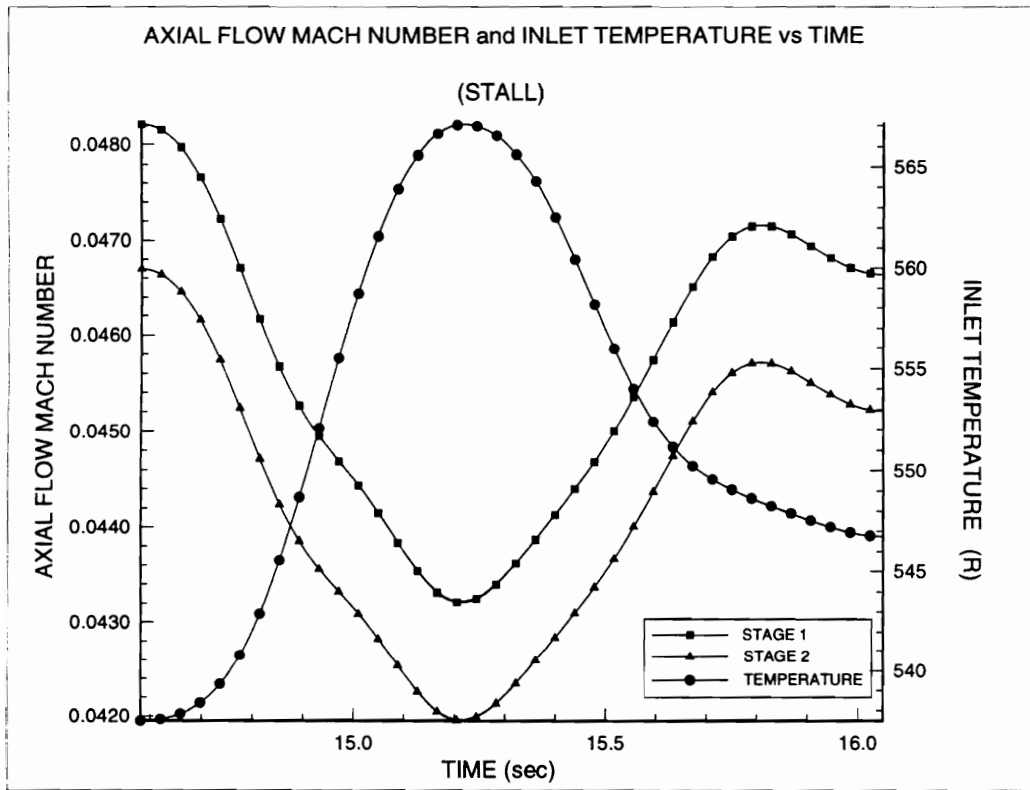


Figure 6.12 Axial Flow Mach Number and Inlet Temperature vs Time (Stall)

Metric Conversions

$$K = 273.0 + \frac{5}{9}[R - 492.0]$$

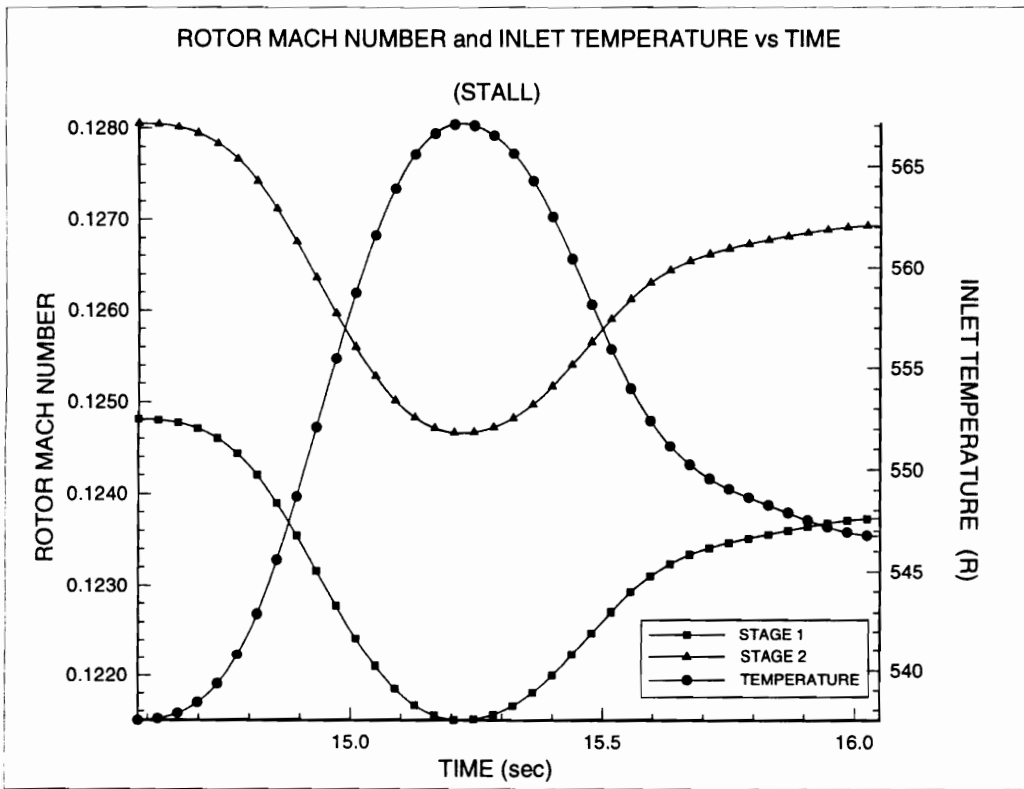


Figure 6.13 Rotor Mach Number and Inlet Temperature vs Time (Stall)

Metric Conversions

$$K = 273.0 + \frac{5}{9}[R - 492.0]$$

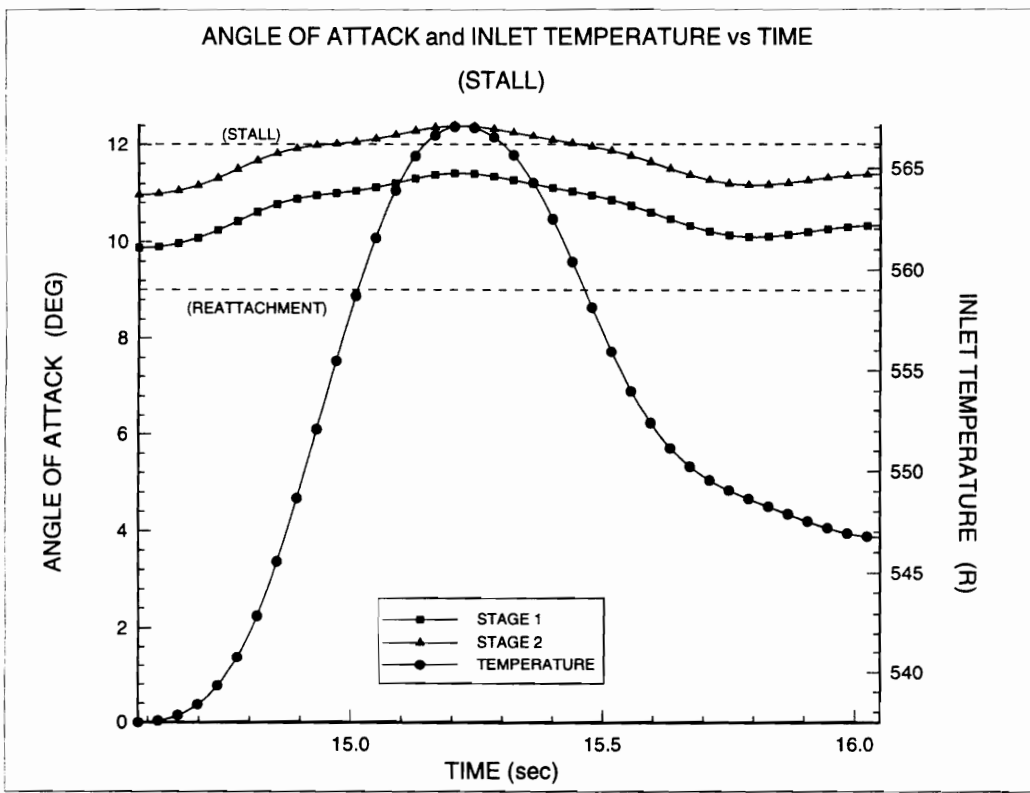


Figure 6.14 Blade Angle of Attack and Inlet Temperature vs Time (Stall)

Metric Conversions

$$K = 273.0 + \frac{5}{9}[R - 492.0]$$

$$\frac{N}{m} = \frac{lbf}{ft} (47.87488)$$

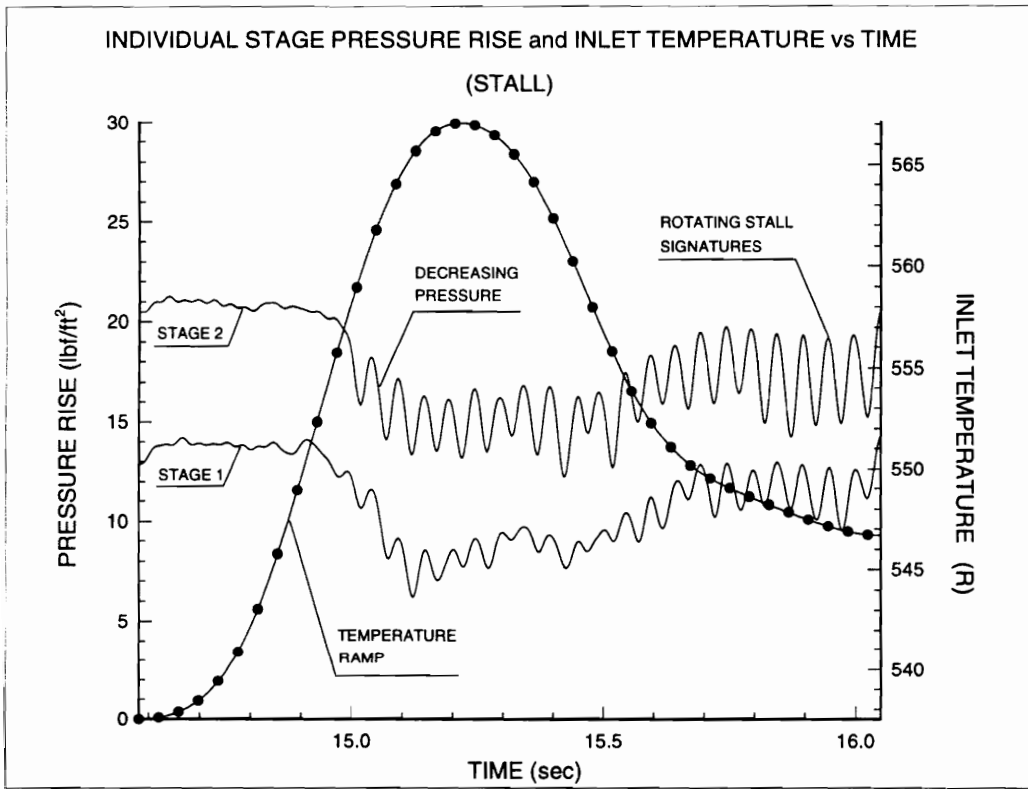


Figure 6.15 Individual Stage Pressure Rise and Inlet Temperature vs Time (Stall)

temperature, the operating point settled on the corresponding 80 % post-stall corrected speed characteristic at point (B).

During the inlet temperature transient, corrected mass flow rate and corrected speed decreased as the inlet temperature increased and drove the operating point across the stall line. This is shown by the path of the process in Figure 6.11. This implies that the axial flow and rotor Mach numbers also decreased as the inlet temperature increased. This fact was verified by the experimental data plots of Figures 6.12 and 6.13. Figure 6.12 is a plot of calculated axial flow Mach number and inlet temperature versus time for stages one and two at the compressor mean radius. The figure shows that axial flow Mach number decreased for both stages at the compressor mean radius as the inlet temperature increased. Figure 6.13 is a plot of calculated rotor Mach number and inlet temperature versus time for stages one and two at the compressor mean radius. Again, it is seen that rotor Mach number also decreased for both stages at the compressor mean radius as the inlet temperature increased. It is observed from Figures 6.12 and 6.13 that axial flow Mach number decreased sooner, and at a faster rate than rotor Mach number at the compressor mean radius. This implies that the rotor blade Mach number triangle changed causing a transient increase in rotor blade incidence and rotor blade angle of attack as shown by the results in Figure 6.14. When the operating point reached the stall line, the rotor blade incidence and rotor blade angle of attack had been increased sufficiently to cause the flow to separate from the rotor blade surface and stall by definition of the stall line. According to the energized compression system dynamic response hypothesis for rotating stall, driving the operating point across the stall line implies that the rotor blade

incidence and rotor blade angle of attack will have been sufficiently increased to cause stall.

Figure 6.14 is a plot of calculated rotor blade angle of attack and inlet temperature versus time for stages one and two at the compressor mean radius. This plot clearly demonstrates that the rotor blade angle of attack increased for both stages at the compressor mean radius during the temperature excursion, crossing the threshold necessary for stall. This implies that the compressor may have entered a rotating stall operating condition. This fact is verified by Figure 6.11 which shows the operating point migrating from the 80 % prestall corrected speed characteristic to the 80 % post-stall corrected speed characteristic.

Figure 6.15 is a plot of individual stage pressure rise and inlet temperature versus time for stages one and two of the compressor during the inlet temperature transient. This plot clearly shows that both stages are initially unstalled. During the inlet temperature transient, it can be seen that individual stage pressure rise begins to decrease for both stages as the compressor inlet temperature increases. As the inlet temperature begins to decay back to the ambient temperature, individual stage pressure rise begins to increase for both stages. Upon return of the inlet temperature back to the ambient temperature, it can be seen that individual stage pressure rise for both stages is lower than before the temperature transient was applied across the compressor inlet. Rotating stall signatures have appeared and are clearly identified for both stages indicating that both stages are now operating in rotating stall.

The results of Figures 6.11, 6.14, and 6.15 support the energized compression system dynamic response rotating stall hypothesis. They clearly demonstrate that energizing a compression system with an inlet temperature excursion can induce a dynamic response that drives the operating point across the stall line. They also show that the crossing of the stall line by the operating point, during the energized dynamic response, implies that the rotor blade flow angle of attack has been sufficiently increased to induce stall.

6.4 No Rotating Stall

A fourth experiment was conducted with the compressor initially operating on the 80 % prestall corrected speed characteristic, as in the third experiment. The fourth experiment demonstrated that if the operating point did not cross the stall line during an energized compression system dynamic response, the compressor did not enter rotating stall. Figure 6.16 identifies the compressor performance map for the overall compressor. The performance map shows the transient path taken by the operating point during the transient inlet temperature excursion of the fourth experiment. The inlet temperature transient applied can be seen in Figures 6.17, 6.18, 6.19, and 6.20. The compressor was initially operating on the 80 % prestall corrected speed characteristic at point (A), when energy was added to the compression system in the form of another low level inlet temperature transient. The dynamic response of the compression system moved the

Metric Conversions

$$\frac{\text{kg}}{\text{s}} = \frac{\text{lbm}}{\text{sec}} (0.45359237)$$

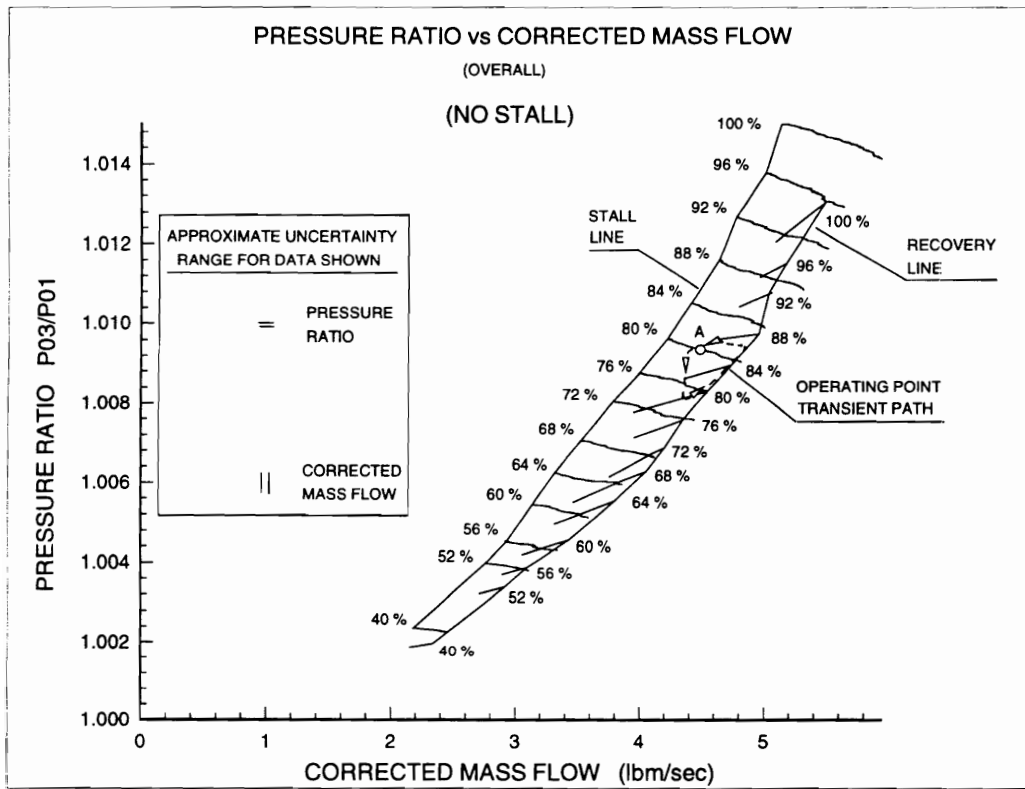


Figure 6.16 Compressor Performance Map (Overall)
(No Stall)

Metric Conversions

$$K = 273.0 + \frac{5}{9}[R - 492.0]$$

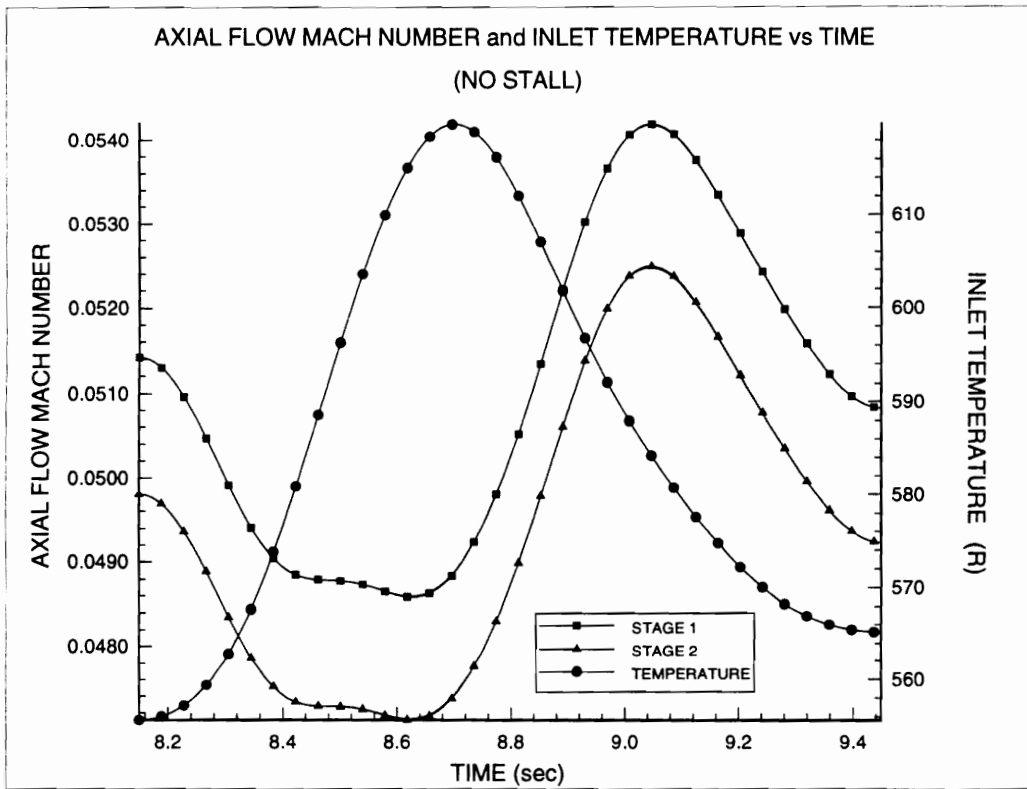


Figure 6.17 Axial Flow Mach Number and Inlet Temperature vs Time (No Stall)

Metric Conversions

$$K = 273.0 + \frac{5}{9}[R - 492.0]$$

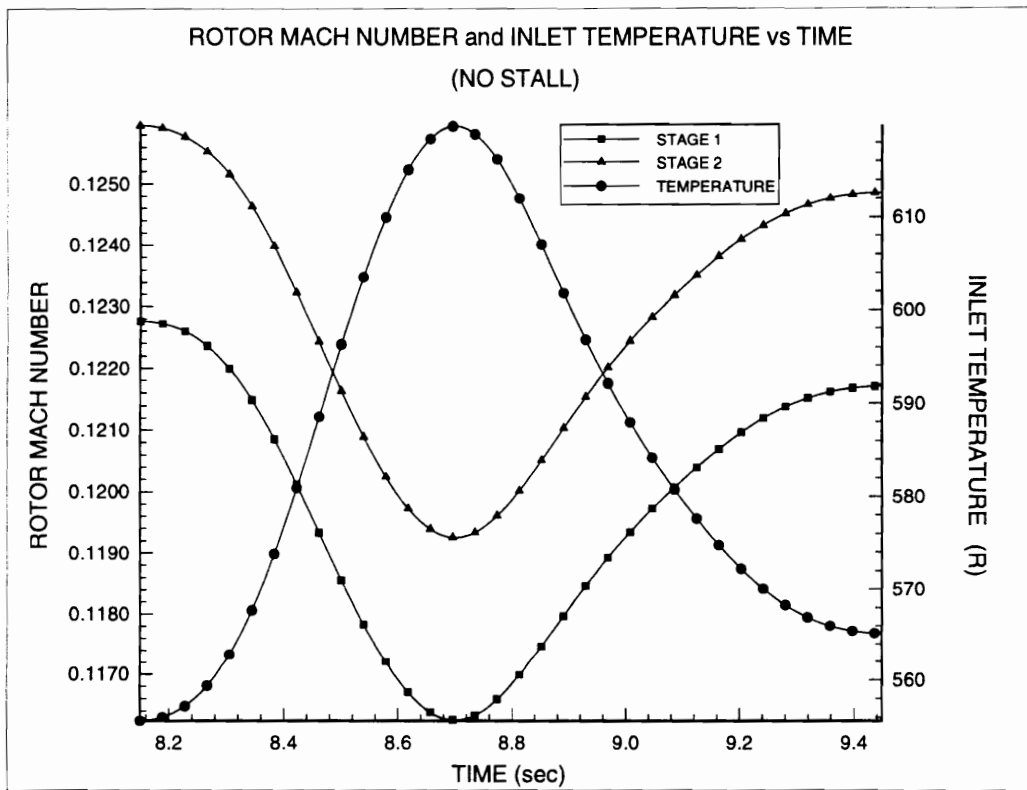


Figure 6.18 Rotor Mach Number and Inlet Temperature vs Time (No Stall)

Metric Conversions

$$K = 273.0 + \frac{5}{9}[R - 492.0]$$

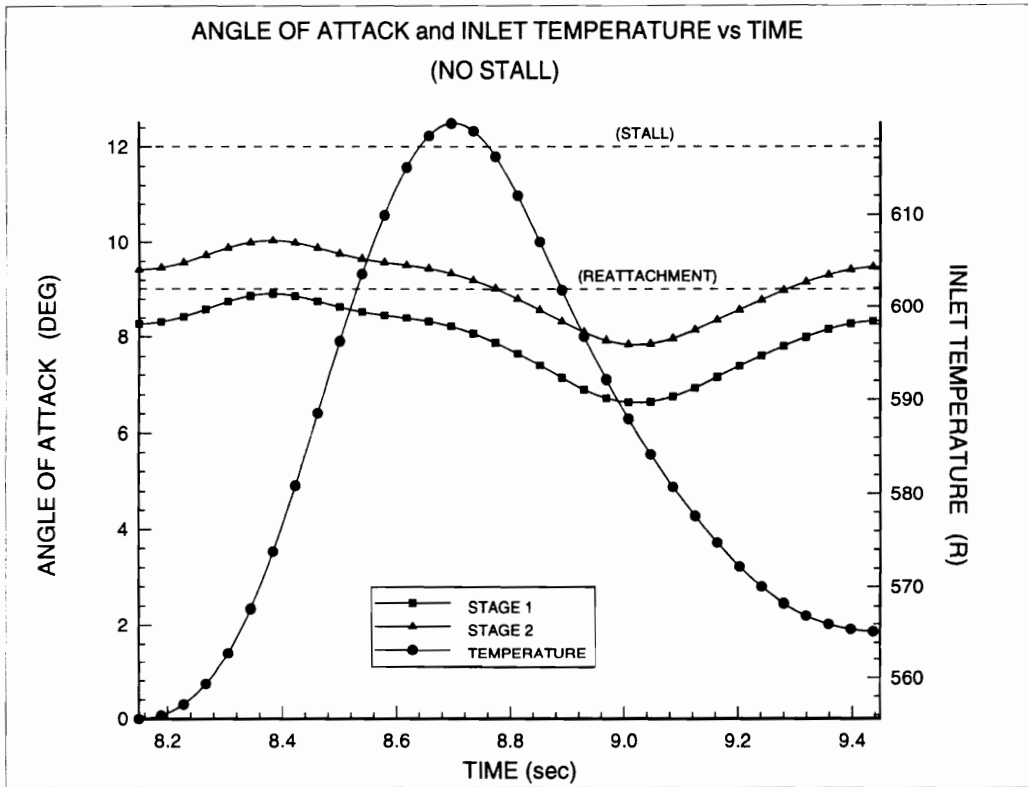


Figure 6.19 Blade Angle of Attack and Inlet Temperature vs Time (No Stall)

Metric Conversions

$$K = 273.0 + \frac{5}{9}[R - 492.0]$$

$$\frac{N}{m} = \frac{lbf}{ft} (47.87488)$$

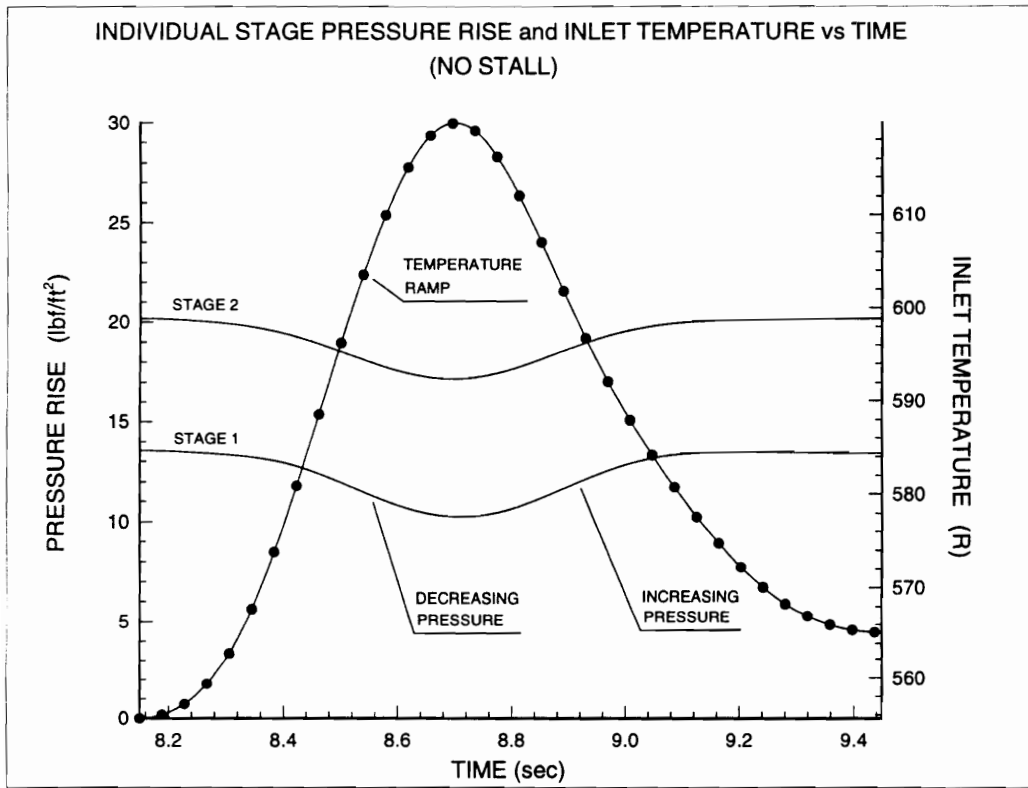


Figure 6.20 Individual Stage Pressure Rise and Inlet Temperature vs Time (No Stall)

operating point down, and back to point (A) after the inlet temperature decayed back to the ambient temperature.

In this situation, the inlet temperature transient was not sufficient in magnitude to add enough energy to the compression system to energize a dynamic response from the compression system that would drive the operating point beyond the stall line. This is shown by the path of the process in Figure 6.16. The failure of the operating point to reach the stall line during the compression system dynamic response, implies that the rotor blade incidence and rotor blade angle of attack were not increased sufficiently during the inlet temperature transient to cause stall by definition of the stall line.

Figure 6.17 shows the calculated axial flow Mach number and inlet temperature versus time for stages one and two at the compressor mean radius. Figure 6.18 shows the calculated rotor Mach number and inlet temperature versus time for stages one and two at the compressor mean radius. Figures 6.17 and 6.18 reveal relatively small changes in axial flow and rotor Mach numbers at the compressor mean radius. Therefore, there was not a significant transient change in the rotor blade Mach number triangle for this process.

Figure 6.19 is a plot of calculated rotor blade angle of attack and inlet temperature versus time for stages one and two at the compressor mean radius. This plot clearly demonstrates that the rotor blade angle of attack increased for both stages at the compressor mean radius during the temperature excursion. However, the rotor blade angle of attack did not cross the threshold necessary for the stall. This implies that the compressor may not have entered a rotating stall operating condition. This fact is verified

by Figure 6.16, which identifies the operating point returning to the initial operating point position on the 80 % prestall corrected speed characteristic.

Figure 6.20 is a plot of individual stage pressure rise and inlet temperature versus time for stages one and two of the compressor during the inlet temperature transient. This plot clearly shows that both stages are initially unstalled. During the inlet temperature transient, it can be seen that individual stage pressure rise begins to decrease for both stages as the compressor inlet temperature increases. As the inlet temperature begins to decay back to the ambient temperature, individual stage pressure rise begins to increase for both stages. Upon return of the inlet temperature back to the ambient temperature, it can be seen that individual stage pressure rise for both stages returned to the levels of stage pressure rise that were being produced before the temperature transient was applied across the compressor inlet. Rotating stall signatures are not evident on any of the compressor stages, indicating that neither stage stalled nor entered a rotating stall operating condition.

The results of Figures 6.16, 6.19, and 6.20, for the fourth experiment, also provide support for the energized compression system dynamic response rotating stall hypothesis. They clearly demonstrate that if the energized compression system dynamic response does not drive the operating point across the stall line, the compressor does not stall. The interpretation of this result is that if the compression system operating point does not cross the stall line, the rotor blade flow angle of attack will not have been sufficiently increased to cause the compression system to stall.

6.5 Rotating Stall Followed By An Immediate Recovery

The fifth and final experiment conducted was an induced compressor rotating stall followed by an immediate recovery by an inlet temperature transient. Figure 6.21 identifies the compressor performance map for the overall compressor. The performance map shows the transient path taken by the operating point during the transient inlet temperature excursion. The inlet temperature transient applied can be seen in Figures 6.22, 6.23, 6.24, and 6.25. The compressor was initially operating on the 80 % prestall corrected speed characteristic at point (A) when energy was added to the compression system in the form of an inlet temperature transient. The dynamic response of the compression system drove the operating point across the stall line towards point (B) inducing stall. However, the inlet temperature transient applied across the compressor inlet in this situation was sufficient in magnitude to continue adding energy to the compression system after the compressor stalled. This additional energy drove the operating point towards lower values of corrected mass flow and corrected speed, to point (C), as the inlet temperature continued to increase. Then, the dynamic response of the energized compression system drove the operating point across the recovery line to point (D), and induced an immediate recovery from the stalled operating condition. As the inlet temperature decayed back to the ambient temperature, the operating point returned back to 80 % prestall corrected speed characteristic at point (A), and the compression system was operating unstalled.

Metric Conversions

$$\frac{\text{kg}}{\text{s}} = \frac{\text{lbm}}{\text{sec}} (0.45359237)$$

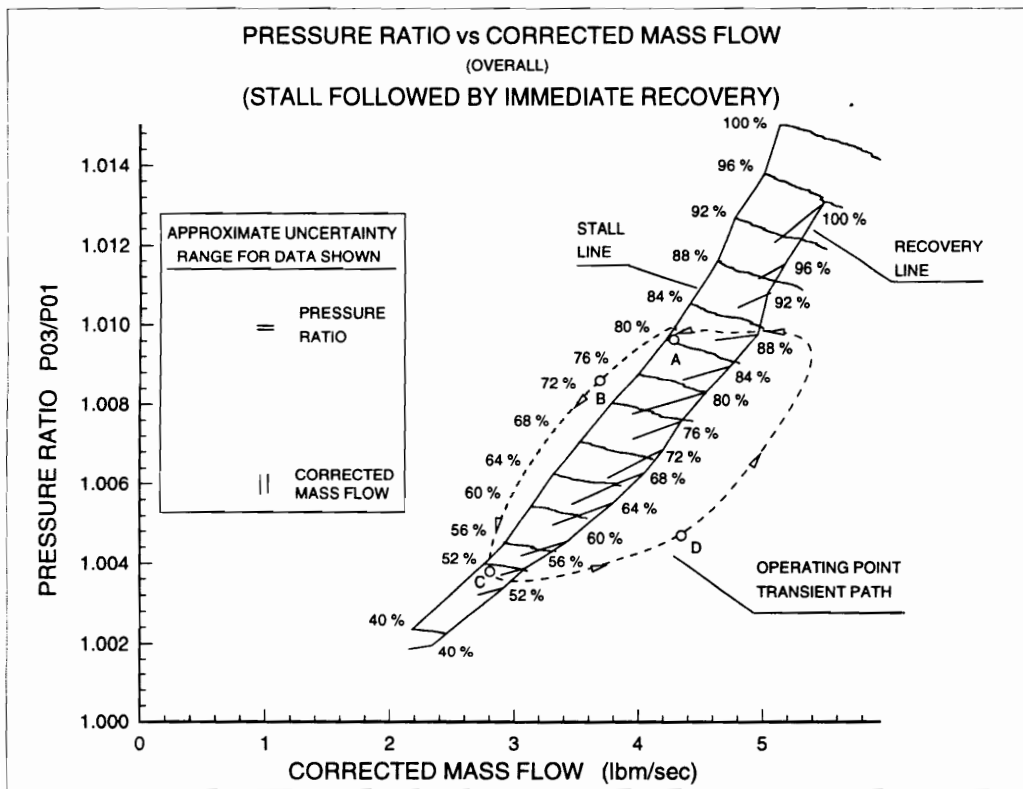


Figure 6.21 Compressor Performance Map (Overall)
(Stall Followed By Immediate Recovery)

Metric Conversions

$$K = 273.0 + \frac{5}{9}[R - 492.0]$$

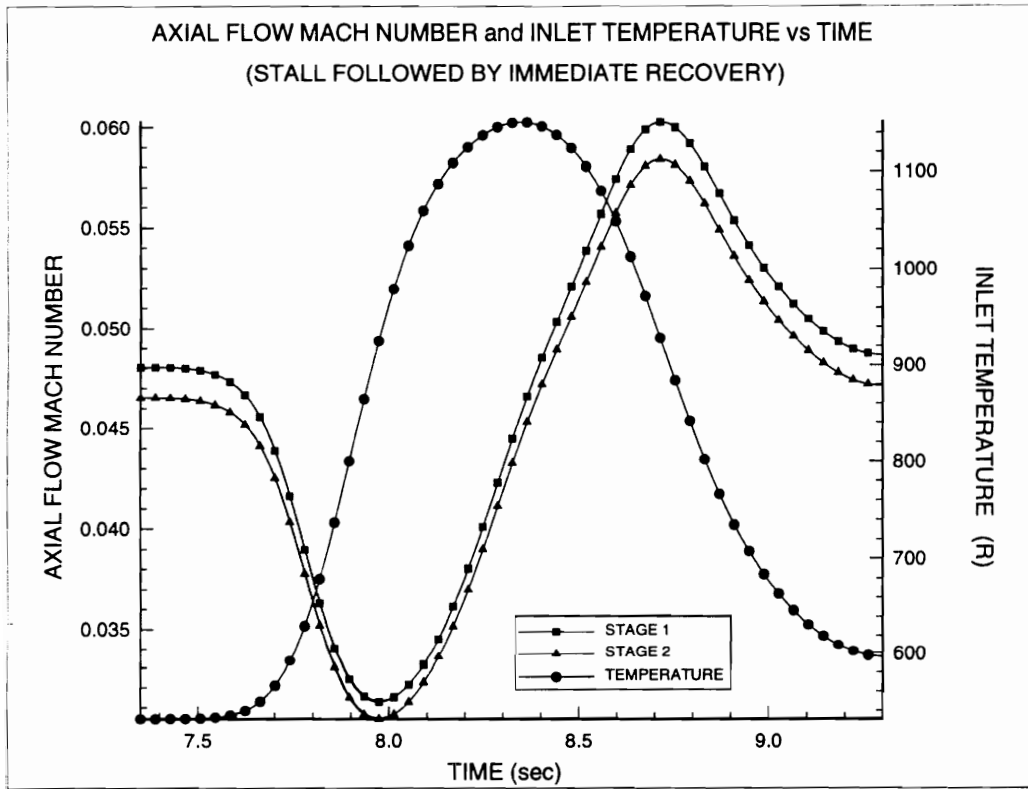


Figure 6.22 Axial Flow Mach Number and Inlet Temperature vs Time (Stall Followed By Immediate Recovery)

Metric Conversions

$$K = 273.0 + \frac{5}{9} [R - 492.0]$$

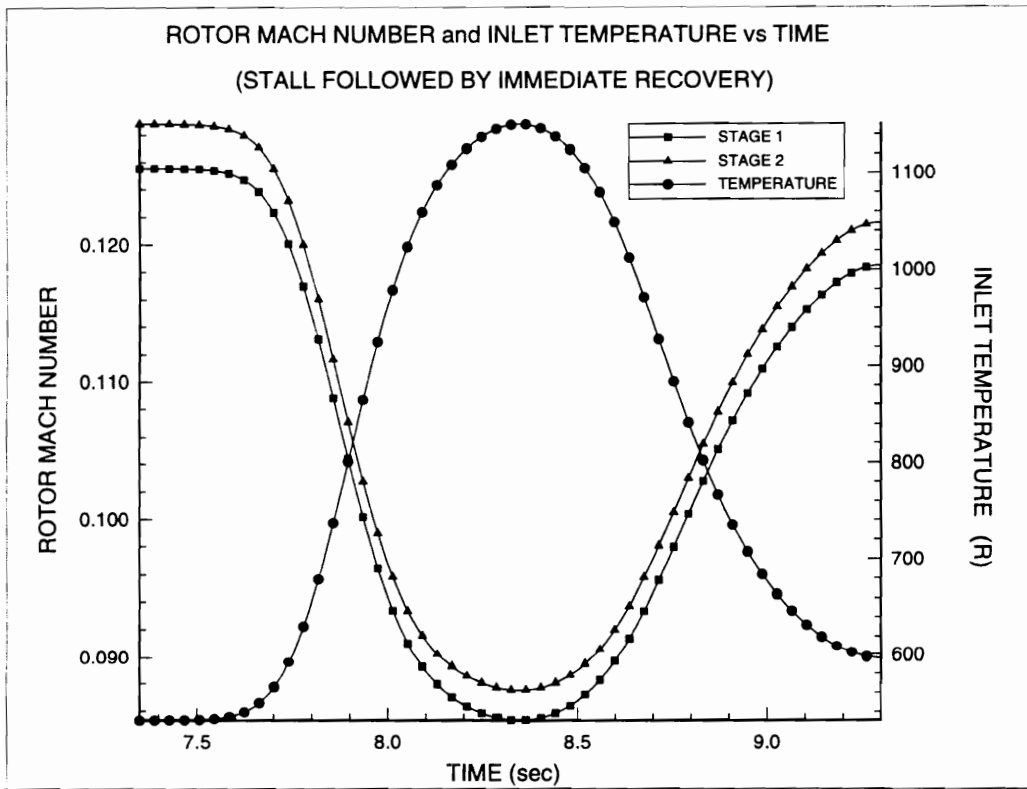


Figure 6.23 Rotor Mach Number and Inlet Temperature vs Time (Stall Followed By Immediate Recovery)

Metric Conversions

$$K = 273.0 + \frac{5}{9}[R - 492.0]$$

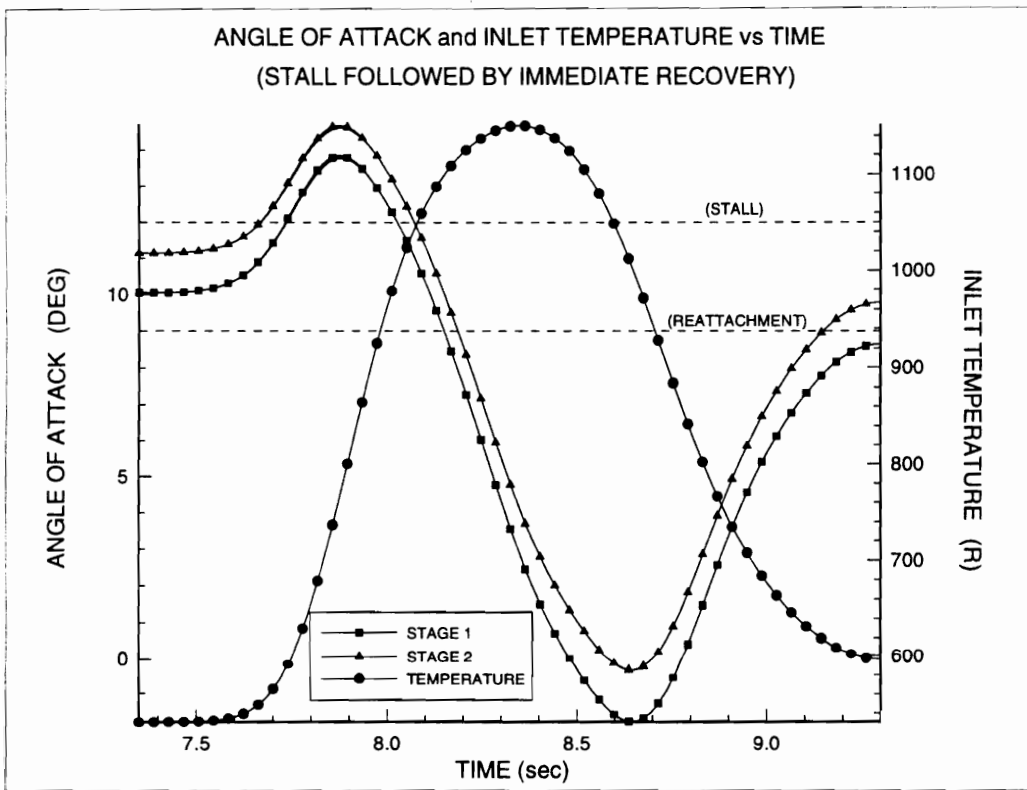


Figure 6.24 Blade Angle of Attack and Inlet Temperature vs Time (Stall Followed By Immediate Recovery)

Metric Conversions

$$K = 273.0 + \frac{5}{9}[R - 492.0]$$

$$\frac{N}{m} = \frac{lbf}{ft} (47.87488)$$

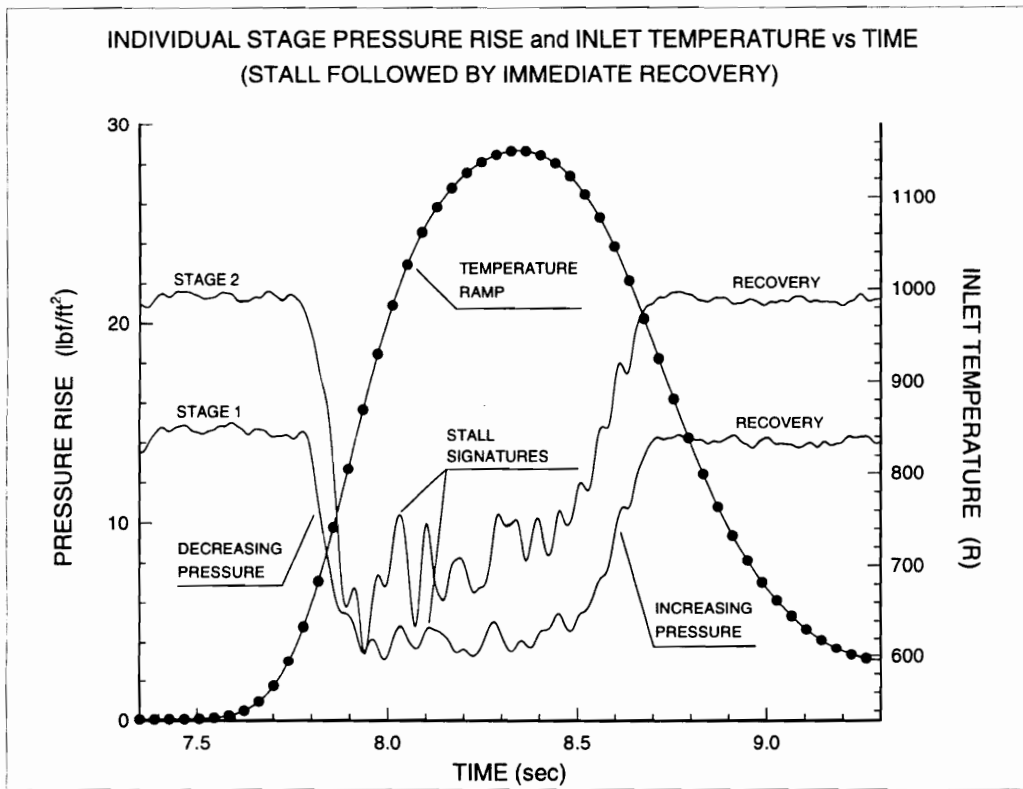


Figure 6.25 Individual Stage Pressure Rise and Inlet Temperature vs Time (Stall Followed By Immediate Recovery)

During the beginning of the inlet temperature transient, it was observed that corrected mass flow rate and corrected speed decreased as the inlet temperature increased, driving the operating point across the stall line. This is shown by the path of the process in Figure 6.21. This implies that the axial flow and rotor Mach numbers also decreased as the inlet temperature increased. This fact was verified by the experimental data plots of Figures 6.22 and 6.23. Figure 6.22 is a plot of calculated axial flow Mach number and inlet temperature versus time for stages one and two at the compressor mean radius. These results demonstrate that axial flow Mach number decreased for both stages at the compressor mean radius as inlet temperature increases. Figure 6.23 is a plot of calculated rotor Mach number and inlet temperature versus time for stages one and two at the compressor mean radius. It clearly demonstrates that rotor Mach number decreased for both stages at the compressor mean radius as inlet temperature increased. It is observed from Figure 6.22 and Figure 6.23 that axial flow Mach number decreased sooner, and at a faster rate than rotor Mach number at the compressor mean radius. This implies that the rotor blade Mach number triangle changed, causing a transient increase in rotor blade incidence and rotor blade angle of attack. When the operating point reached the stall line, the rotor blade incidence and rotor blade angle of attack had been increased sufficiently to cause the flow to separate from the rotor blade surface and stall by definition of the stall line.

As energy was continually added to the compression system during the inlet temperature transient, corrected mass flow and corrected speed continued to decrease as

the inlet temperature increased, moving the operating point towards point (C) as shown by the path of the process in Figure 6.21. As the operating point began to move towards the recovery line to point (D), it was observed that corrected mass flow rate began to increase. This implies that axial flow Mach number also began to increase as shown by the data taken at the compressor mean radius in Figure 6.22. Figures 6.22 and 6.23 reveal that during this part of the compression system transient response, there was a significant change in the rotor blade Mach number triangle because axial flow Mach number increased sooner, and at a faster rate than rotor Mach number at the compressor mean radius. This caused a transient decrease in rotor blade incidence and rotor angle of attack. When the operating point reached the recovery line, the rotor blade incidence and rotor blade angle of attack had been reduced sufficiently to cause the stalled flow to reattach to the rotor blade surface by definition of the recovery line.

Figure 6.24 is a plot of calculated rotor blade angle of attack and inlet temperature versus time for stages one and two at the compressor mean radius. This plot clearly demonstrates that the rotor blade angle of attack initially increased for both stages at the compressor mean radius during the temperature excursion, crossing the threshold necessary for stall. This suggests that the compressor may have stalled, and this fact is verified by Figure 6.21 which identifies the operating point crossing the stall line. As energy was continually added to the compression system, the rotor blade angle of attack decreased at the compressor mean radius, crossing the threshold necessary for stalled flow reattachment. This suggests that the compressor may have recovered from the rotating stall operating condition. This fact is verified by Figure 6.21 which identifies the

operating point crossing the recovery line and returning to the initial operating point position on the 80 % prestall corrected speed characteristic.

Figure 6.25 is a plot of individual stage pressure rise and inlet temperature versus time for stages one and two of the compressor during the inlet temperature transient. This plot clearly shows that both stages are initially unstalled. During the inlet temperature transient, it can be seen that individual stage pressure rise begins to decrease for both stages as the compressor inlet temperature increases. Stall signatures begin to appear for both stages indicating that both stages are beginning to stall. As the inlet temperature continues to increase and then begins to decay back to the ambient temperature, individual stage pressure rise begins to increase for both stages. Upon return of the inlet temperature back to the ambient temperature, it can be seen that individual stage pressure rise for both stages has returned to the initial levels of stage pressure rise as before the temperature transient was applied across the compressor inlet. Rotating stall signatures are not evident on either of the compressor stages, indicating that neither stage entered a rotating stall operating condition.

7. CONCLUSIONS AND SUMMARY

7.1 Conclusions

The effects of inlet temperature transients on the stall and stall recovery aerodynamics of a low speed multi-stage axial flow compressor have been experimentally investigated and presented. A review of the literature revealed that the stall process during an inlet temperature transient was previously understood only through the use of a compressor map. Details of the rotor blade flow physics associated with the stall process during an inlet temperature transient, had never been developed nor addressed. No literature was found describing how an inlet temperature transient could energize and make a compression system recover from a rotating stall operating condition.

It was determined that the addition of energy to a compression system in the form of transient inlet temperature excursions can energize a dynamic response from a compression system. The compression system was modeled as a classical Helmholtz resonator and the dynamics of the compression system, subjected to different inlet temperature transients, were determined. It was found that high magnitude inlet temperature transients caused large compression system dynamic responses, inducing large changes in compressor pressure ratio and corrected mass flow. Small magnitude inlet temperature transients caused small compression system dynamic responses, inducing small changes in compressor pressure ratio and corrected mass flow.

Two theoretical hypotheses, regarding the rotor blade flow physics associated with the stall and rotating stall recovery processes of a compression system energized by an inlet temperature transient, were developed and experimentally tested. The blade flow associated with these two hypotheses, was found to be governed by a single fundamental equation for rotor blade incidence, that was modified to be a function of Mach numbers. This equation related the rotor blade incidence at a particular rotor blade radius, to the rotor and axial flow Mach numbers at that same rotor blade radius. This equation is valid along the entire span of the rotor blade. To evaluate this equation required knowledge of the rotor and axial flow Mach numbers, at a particular rotor blade radius, as functions of time during the inlet temperature transient. This information was obtained experimentally at the compressor mean radius during this portion of research as previously demonstrated and discussed.

One hypothesis postulated the rotor blade flow behavior of the compression system stall process during an inlet temperature transient, with reference to the stall line. The second hypothesis postulated the rotor blade flow behavior of the compression system rotating stall recovery process during an inlet temperature transient. The second hypothesis introduced a new concept on the compression system performance map called the recovery line. The rotor blade flow behavior of the rotating stall recovery process during an inlet temperature transient, was postulated with reference to the recovery line.

Five experiments were conducted on a low speed two-stage axial-flow compressor to demonstrate the effects of inlet temperature transients on compression

system dynamic response and to test the two theoretical hypotheses. The following conclusions were drawn from the theory and the experiments.

7.1.1 Rotating Stall Recovery Conclusions

- A compression system operating in rotating stall can be energized by an inlet temperature transient and made to recover from the rotating stall operating condition. This is believed to be a new technique for active recovery from rotating stall.
- The energized dynamic response of the compression system operating in rotating stall causes a transient decrease in rotor blade incidence and rotor blade angle of attack.
- The transient decrease in rotor blade incidence during an inlet temperature transient is governed by the modified fundamental equation for rotor blade incidence as a function of Mach numbers.
- A new line called the “recovery line” has been defined and introduced on the compressor performance map.
- The recovery line has a physical interpretation. It represents the boundary on the performance map where stalled flow will reattach to the rotor blade surface if the operating point reaches or drifts beyond it. If the operating point does not reach or cross the recovery line, the compression system does not recover from the rotating stall operating condition.

7.1.2 Conclusions Related To The Development Of Stall

- A compression system energized by an inlet temperature transient will stall if the compression system dynamic response drives the operating point to or across the stall line.
- The energized dynamic response of the compression system causes a transient increase in rotor blade incidence and rotor blade angle of attack.
- The transient increase in rotor blade incidence during an inlet temperature transient is governed by the modified fundamental equation for rotor blade incidence as a function of Mach numbers.
- The stall line has a physical interpretation. It represents the boundary on the performance map where rotor blade incidence and rotor blade angle of attack will have been increased sufficiently to cause stall if the operating point reaches or drifts beyond it. If the operating point does not reach or drift beyond the stall line the compression system does not stall.

The results from the experiments demonstrate the effects of inlet temperature transients on compression system dynamic response. The experimental results also demonstrate and support the rotor blade flow physics and concepts postulated in the two hypotheses.

7.2 Summary

The compression system dynamic response to different magnitudes of inlet temperature transients applied across the compressor inlet induced different transient variations in compressor rotor blade incidence and rotor blade angle of attack. The compression system traversed stalled and unstalled operational states on the quasi-steady compressor performance map while in dynamic transit to a new operating condition. Depending upon the initial operating condition of the compression system, the dynamic response of the compression system to the inlet temperature transients either induced compressor rotating stall or rotating stall recovery. The concepts and physics have been experimentally demonstrated and supported.

8. RECOMMENDATIONS AND FUTURE WORK

The scope of this dissertation was to explain how an axial flow compression system could stall or recover from rotating stall operation by applying an inlet temperature transient. The focus was on the rotor blade flow physics. It was determined that a single fundamental equation modified to be a function of Mach numbers governed the rotor blade flow physics associated with both the stall and rotating stall recovery processes. The equation related the rotor blade incidence at a particular rotor blade radius, to the rotor and axial flow Mach numbers at that same rotor blade radius. This equation is valid along the entire span of the rotor blade. To evaluate this equation required knowledge of the rotor and axial flow Mach numbers, at a particular rotor blade radius, as functions of time during the inlet temperature transient. This information was obtained **experimentally** at the compressor mean radius during this portion of research as previously demonstrated and discussed.

In the future, it should be possible to simulate the observed behavior with a dynamic compression system model. This would require developing a dynamic compression system model that accurately simulated the dynamic response of a compression system during an inlet temperature transient. The **calculated** values of rotor and axial flow Mach numbers produced by the simulation, could then be used to calculate the rotor blade incidence by applying the equation for rotor blade incidence as applied in this piece of research.

Calculating rotor blade incidence with the values of Mach numbers calculated within the dynamic simulation along with the concept of the recovery line, can be included in existing compression system dynamic simulation models. This would add the capability to existing simulations to determine if a compression system, initially operating in rotating stall, would recover from the rotating stall operating condition by energizing the compression system with an inlet temperature transient.

When three-dimensional dynamic compression system models are developed, the axial flow Mach number profile along the entire span of the rotor blade can be calculated. Equation (3.2) can then be applied at each rotor blade radius to calculate rotor blade incidence and rotor blade angle of attack, using the rotor and axial flow Mach number profiles along the entire span of the rotor blade.

It was determined in this research that the addition of energy to the compression system in the form of transient inlet temperature excursions would energize a dynamic response from the compression system. The compression system dynamic response was a function of the magnitude of the inlet temperature transient applied. Additional research must be conducted to fully understand the dynamic response of a compression system when subjected to inlet temperature transients. Specifically, the relationship between compressor pressure ratio and corrected mass flow rate as functions of inlet temperature and inlet temperature ramp rate should be determined.

The next logical step in this investigation should be to perform a rotating stall recovery test with an inlet temperature transient, on a high speed multi-stage compressor.

This type of test will hopefully support the results obtained in this piece of research for a low-speed compressor. Upon completion of the high speed compressor rotating stall recovery test, additional compressor rig experiments should be conducted.

It is clear that the compressor working fluid density plays an important role in the dynamic response of the compression system in addition to the working fluid temperature. Although inlet flow density variations were not specifically addressed in this particular investigation they were inherently introduced into the experiment as the inlet temperature changed. Experiments should be conducted in the future that address inlet flow density variations specifically without temperature changes. It is believed that using a gas with a density lower than air, such as helium, will produce similar effects found in this investigation. These types of experiments will have important implications if the ideas and concepts developed in this piece of research are to be applied in the development of a practical rotating stall recovery system.

Compressor stall and rotating stall recovery experiments should be conducted using a gas with a density lower than air, such as helium. A compressor should be initially in steady unstalled operation compressing air. At some point in the experiment, a gas with density lower than air such as helium, should be injected into the compressor inlet. Proper instrumentation should be installed to measure compressor pressure rise, axial flow velocity, axial flow Mach number, and rotor Mach number on a stage by stage basis. Trends to look for in this type of experiment are a rapid decrease in compressor pressure

rise, axial flow velocity, and axial flow Mach number on a stage by stage basis just prior to stall.

Similarly, the same compressor should be initially operating in rotating stall while ingesting air. Helium should then be injected into the compressor inlet to determine if the compression system will undergo a dynamic response and recover from the rotating stall operating condition. Measurements should be taken to observe compressor pressure rise, axial flow velocity, axial flow Mach number, and rotor Mach number on a stage by stage basis. Trends to look for in this type of experiment are an increase in axial flow velocity, and axial flow Mach number on a stage by stage basis just prior to rotating stall recovery. These results will support the concept of using a gas with a density lower than air such as helium, to induce compressor rotating stall recovery.

A set of compressor experiments should be conducted to examine the effects of partial admission of the high temperature gas on the stall recovery process. These experiments should be conducted with both inlet temperature transients and low density gas. These particular experiments will also have important implications for the development of a practical rotating stall recovery system. The relationship between inlet circumferential extent and magnitude of the temperature transient or gas density required for compressor rotating stall recovery to be effective, should be determined.

The results of the compressor rig experiments should then be used to develop and validate more predictive analytical theories relating to compression system dynamic response.

9. REFERENCES

Cited References

1. Wells, H.S., "A Study Of Rocket Exhaust Gas Ingestion Simulation Techniques For The AEDC", ARO ENGR RPT 77-3, March 1977.
2. Childs, J.H., Kochendorfer, F.D., Lubick, R.J., and Friedman, R., "Stall And Flame-Out Resulting From Firing Of Armament", NACA RM E55E25, 1955.
3. Braithwaite, W.M., Garber Jr., E.J., and Mehalic, C.M., "The Effect Of Inlet Temperature And Pressure Distortion On Turbojet Performance", AIAA Paper No. 73-1316, 1973.
4. Society of Automotive Engineers, "A Current Assessment Of The Inlet/Engine Temperature Distortion Problem", Aerospace Resource Document ARD50015, 1991-01-22.
5. Wallner, Lewis E., Useller, James W., and Saari, Martin J., "A Study Of Temperature Transients AT The Inlet Of A Turbojet Engine" NACA RM E57C22, June 1957.
6. Mehalic, Charles M., Lottig, Roy A., "Steady State Inlet Temperature Distortion Effects On The Stall Limits Of A J-85-GE-13 Turbojet Engine", NASA TM X-2990, February 1974.
7. Rudey, Richard A. and Antl, Robert J. "The Effects Of Inlet Temperature Distortion On The Performance Of A Turbofan Engine Compressor System", NASA TM X-52788, June 1970.
8. Abdelwahab, Mahmood, "Effects of Temperature Transients at Fan Inlet of a Turbofan Engine", NASA TP 1031, September 1977.
9. Davis Jr., M.W., "Evaluation Of A-10 Flight Test Data To Determine The Causes Of Engine Instability Problems While Ingesting Gun Exhaust Gas", AEDC-TMR-79-G11, August 1979.
10. Egolf, D.P. "Mathematical Modeling of A Probe-Tube Microphone", JASA, VOL. 61, NO.1, January 1977, pp 200-205.
11. Kinsler, L.E., Coppens, A.B., Frey, A.R., and Sanders J.V., "Fundamentals Of Acoustics", Third Edition, John Wiley & Sons 1982, pp 225-226.

REFERENCES **(Continued)**

12. Yocum, A.M., "An Experimental and Numerical Investigation of the Performance of Compressor Cascades with Stalled Flow", Doctorate Dissertation, Virginia Polytechnic Institute and State University, Blacksburg, VA, May 1988, pp 275-285.
13. DiPietro Jr. A.L., "Design And Experimental Evaluation Of A Dynamic Thermal Distortion Generator For Turbomachinery Research", Masters Thesis, Virginia Polytechnic Institute and State University, Blacksburg, VA, April 1993.
14. DiPietro Jr., A.L., O' Brien, W.F., "Design And Experimental Evaluation Of A Dynamic Thermal Distortion Generator For Turbomachinery Research", AIAA 94-0149, Virginia Polytechnic Institute and State University, Blacksburg, VA, January 1994.
15. DiPietro Jr., A.L., O' Brien, W.F., "Stall and Recovery Aerodynamics of A Low Speed Multi-Stage Compressor With Inlet Temperature Transients", AIAA 97-0163, Virginia Polytechnic Institute and State University, Blacksburg, VA, January 1997.
16. DiPietro Jr., A.L., O' Brien, W.F., "A New Technique For Active Recovery From Rotating Stall", AIAA 97-0164, Virginia Polytechnic Institute and State University, Blacksburg, VA, January 1997.
17. Abbott, Ira H. and Von Doenhoff, Albert E., "Theory Of Wing Sections", Second Edition, Dover Publications, Inc., New York 1959.
18. Day, I.J., "Active Suppression of Rotating Stall and Surge in Axial Compressors", ASME 91-GT-87, June 1991.

Uncited References

19. Abdelwahab Mahmood,"Effects of Fan Inlet Temperature Disturbances on the Stability of a Turbofan Engine", NASA-TM 82699, December 1981.
20. Dowler, C., Boyer, K., and Poti N., "Model Predictions of Fan Response to Inlet Temperature Transients and Spatial Temperature Distortion", AIAA 89-2686, July 1989.
21. Das, D.K. and Trippi, A., "Unsteady Response Of An Axial Flow Compressor To Planar Temperature Transients", AIAA 82-1266, June 1982.
22. Walter, W.A. and Shaw, M., "Predicted F100 Engine Response To Circumferential Pressure And temperature Distortion", 1979.

REFERENCES

(Continued)

23. Garber Jr., E.J. and Braithwaite, W.M., "Summary Of Recent Investigations Of Inlet Flow Distortion Effects On Engine Stability", AIAA 74-236, February 1974.
24. Reid, C., "The Response of Axial Flow Compressor to Intake Flow Distortion", ASME 69-GT-29, 1970.
25. Glawe, G.E., Holanda, R., and Krause, L.N., "Recovery and Radiation Corrections and Time Constants of Several Sizes of Shielded and Unshielded Thermocouple Probes for Measuring Gas Temperature", NASA-TP-1099, January 1978.
26. Taback, I., "The Response Of Pressure Measuring Systems To Oscillating Pressure", NACA-TN 1819, February 1949.
27. Greitzer, E.M., "Surge and Rotating Stall in Axial Flow Compressors Part I: Theoretical Compression System Model", ASME 75-GT-9, 1976.
28. Greitzer, E.M., "Surge and Rotating Stall in Axial Flow Compressors Part II: Experimental Results and Comparison With Theory, ASME 75-GT-10, 1976.
29. Jinan, Xie and Xiaoxu, Bai, "An Investigation of Rotating Stall and Surge of a 10-Stage Subsonic Compressor", ASME 85-1GT-96, 1985.
30. Melick Jr., H.C. and Simpkin, W.E., "A Unified Theory Of inlet/Engine Compatibility", AIAA 72-1115, December 1972.
31. Marchman III, J.F., Sumantran, V., and Schaefer, C.G., "Acoustic and Turbulence Influences on Stall Hysteresis", AIAA 86-0170, January 1986.
32. Oates, G.C., "Aerothermodynamics of Gas Turbine and Rocket Propulsion", AIAA Educational Series, Published by American Institute of Aeronautics and Astronautics, Inc., 1988, pp.19-62.
33. Zukoski, Edward E., and Marble, F.E., "Experiments Concerning The Mechanism of Flame Blowoff from Bluff Bodies," Proceedings of the Gas Dynamics Symposium on Aerothermochemistry, Northwestern University Press, Evanston, Ill., 1955.
34. Cohen, H., Rogers, G.F.C., Saravanamuttoo, H.I.H., "Gas Turbine Theory", Third Edition, John Wiley & Sons, Inc., New York, 1978.

REFERENCES **(Continued)**

35. Hill, P.G., Peterson, C.R., "Mechanics And Thermodynamics Of Propulsion", Addison Wesley Publishing Company, Inc., 1965.
36. Kuo, K.K., "Principles Of Combustion", John Wiley & Sons, Inc., 1986.
37. Seddon, J. and Goldsmith, E.L., " Intake Aerodynamics", AIAA Educational Series, Published by American Institute of Aeronautics and Astronautics, Inc 1985.
38. Oates, G.C., " Aerothermodynamics of Aircraft Engine Components", AIAA Educational Series, Published by American Institute of Aeronautics and Astronautics, Inc., 1985.
39. Van Wylen, G.J., Sonntag, R.E., " Fundamentals Of Classical Thermodynamics", Third Edition, John Wiley & Sons, Inc., New York, 1986.
40. Schetz, J.A., "Foundations of Boundary Layer Theory For Momentum, Heat, and Mass Transfer", Prentice Hall, Inc., New Jersey, 1984.
41. Anderson, J.D., " Modern Compressible Flow With Historic Perspective", second edition, McGraw Hill Publishing Company, 1982.
42. Bertin, J.J., Smith, M.L., " Aerodynamics For Engineers", second edition, Prentice Hall, Inc., New Jersey, 1979.
43. Vincenti, W.G., Kruger Jr. C.H., " Introduction To Physical Gas Dynamics", Robert E. Krieger Publishing Co., Inc., Florida, 1986.

10. APPENDIX A

Experimental Data

This appendix contains additional plots which were generated from measured or calculated data for five experiments. These plots were not presented as part of the chapter 6 discussion but are included here as additional information. The following data is presented for the five experiments :

- 1) Pressure Ratio vs Time vs Inlet Temperature
- 2) Corrected Mass Flow vs Time vs Inlet Temperature
- 3) Flow Density vs Time vs Inlet Temperature
- 4) Axial Flow Velocity vs Time vs Inlet Temperature
- 5) Blade Incidence vs Time vs Inlet Temperature
- 6) Throttle Area vs Time vs Inlet Temperature

10.1 Additional Plots For Experiment 1, (Rotating Stall Recovery)

The following additional data plots are presented for experiment 1, the compressor **rotating stall recovery** experiment :

- 1) Pressure Ratio vs Time vs Inlet Temperature
- 2) Corrected Mass Flow vs Time vs Inlet Temperature
- 3) Flow Density vs Time vs Inlet Temperature
- 4) Axial Flow Velocity vs Time vs Inlet Temperature
- 5) Blade Incidence vs Time vs Inlet Temperature
- 6) Throttle Area vs Time vs Inlet Temperature

Metric Conversions

$$K = 273.0 + \frac{5}{9} [R - 492.0]$$

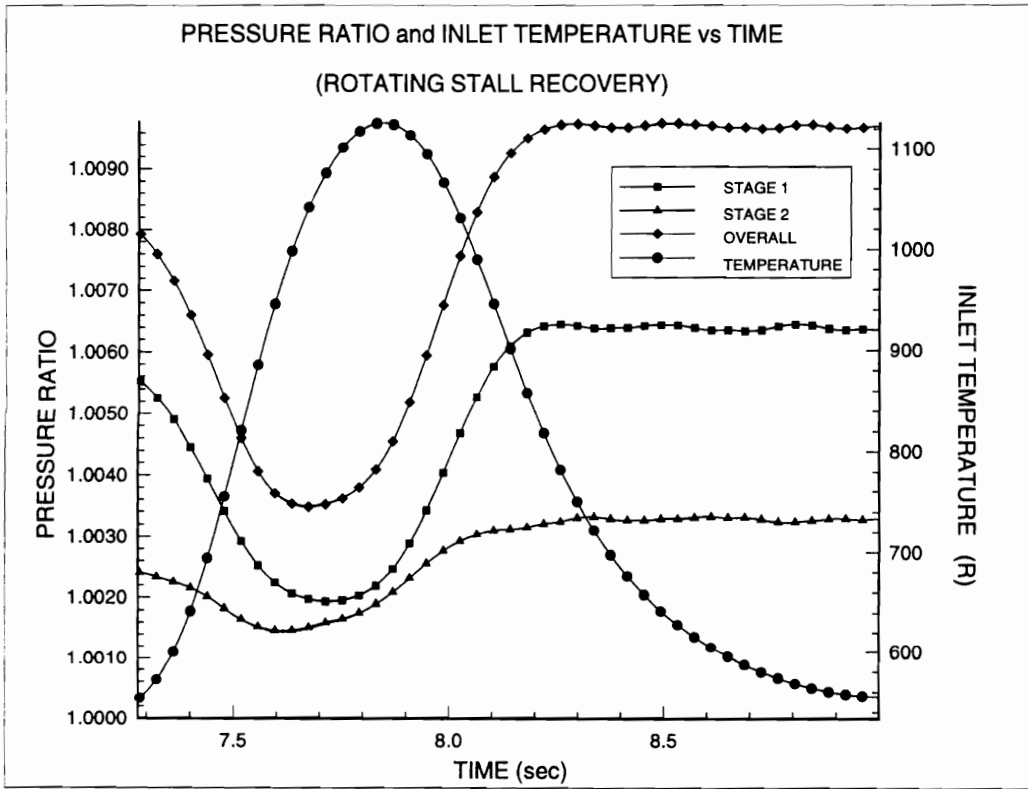


Figure 10.1 Pressure Ratio and Inlet Temperature vs Time (Rotating Stall Recovery)

Metric Conversions

$$K = 273.0 + \frac{5}{9}[R - 492.0]$$

$$\frac{kg}{s} = \frac{lbm}{sec} (0.45359237)$$

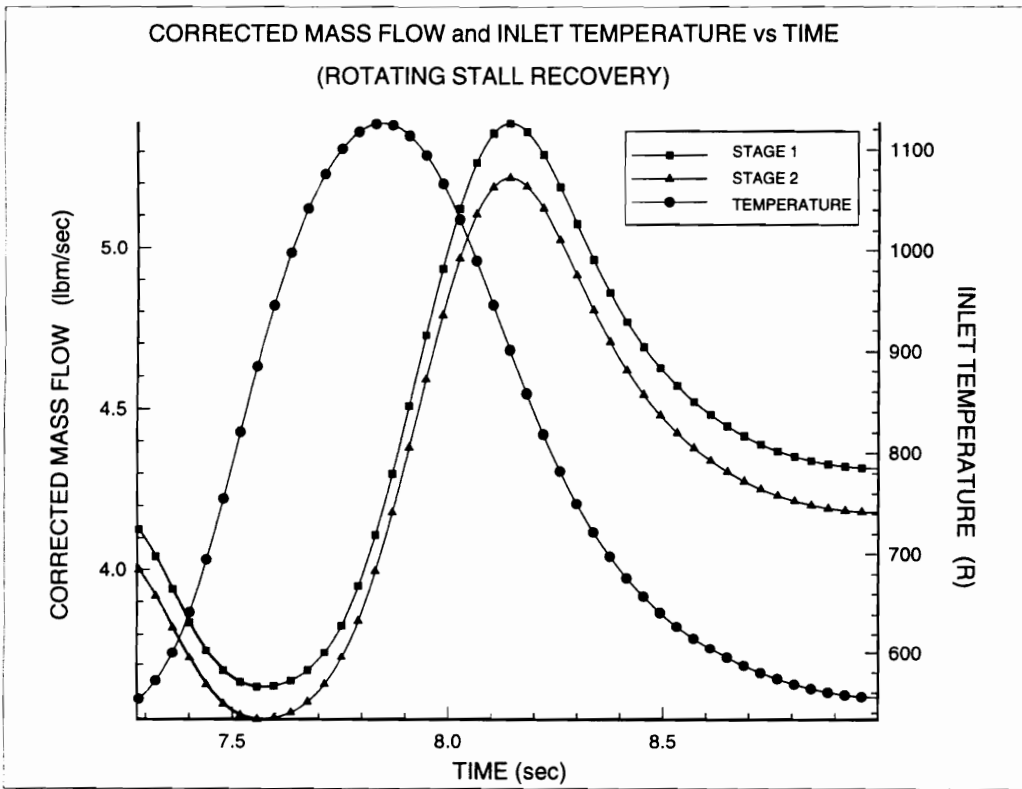


Figure 10.2 Corrected Mass Flow and Inlet Temperature vs Time (Rotating Stall Recovery)

Metric Conversions

$$K = 273.0 + \frac{5}{9} [R - 492.0]$$

$$\frac{\text{kg}}{\text{m}^3} = \frac{\text{lbm}}{\text{ft}^3} (16.00616434)$$

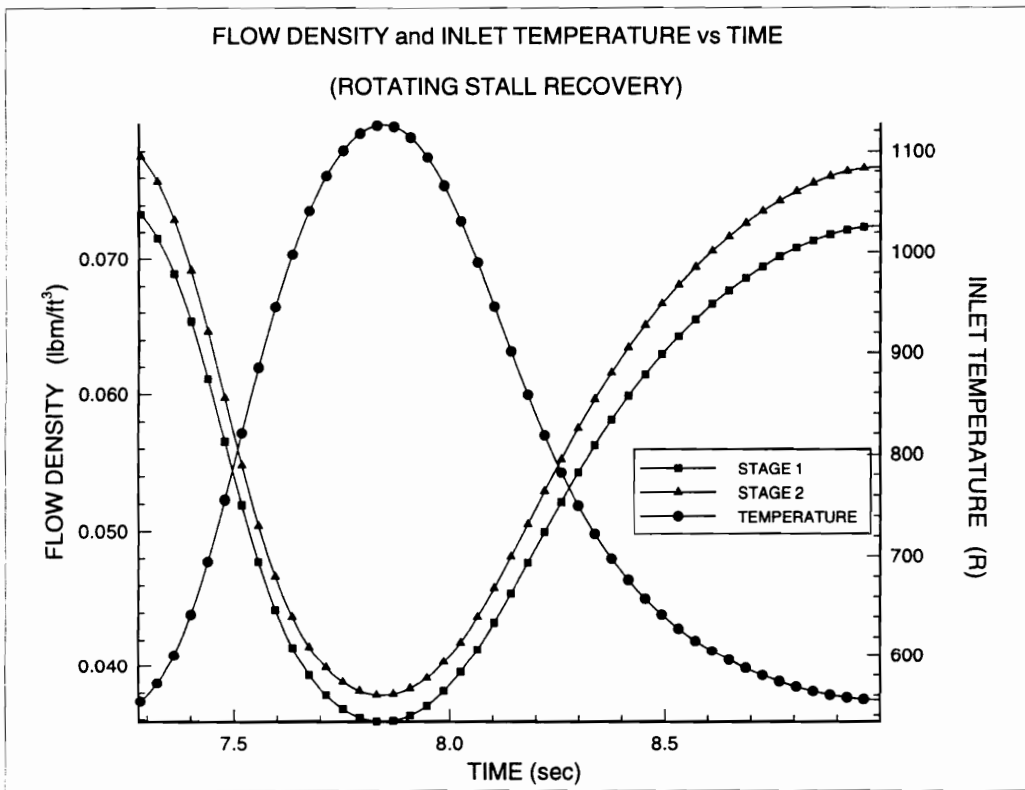


Figure 10.3 Flow Density and Inlet Temperature vs Time (Rotating Stall Recovery)

Metric Conversions

$$K = 273.0 + \frac{5}{9}[R - 492.0]$$

$$\frac{m}{s} = \frac{ft}{sec}(0.304878048)$$

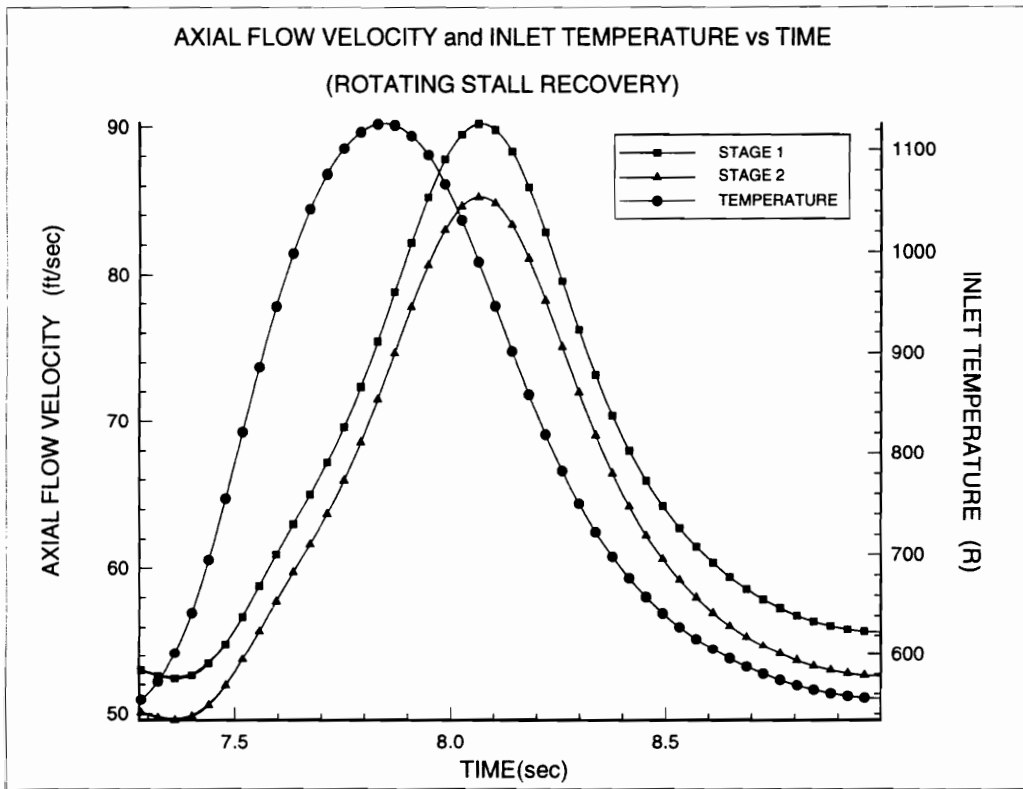


Figure 10.4 Axial Flow Velocity and Inlet Temperature vs Time (Rotating Stall Recovery)

Metric Conversions

$$K = 273.0 + \frac{5}{9}[R - 492.0]$$

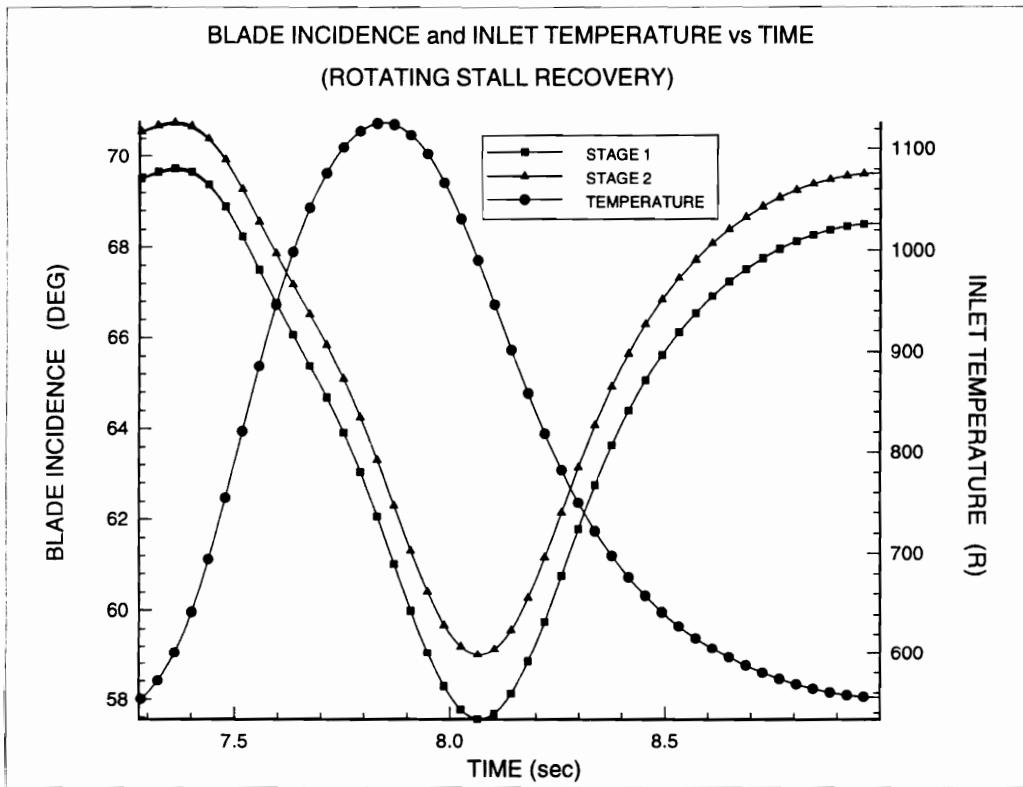


Figure 10.5 Blade Incidence and Inlet Temperature vs Time (Rotating Stall Recovery)

Metric Conversions

$$K = 273.0 + \frac{5}{9}[R - 492.0]$$

$$m^2 = ft^2 (0.092950624)$$

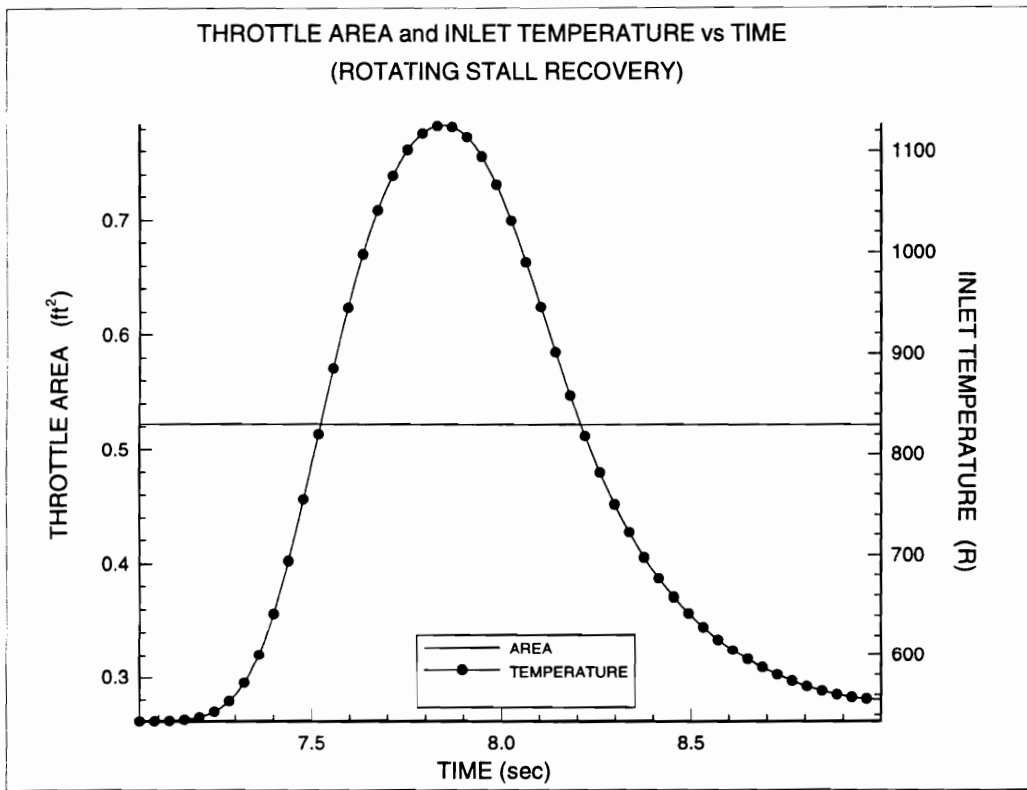


Figure 10.6 Throttle Area and Inlet Temperature vs Time (Rotating Stall Recovery)

10.2 Additional Plots For Experiment 2, (No Rotating Stall Recovery)

The following additional data plots are presented for experiment 2, the compressor **no rotating stall recovery** experiment :

- 1) Pressure Ratio vs Time vs Inlet Temperature
- 2) Corrected Mass Flow vs Time vs Inlet Temperature
- 3) Flow Density vs Time vs Inlet Temperature
- 4) Axial Flow Velocity vs Time vs Inlet Temperature
- 5) Blade Incidence vs Time vs Inlet Temperature
- 6) Throttle Area vs Time vs Inlet Temperature

Metric Conversions

$$K = 273.0 + \frac{5}{9}[R - 492.0]$$

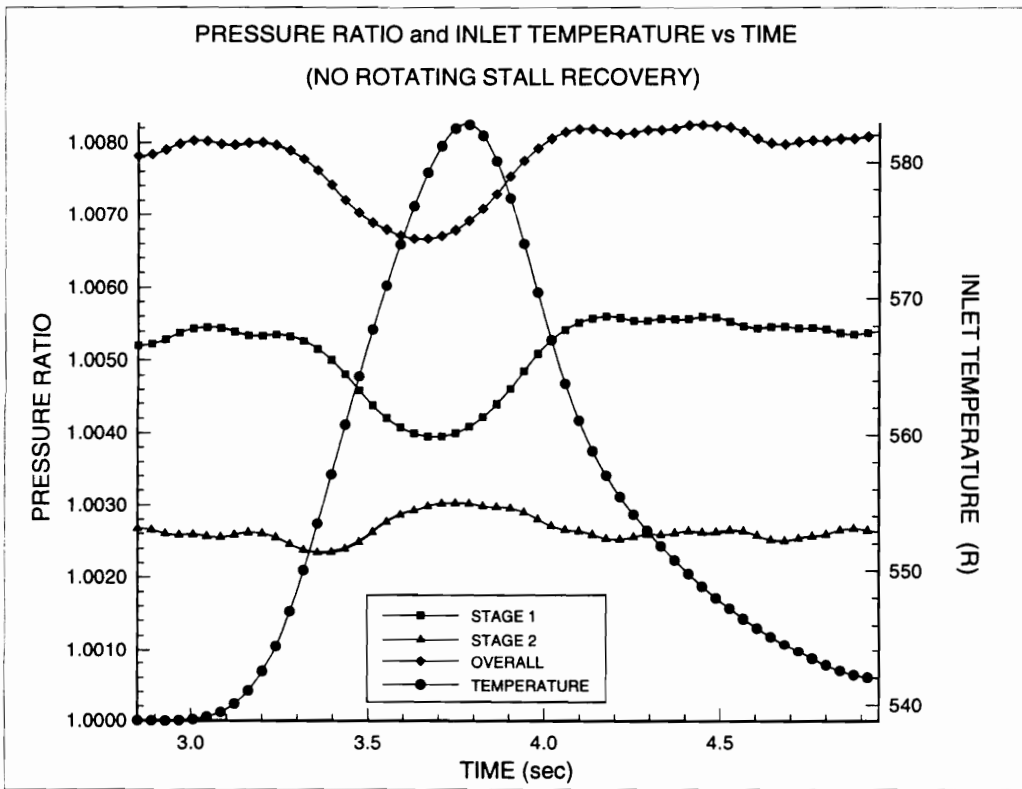


Figure 10.7 Pressure Ratio and Inlet Temperature vs Time
(No Rotating Stall Recovery)

Metric Conversions

$$K = 273.0 + \frac{5}{9}[R - 492.0]$$

$$\frac{\text{kg}}{\text{s}} = \frac{\text{lbm}}{\text{sec}}(0.45359237)$$

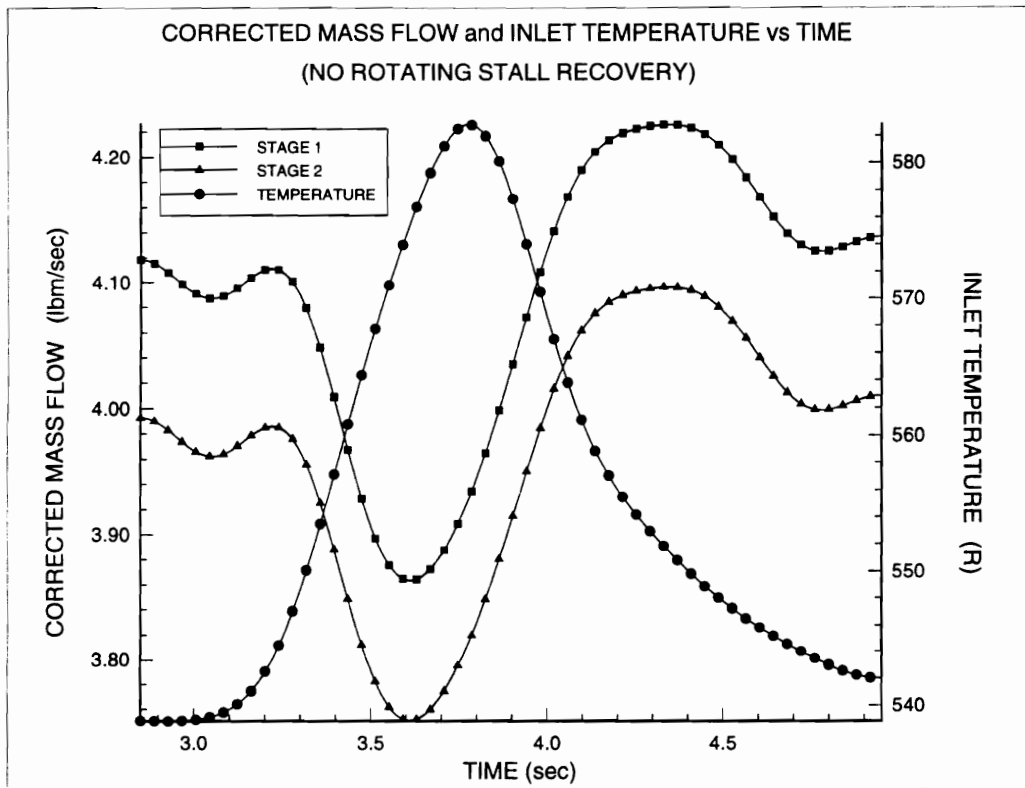


Figure 10.8 Corrected Mass Flow and Inlet Temperature vs Time (No Rotating Stall Recovery)

Metric Conversions

$$K = 273.0 + \frac{5}{9}[R - 492.0]$$

$$\frac{\text{kg}}{\text{m}^3} = \frac{\text{lbm}}{\text{ft}^3} (16.00616434)$$

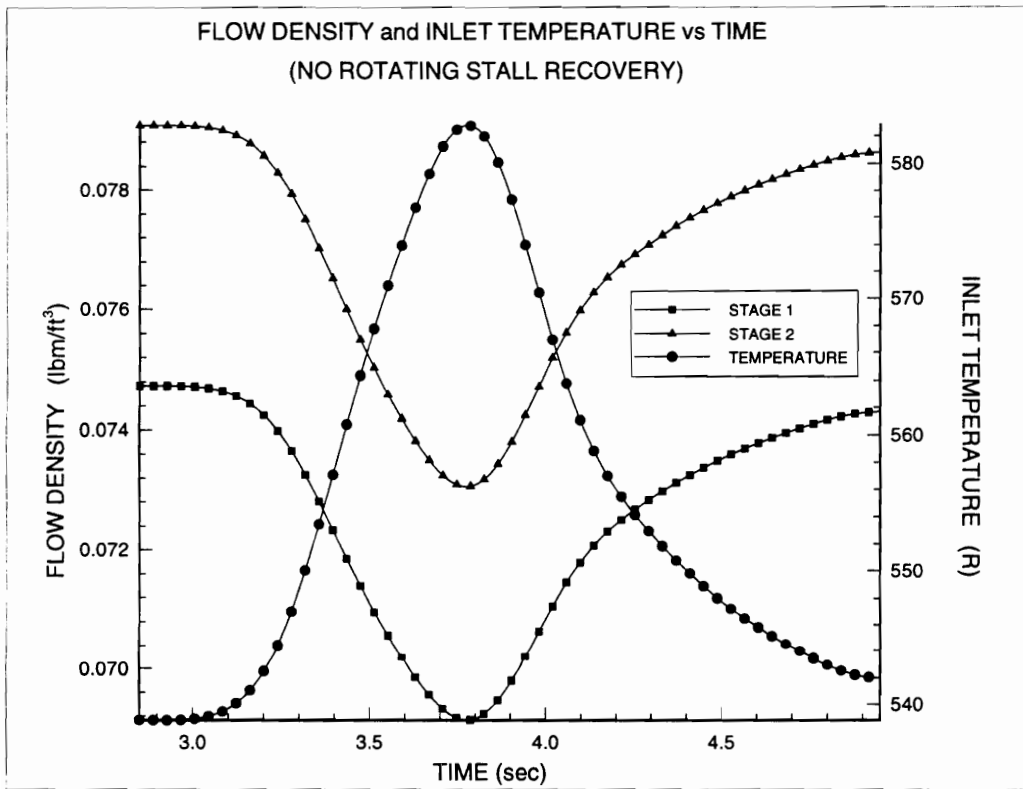


Figure 10.9 Flow Density and Inlet Temperature vs Time (No Rotating Stall Recovery)

Metric Conversions

$$K = 273.0 + \frac{5}{9}[R - 492.0]$$

$$\frac{m}{s} = \frac{ft}{sec}(0.304878048)$$

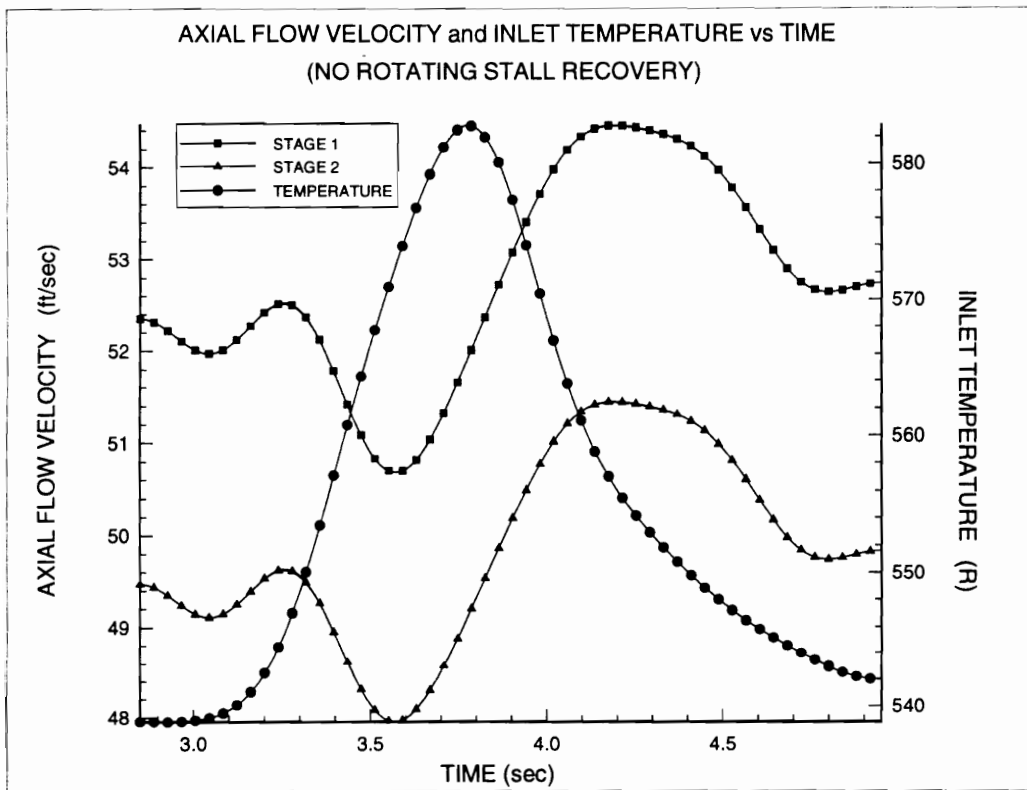


Figure 10.10 Axial Flow Velocity and Inlet Temperature vs Time (No Rotating Stall Recovery)

Metric Conversions

$$K = 273.0 + \frac{5}{9}[R - 492.0]$$

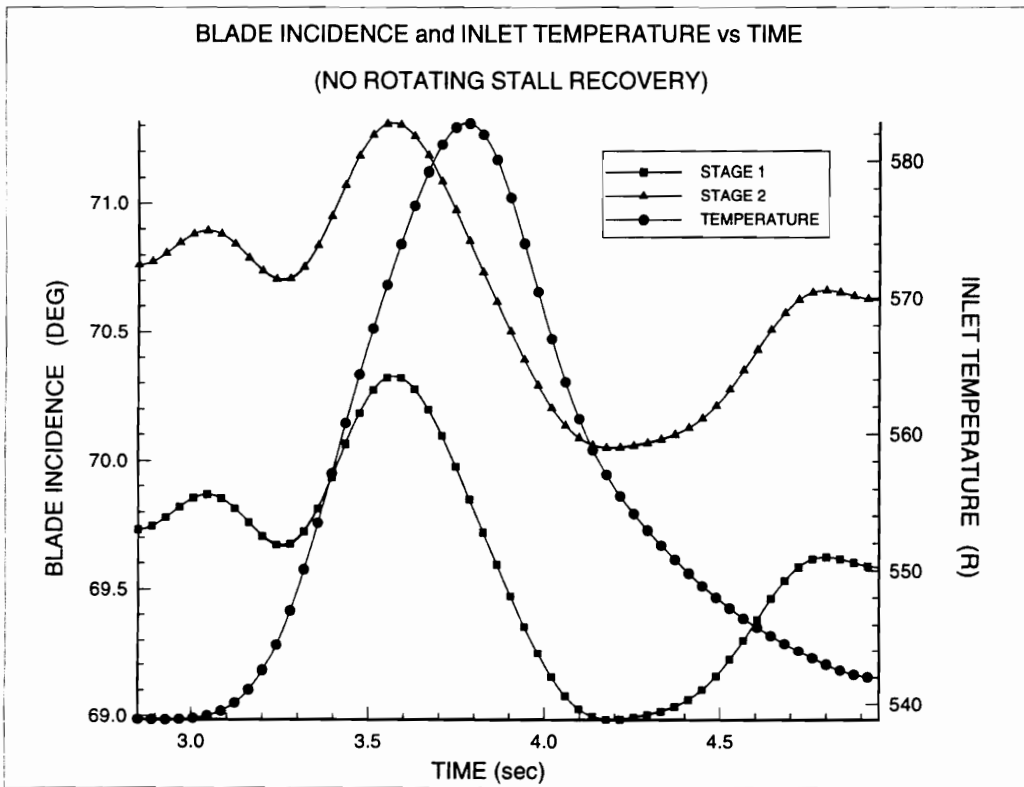


Figure 10.11 Blade Incidence and Inlet Temperature vs Time (No Rotating Stall Recovery)

Metric Conversions

$$K = 273.0 + \frac{5}{9}[R - 492.0]$$

$$m^2 = ft^2 (0.092950624)$$

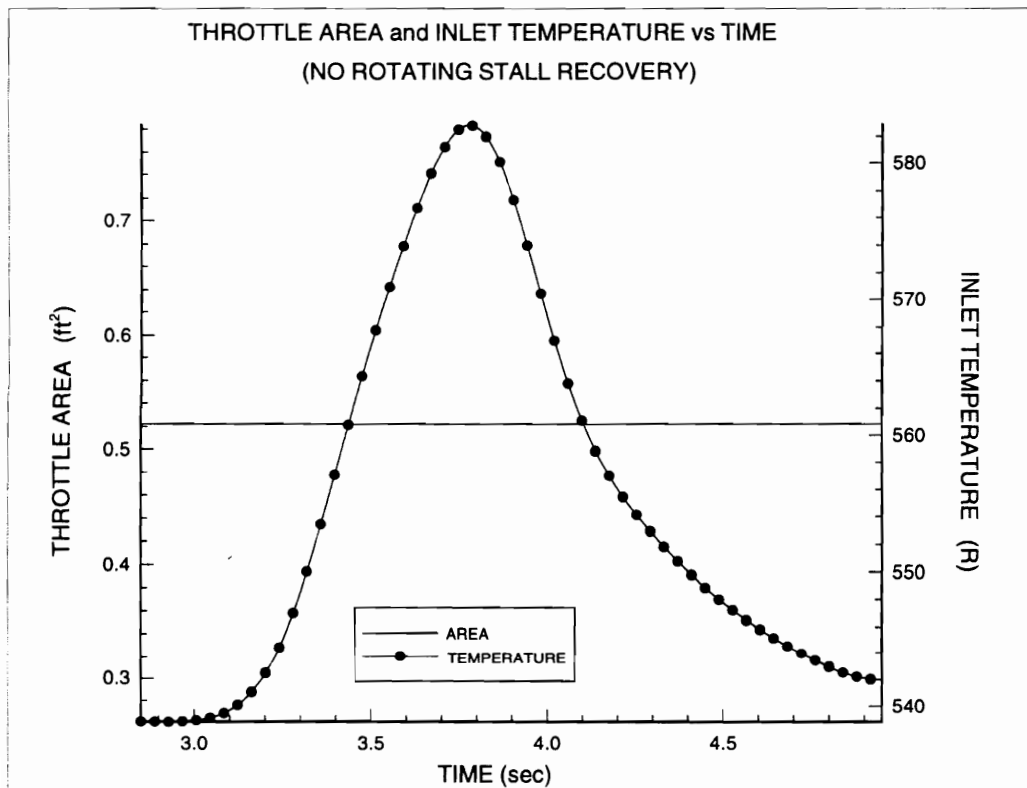


Figure 10.12 Throttle Area and Inlet Temperature vs Time
(No Rotating Stall Recovery)

10.3 Additional Plots For Experiment 3, (Induced Stall)

The following additional data plots are presented for experiment 3, the compressor induced **stall** experiment :

- 1) Pressure Ratio vs Time vs Inlet Temperature
- 2) Corrected Mass Flow vs Time vs Inlet Temperature
- 3) Flow Density vs Time vs Inlet Temperature
- 4) Axial Flow Velocity vs Time vs Inlet Temperature
- 5) Blade Incidence vs Time vs Inlet Temperature
- 6) Throttle Area vs Time vs Inlet Temperature

Metric Conversions

$$K = 273.0 + \frac{5}{9} [R - 492.0]$$

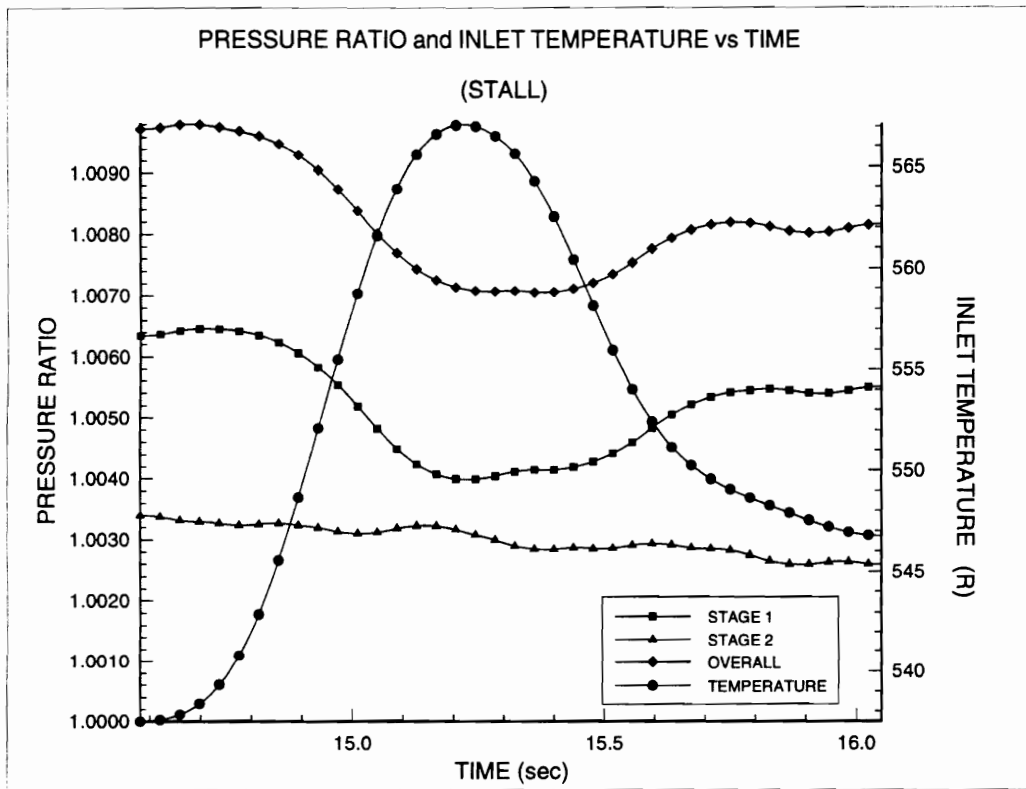


Figure 10.13 Pressure Ratio and Inlet Temperature vs Time (Stall)

Metric Conversions

$$K = 273.0 + \frac{5}{9}[R - 492.0]$$

$$\frac{kg}{s} = \frac{lbm}{sec} (0.45359237)$$

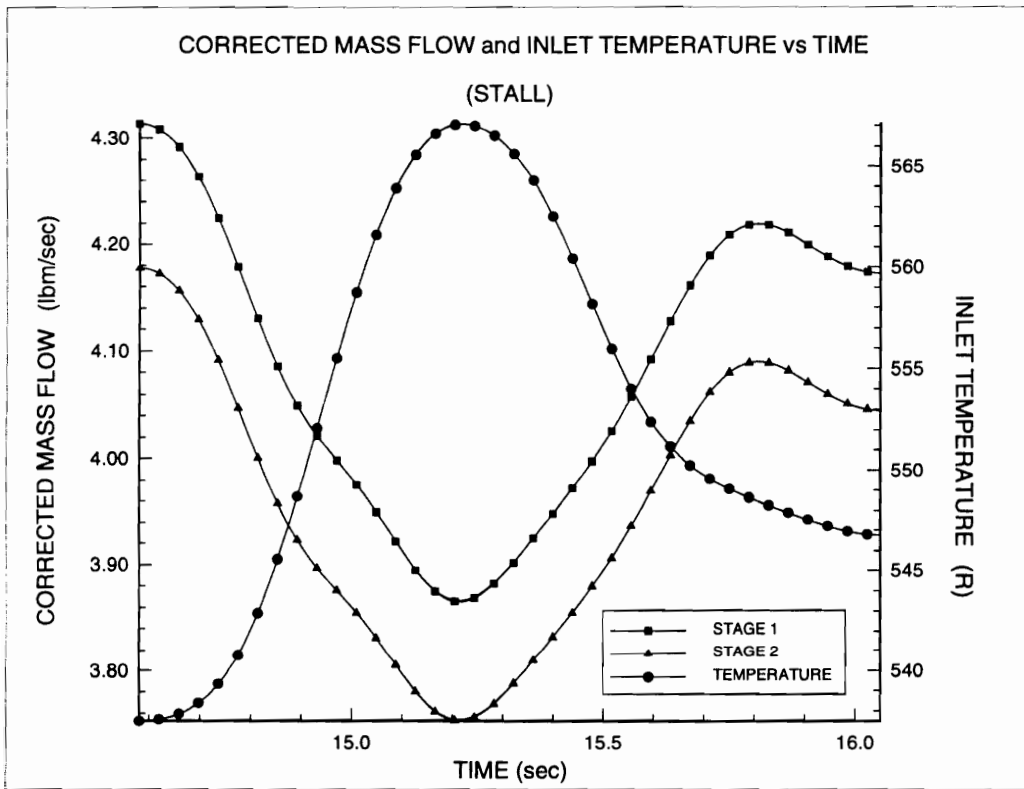


Figure 10.14 Corrected Mass Flow and Inlet Temperature vs Time (Stall)

Metric Conversions

$$K = 273.0 + \frac{5}{9}[R - 492.0]$$

$$\frac{\text{kg}}{\text{m}^3} = \frac{\text{lbm}}{\text{ft}^3} (16.00616434)$$

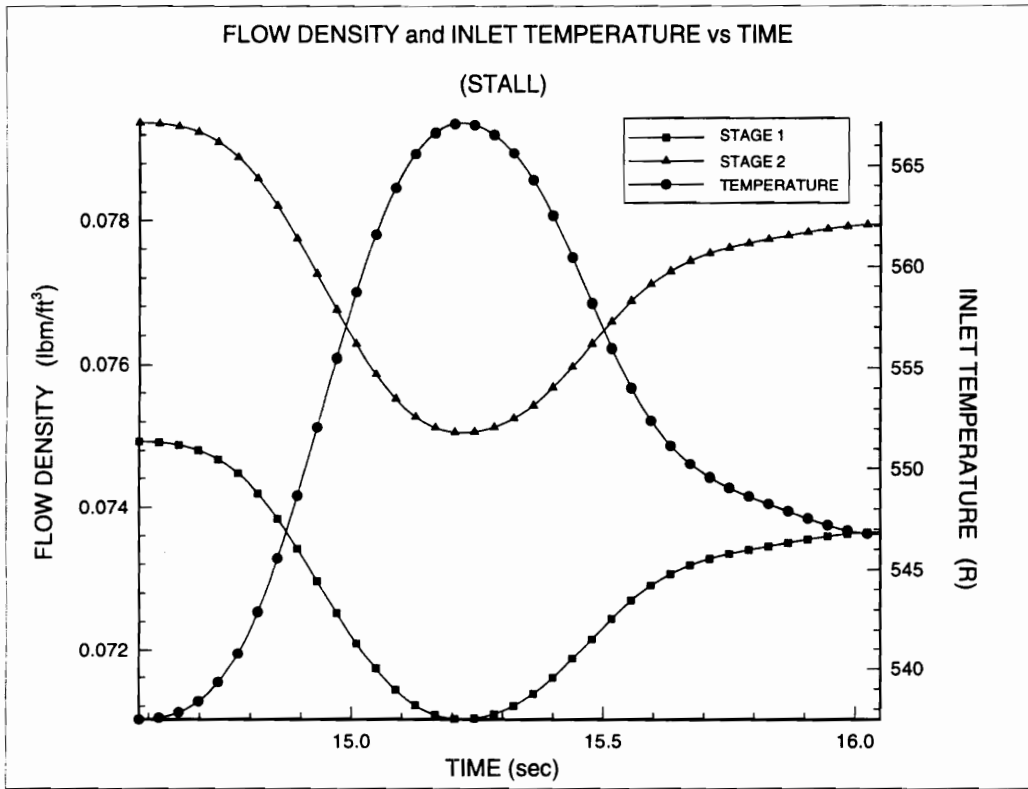


Figure 10.15 Flow Density and Inlet Temperature vs Time (Stall)

Metric Conversions

$$K = 273.0 + \frac{5}{9}[R - 492.0]$$

$$\frac{m}{s} = \frac{ft}{sec} (0.304878048)$$

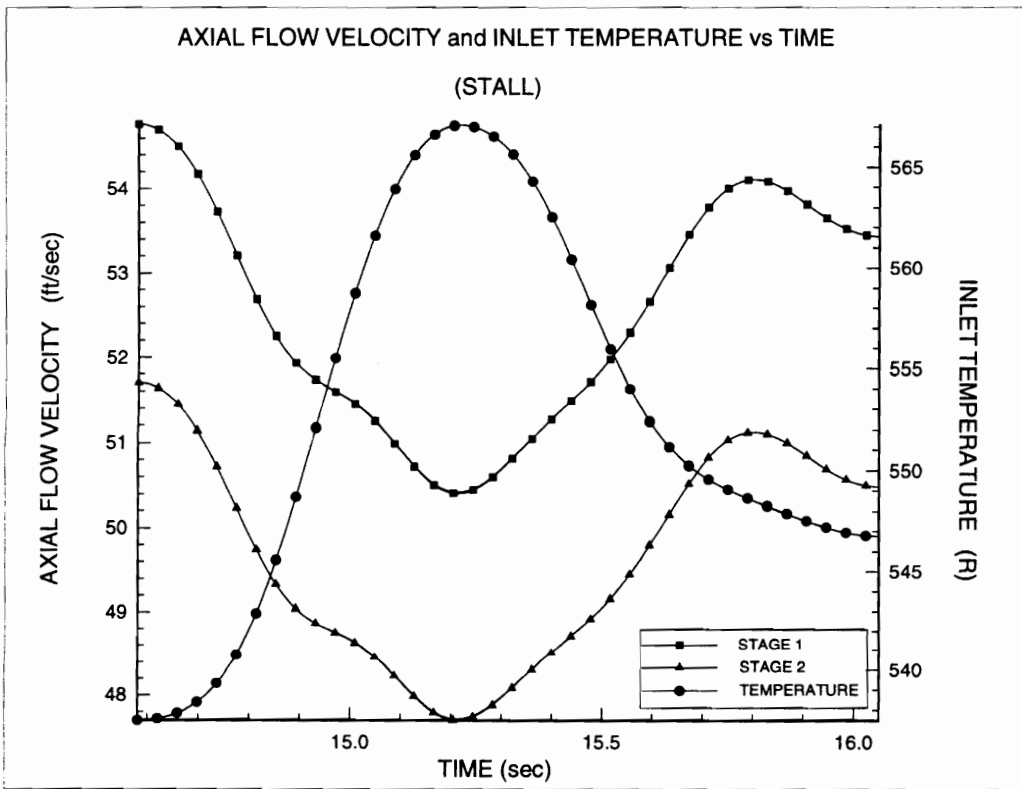


Figure 10.16 Axial Flow Velocity and Inlet Temperature vs Time (Stall)

Metric Conversions

$$K = 273.0 + \frac{5}{9}[R - 492.0]$$

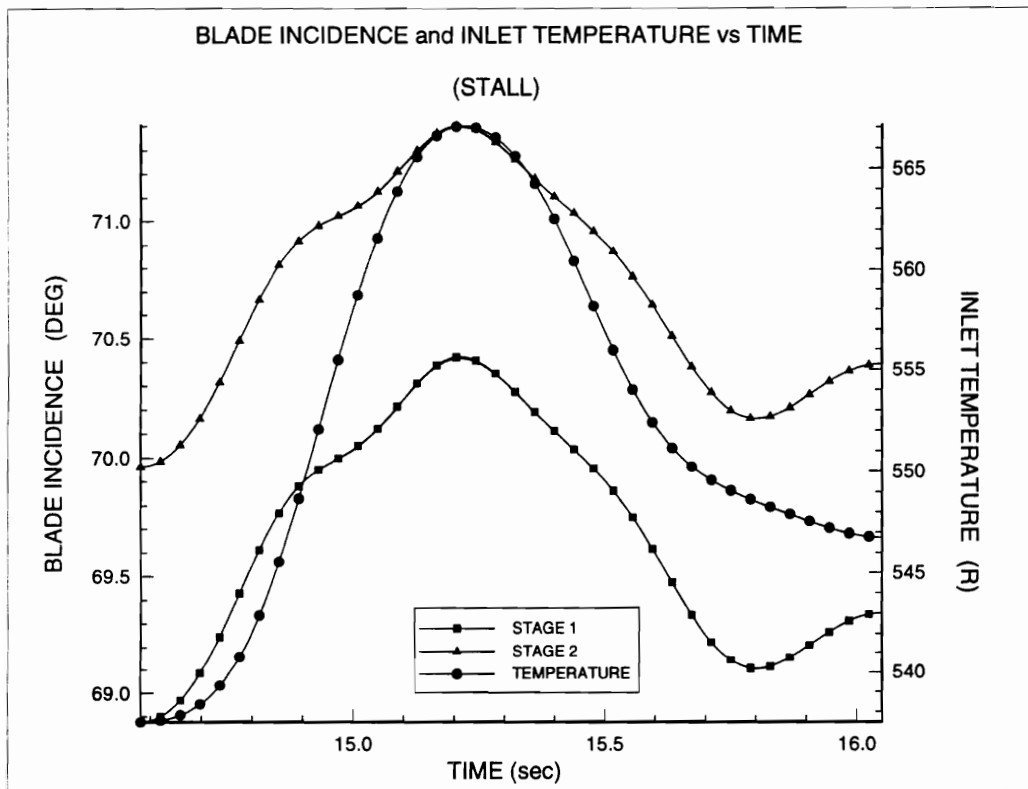


Figure 10.17 Blade Incidence and Inlet Temperature vs Time (Stall)

Metric Conversions

$$K = 273.0 + \frac{5}{9}[R - 492.0]$$

$$m^2 = ft^2 (0.092950624)$$

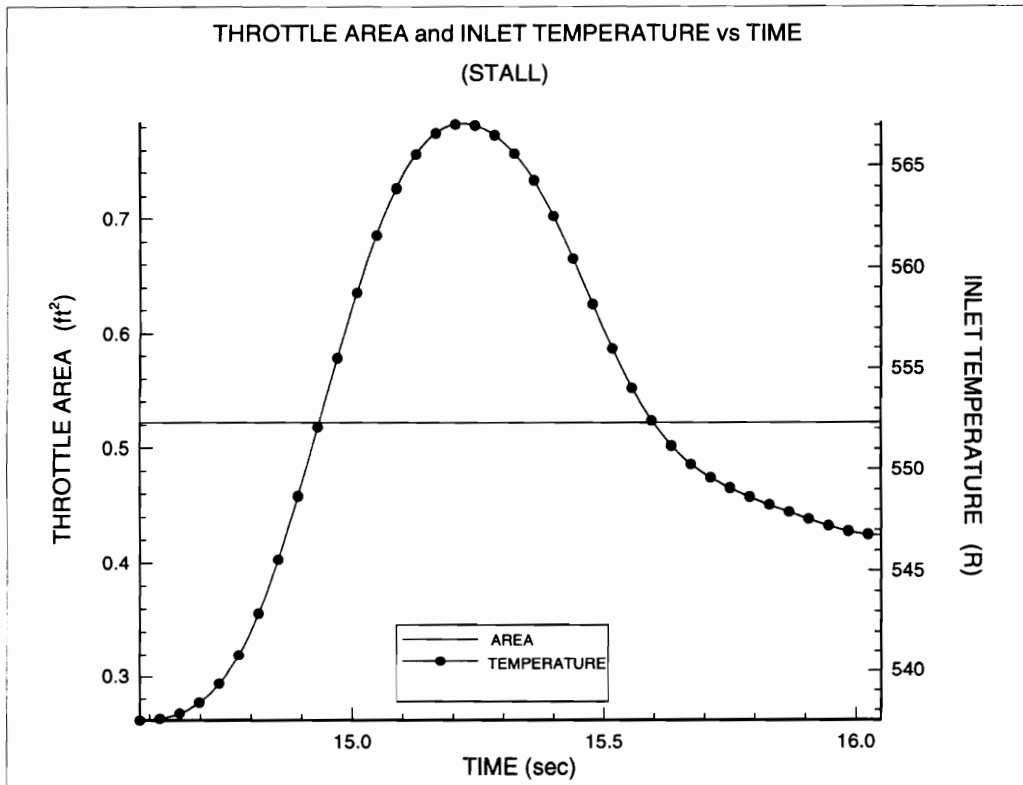


Figure 10.18 Throttle Area and Inlet Temperature vs Time (Stall)

10.4 Additional Plots For Experiment 4, (No Induced Stall)

The following additional data plots are presented for experiment 4, the compressor **no stall** experiment :

- 1) Pressure Ratio vs Time vs Inlet Temperature
- 2) Corrected Mass Flow vs Time vs Inlet Temperature
- 3) Flow Density vs Time vs Inlet Temperature
- 4) Axial Flow Velocity vs Time vs Inlet Temperature
- 5) Blade Incidence vs Time vs Inlet Temperature
- 6) Throttle Area vs Time vs Inlet Temperature

Metric Conversions

$$K = 273.0 + \frac{5}{9}[R - 492.0]$$

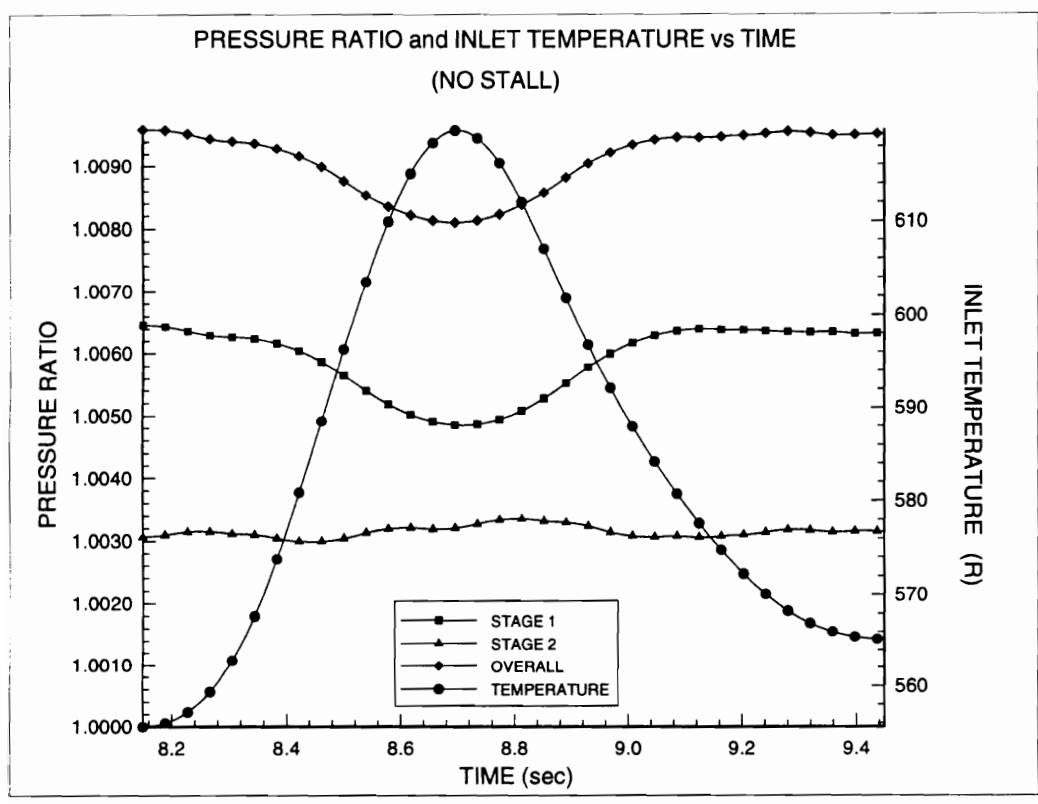


Figure 10.19 Pressure Ratio and Inlet Temperature vs Time (No Stall)

Metric Conversions

$$K = 273.0 + \frac{5}{9}[R - 492.0]$$

$$\frac{\text{kg}}{\text{s}} = \frac{\text{lbm}}{\text{sec}}(0.45359237)$$

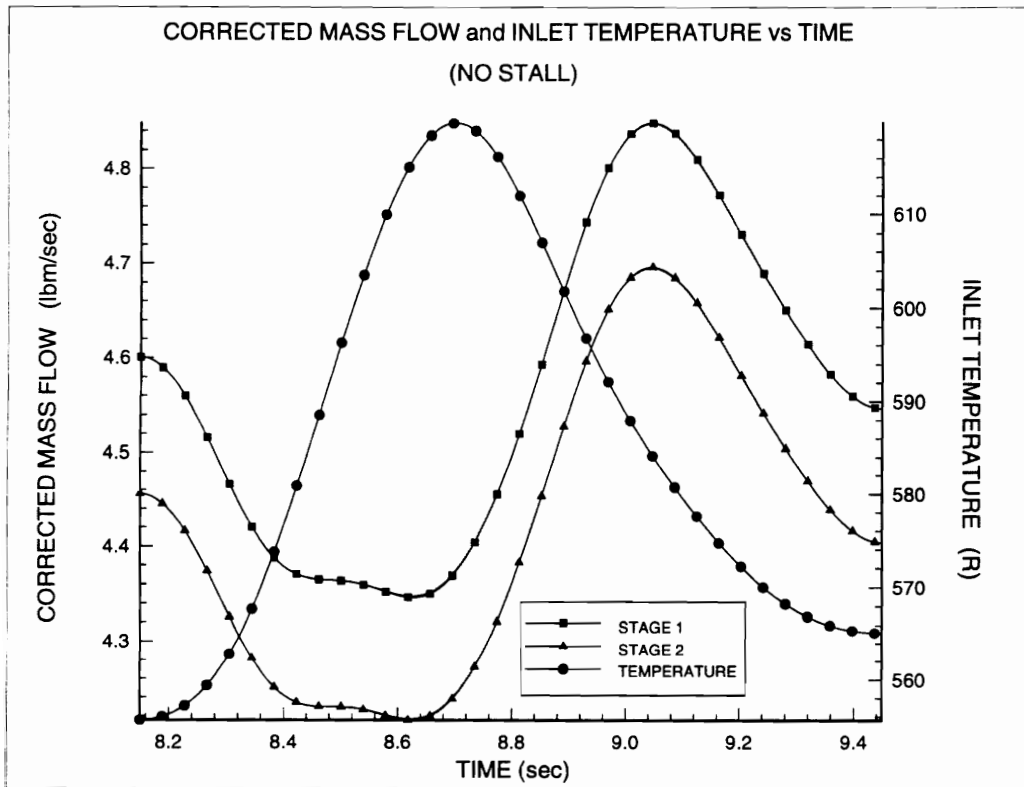


Figure 10.20 Corrected Mass Flow and Inlet Temperature vs Time
(No Stall)

Metric Conversions

$$K = 273.0 + \frac{5}{9}[R - 492.0]$$

$$\frac{\text{kg}}{\text{m}^3} = \frac{\text{lbm}}{\text{ft}^3} (16.00616434)$$

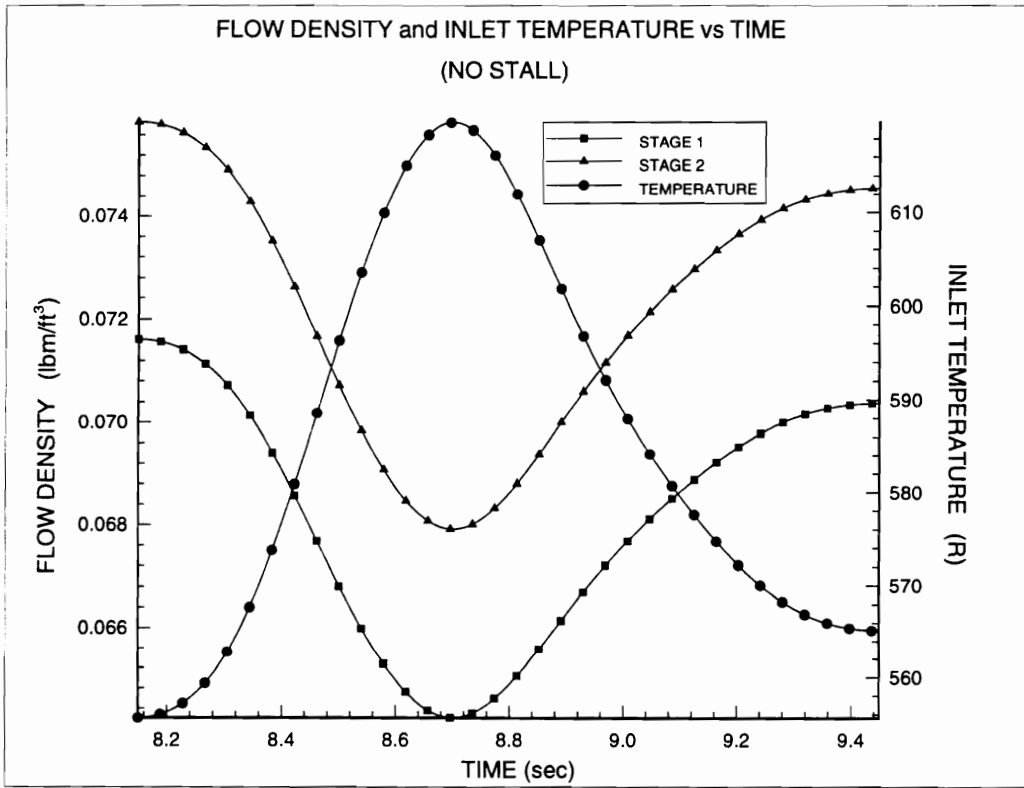


Figure 10.21 Flow Density and Inlet Temperature vs Time (No Stall)

Metric Conversions

$$K = 273.0 + \frac{5}{9}[R - 492.0]$$

$$\frac{m}{s} = \frac{ft}{sec} (0.304878048)$$

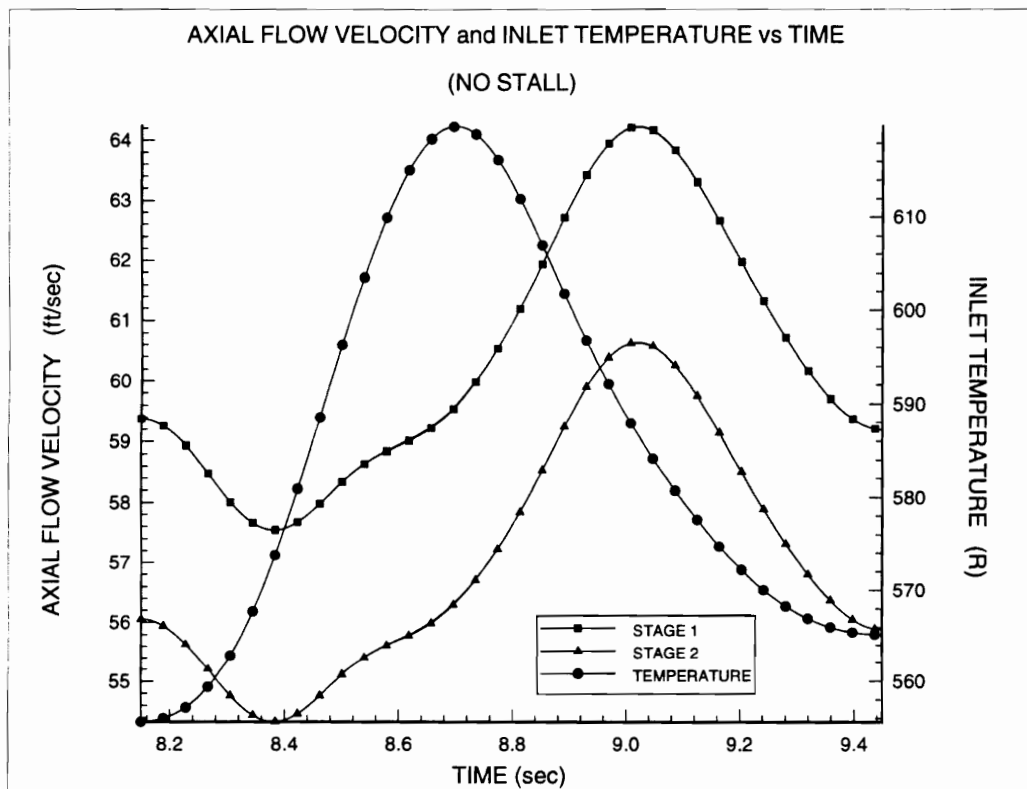


Figure 10.22 Axial Flow Velocity and Inlet Temperature vs Time (No Stall)

Metric Conversions

$$K = 273.0 + \frac{5}{9}[R - 492.0]$$

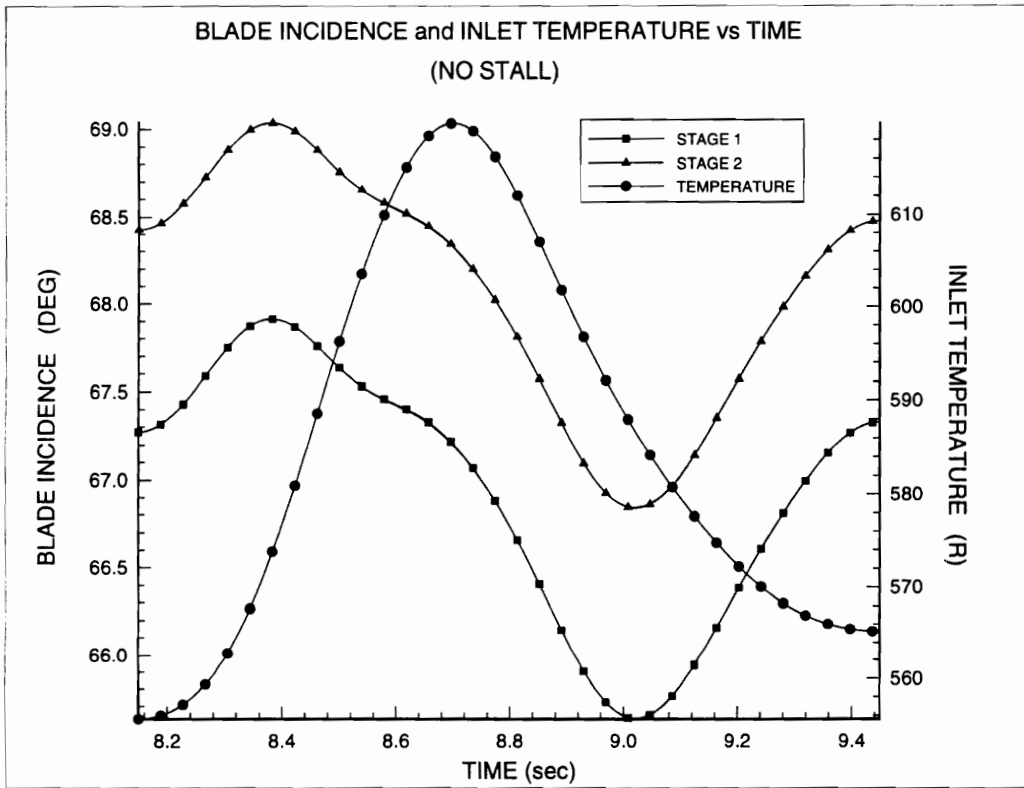


Figure 10.23 Blade Incidence and Inlet Temperature vs Time (No Stall)

Metric Conversions

$$K = 273.0 + \frac{5}{9}[R - 492.0]$$

$$m^2 = ft^2 (0.092950624)$$

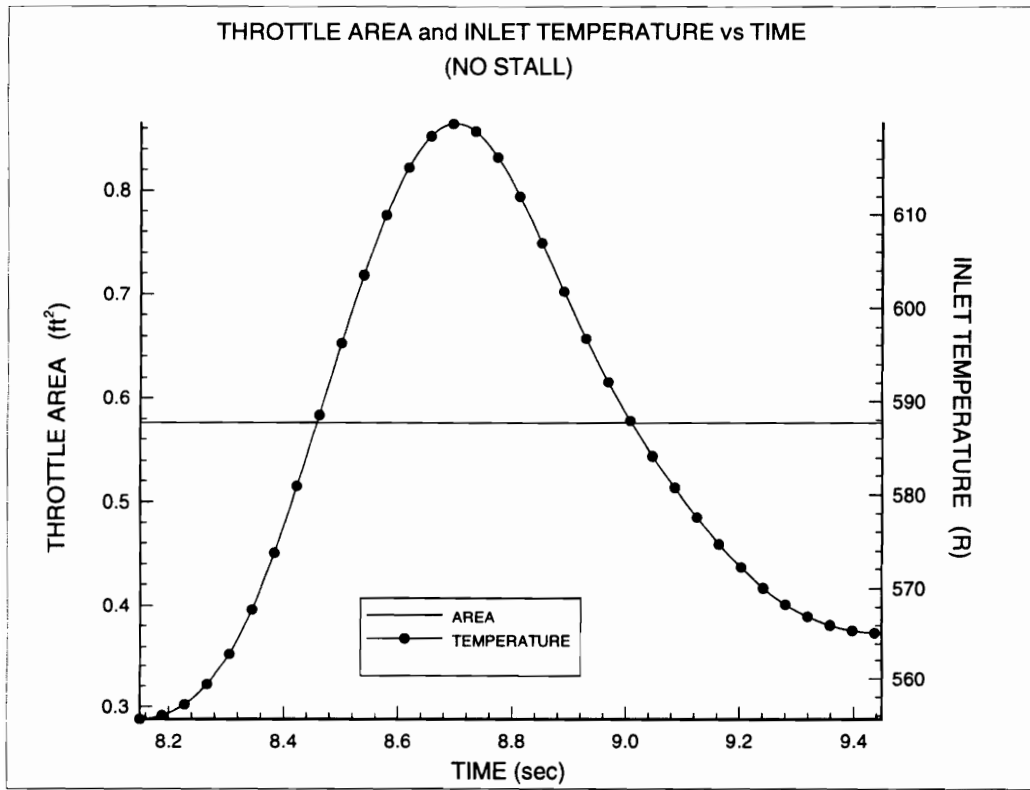


Figure 10.24 Throttle Area and Inlet Temperature vs Time (No Stall)

10.5 Additional Plots For Experiment 5, (Stall Followed By An Immediate Recovery)

The following additional data plots are presented for experiment 5, the compressor **stall followed by an immediate recovery** experiment :

- 1) Pressure Ratio vs Time vs Inlet Temperature
- 2) Corrected Mass Flow vs Time vs Inlet Temperature
- 3) Flow Density vs Time vs Inlet Temperature
- 4) Axial Flow Velocity vs Time vs Inlet Temperature
- 5) Blade Incidence vs Time vs Inlet Temperature
- 6) Throttle Area vs Time vs Inlet Temperature

Metric Conversions

$$K = 273.0 + \frac{5}{9}[R - 492.0]$$

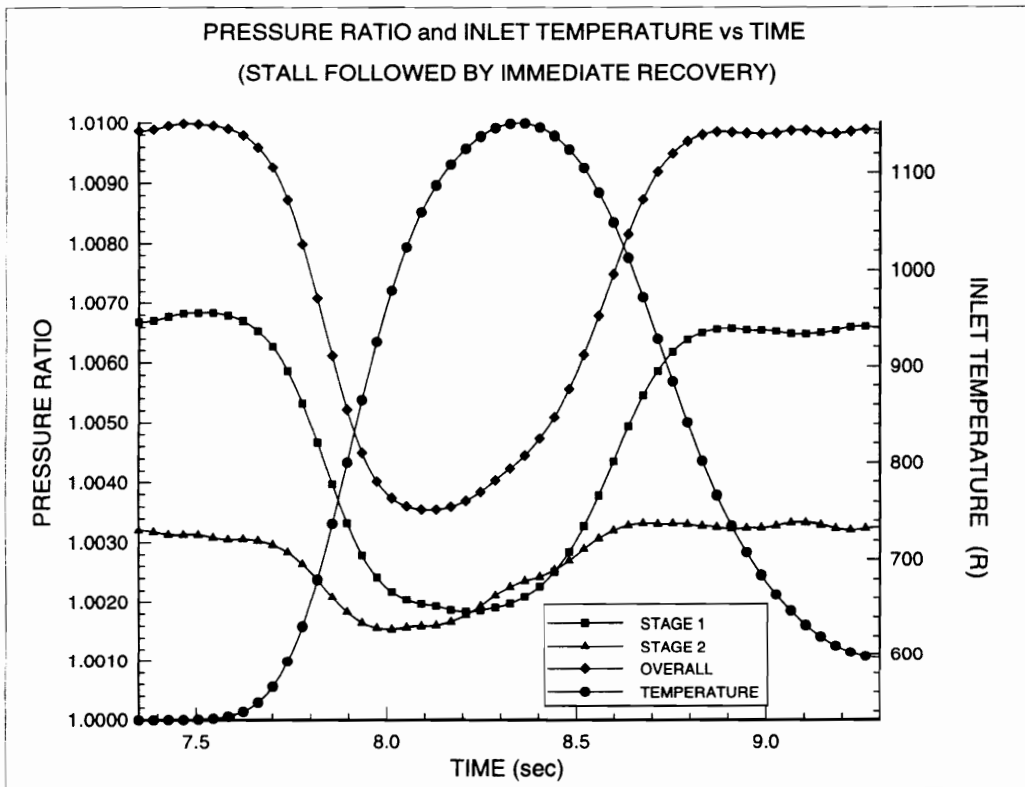


Figure 10.25 Pressure Ratio and Inlet Temperature vs Time (Stall Followed By An Immediate Recovery)

Metric Conversions

$$K = 273.0 + \frac{5}{9}[R - 492.0]$$

$$\frac{\text{kg}}{\text{s}} = \frac{\text{lbm}}{\text{sec}} (0.45359237)$$

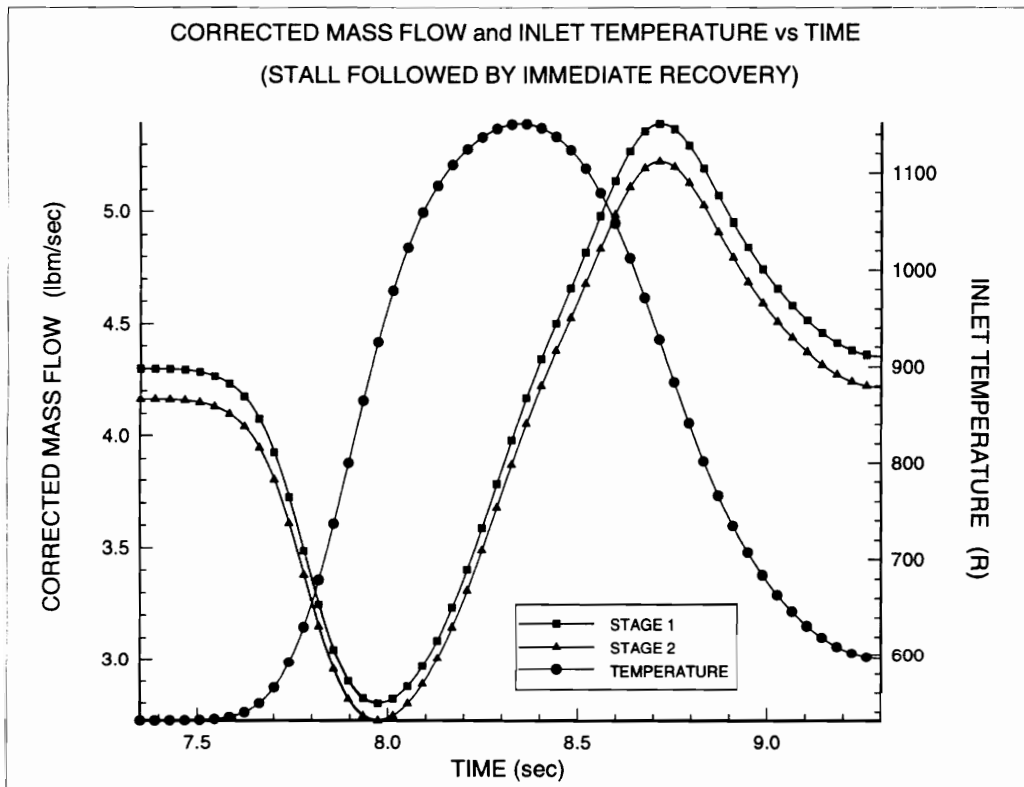


Figure 10.26 Corrected Mass Flow and Inlet Temperature vs Time (Stall Followed By An Immediate Recovery)

Metric Conversions

$$K = 273.0 + \frac{5}{9}[R - 492.0]$$

$$\frac{\text{kg}}{\text{m}^3} = \frac{\text{lbm}}{\text{ft}^3} (16.00616434)$$

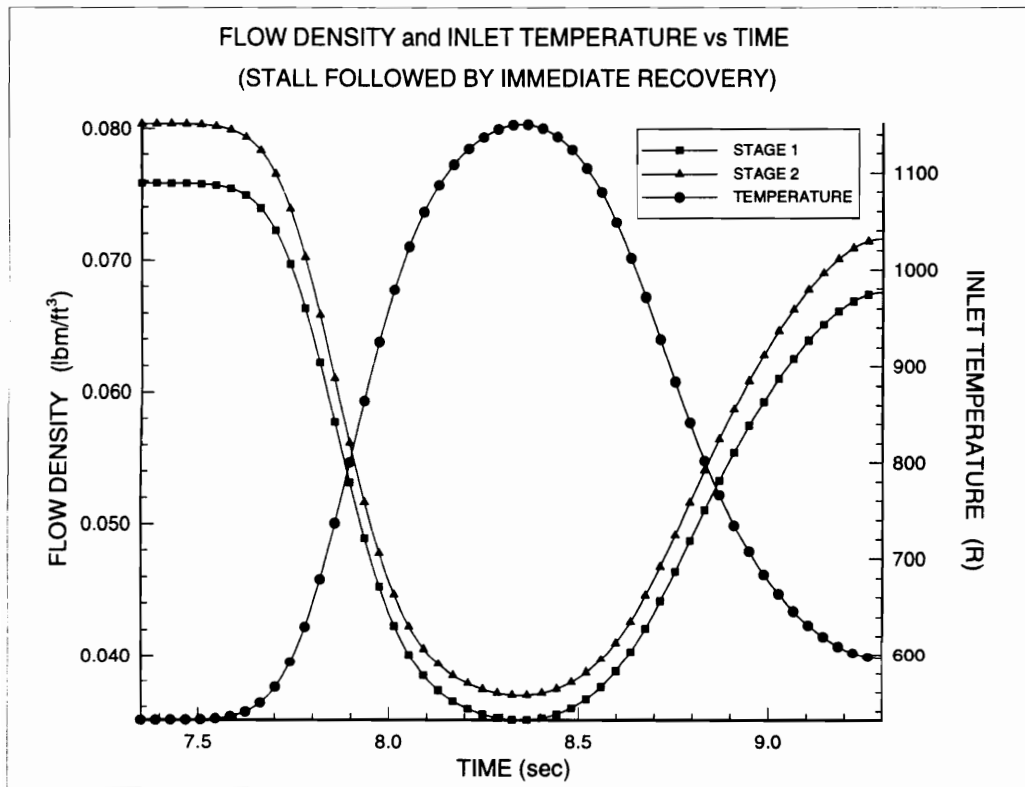


Figure 10.27 Flow Density and Inlet Temperature vs Time (Stall Followed By An Immediate Recovery)

Metric Conversions

$$K = 273.0 + \frac{5}{9}[R - 492.0]$$

$$\frac{m}{s} = \frac{ft}{sec} (0.304878048)$$

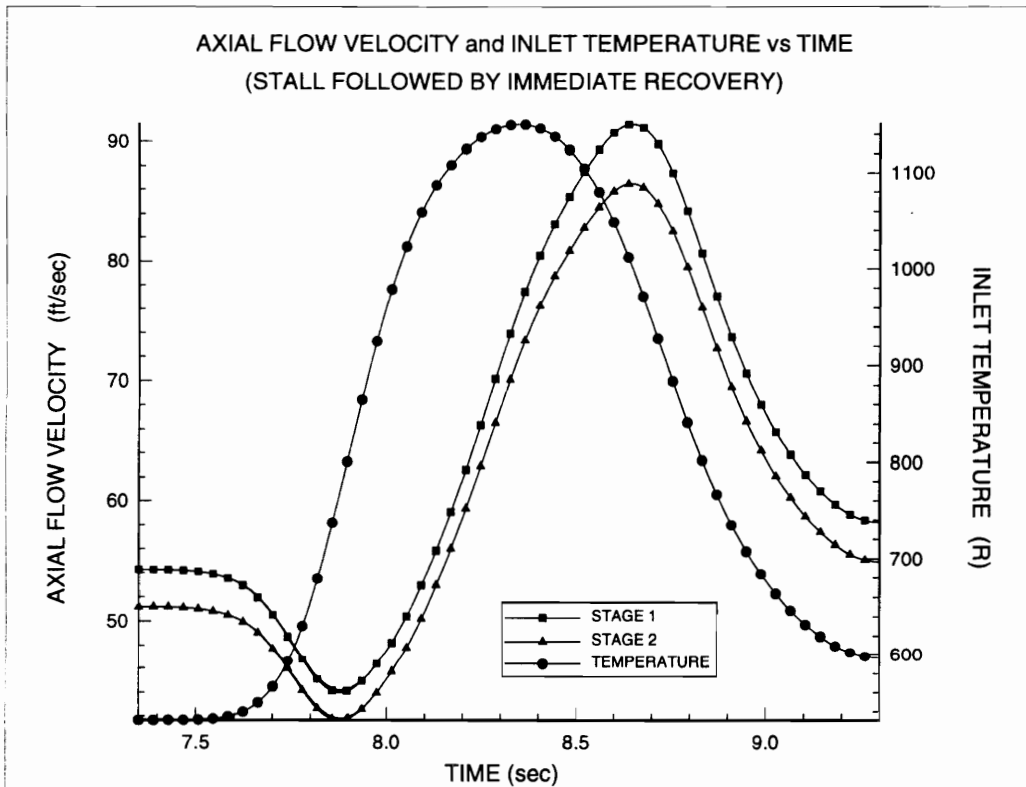


Figure 10.28 Axial Flow Velocity and Inlet Temperature vs Time (Stall Followed By An Immediate Recovery)

Metric Conversions

$$K = 273.0 + \frac{5}{9} [R - 492.0]$$

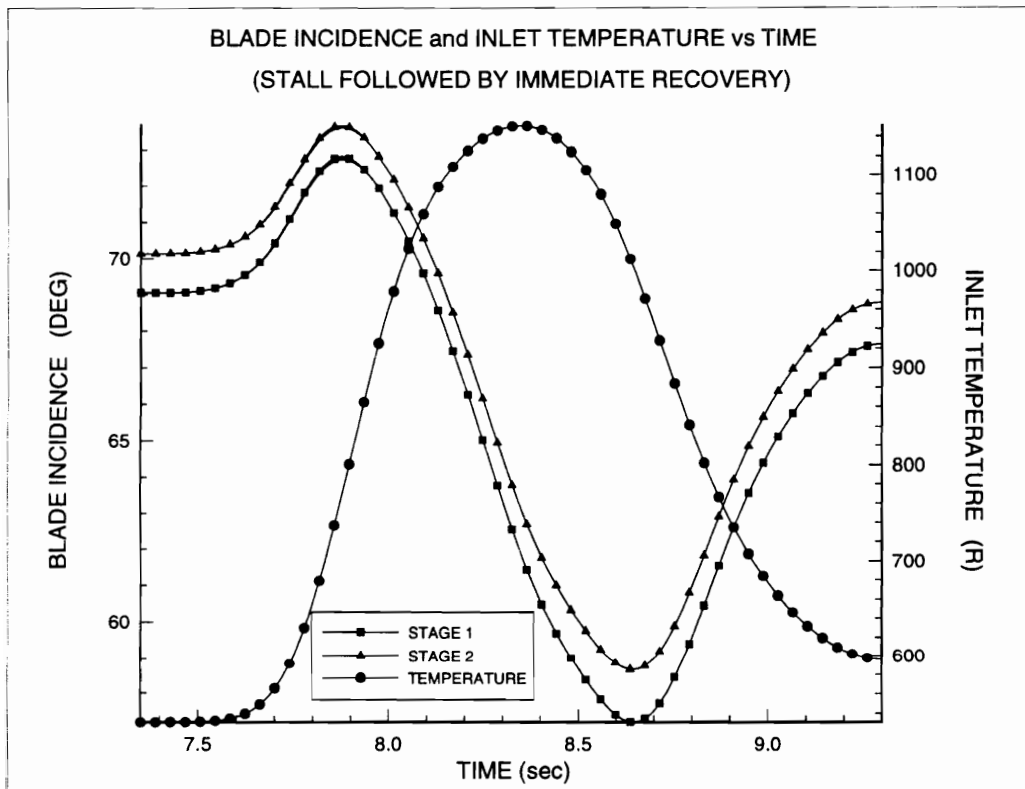


Figure 10.29 Blade Incidence and Inlet Temperature vs Time (Stall Followed By An Immediate Recovery)

Metric Conversions

$$K = 273.0 + \frac{5}{9}[R - 492.0]$$

$$m^2 = ft^2 (0.092950624)$$

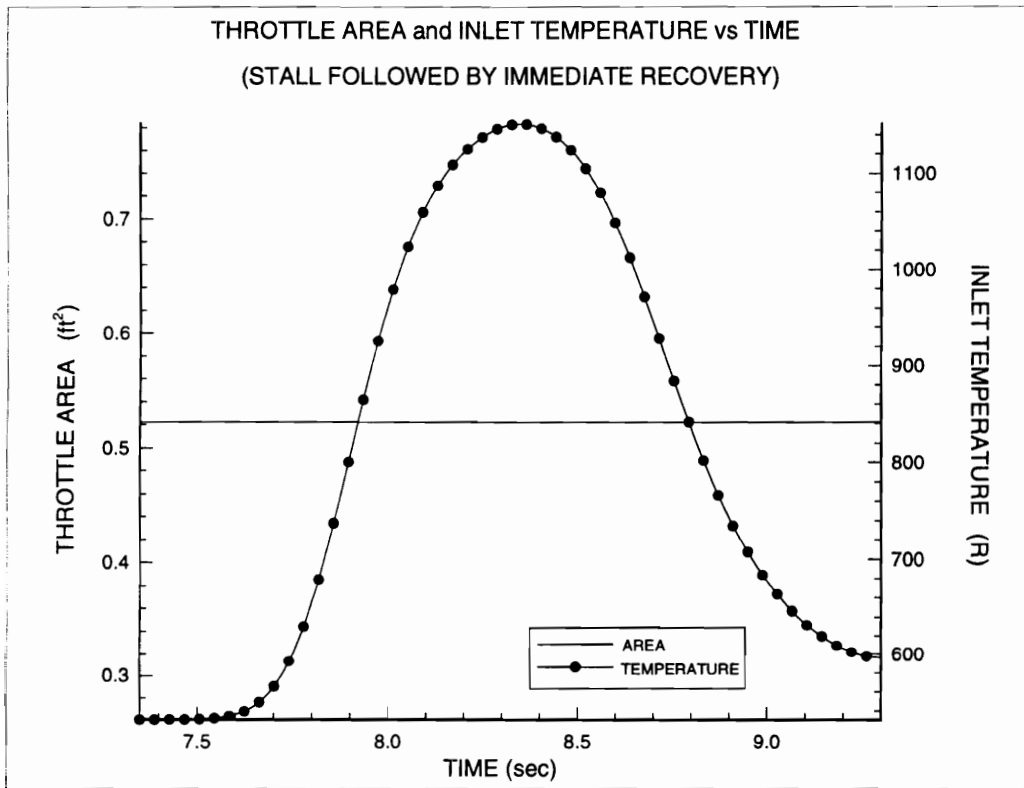


Figure 10.30 Throttle Area and Inlet Temperature vs Time (Stall Followed By An Immediate Recovery)

11. APPENDIX B

Instrument Calibration

Pressure Transducers

Calibration of the pressure transducers was accomplished using a Pyrex water tube and plunger along with a Dwyer gravity fluid manometer. A schematic of the calibration assembly is shown in Figure 11.1. The Datametrix Type 590 Integral Barocel pressure transducers were connected to Datametrix Type 1400 Electronic Manometers that had to initially be zeroed with zero differential pressure across the transducers. This task was performed according to the instruction manual for the Datametrix Type 590 Integral Barocel pressure transducer and the Datametrix Type 1400 Electronic Manometer. The OMEGA PX800-001GV high accuracy pressure transducers were supplied with the calibration constant determined by the manufacturer. This calibration constant was derived using the National Bureau of Standards for pressure measurements. All of the transducers read gauge pressure and produced zero volts when measuring atmospheric pressure.

It was known that the pressures to be measured in the experiment would be approximately in the range of 4 to 6 inches (0.1 to 0.15 m) of water or less. The water tube in Figure 11.1 was filled with six inches of water and the plunger inserted into the bottom of the tube. The pressure at the bottom of the water tube was now equivalent to the hydrostatic pressure produced by a column of water six inches high. This fact was verified by the Dwyer gravity fluid manometer (SG 0.827), also connected in the pressure

Calibration Apparatus

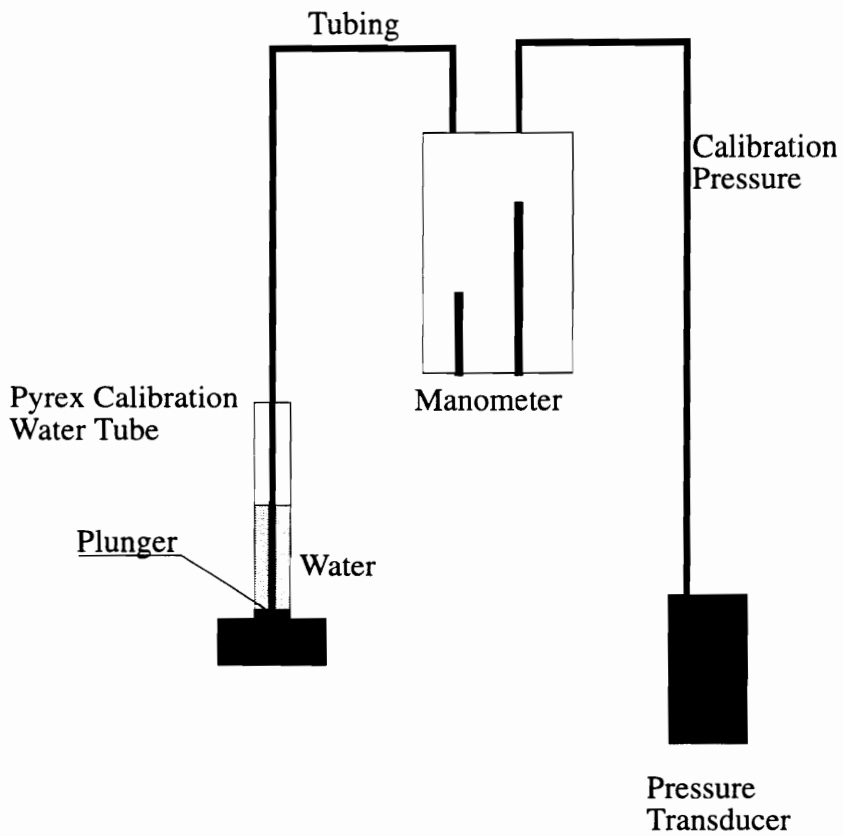


Figure 11.1 Pressure Transducer Calibration Apparatus

line as shown in Figure 11.1, which read a pressure of six inches of water. Each transducer was connected to the calibration pressure system to measure the known calibration pressure.

Each of the Datametrix electronic manometers indicated pressures equal to six inches of water accurate out to two decimal places. The OMEGA pressure transducers produced voltages, measured by a volt meter, that agreed with the manufacturer specified calibration constants. This calibration experiment was carried out again with the water tube filled with four and then two inches of water. Again, each of the electronic manometers indicated pressures accurate out to two decimal places. The OMEGA pressure transducers again produced voltages that agreed with the manufacturer specified calibration constants.

Thermocouples

All thermocouples used in this particular experiment were connected to a DT707-T Data Translation external screw terminal panel. This particular screw terminal panel provides a thermocouple reference cold junction compensation circuit by which the user can determine the temperature of the screw terminal panel. A program then compensates for the cold junction thermocouple formed at the DT707-T. When the cold-junction compensation circuit is calibrated, the sensor output is $0.4\text{mV}/(\text{C})$.

This calibration constant was checked in the test cell. The thermocouples were placed near each other in the test cell with all doors to the test cell closed along with a calibrated thermometer. A space heater in test cell then varied the temperature inside the

test cell. A thermostat setting on the space heater was selected and the space heater was left to operate for 24 hours to ensure the test cell went to an equilibrium temperature. Comparing the temperatures measured by the thermocouples to the temperature measured by the calibrated thermometer, all measurements agreed to the nearest degree. A measurement of the voltage output of the thermocouples with a volt meter, verified the 0.4 mV/(C) calibration constant.

12. APPENDIX C

Mass Flow Measurements

The mass flow passing through the compression system at any given time is determined by pressure and temperature measurements made within the plenum chamber and at the throttle exit plane. Figure 12.1 is a schematic of the compressor and plenum chamber. The compressor and plenum together are considered a control volume and the integral form of the conservation of mass equation is applied to determine the mass flow passing through the compression system at any instant in time. The integral form of the conservation of mass equation is

$$\frac{d}{dt} \left[\int_{cv} \rho \, dVol \right] + \sum_{out} \rho VA - \sum_{in} \rho VA = 0 \quad (12.1)$$

Applying equation (12.1) to the compression system control volume in Figure 12.1 with one inlet at station (1) and one exit at station (5) yields

$$\frac{d}{dt} (\rho_P \, Vol) + \rho_T V_T A_T - \rho_C V_C A_C = 0 \quad (12.2)$$

Station (1) is the compressor inlet and all properties and parameters are denoted by subscript C. Station (5) is the throttle exit plane and all properties and parameters are denoted by subscript T. The properties and parameters associated with the plenum chamber are denoted by subscript P. Differentiating the unsteady term and knowing that the compression system geometric volume is constant yields

$$\frac{d\rho_P}{dt} Vol + \rho_T V_T A_T - \rho_C V_C A_C = 0 \quad (12.3)$$

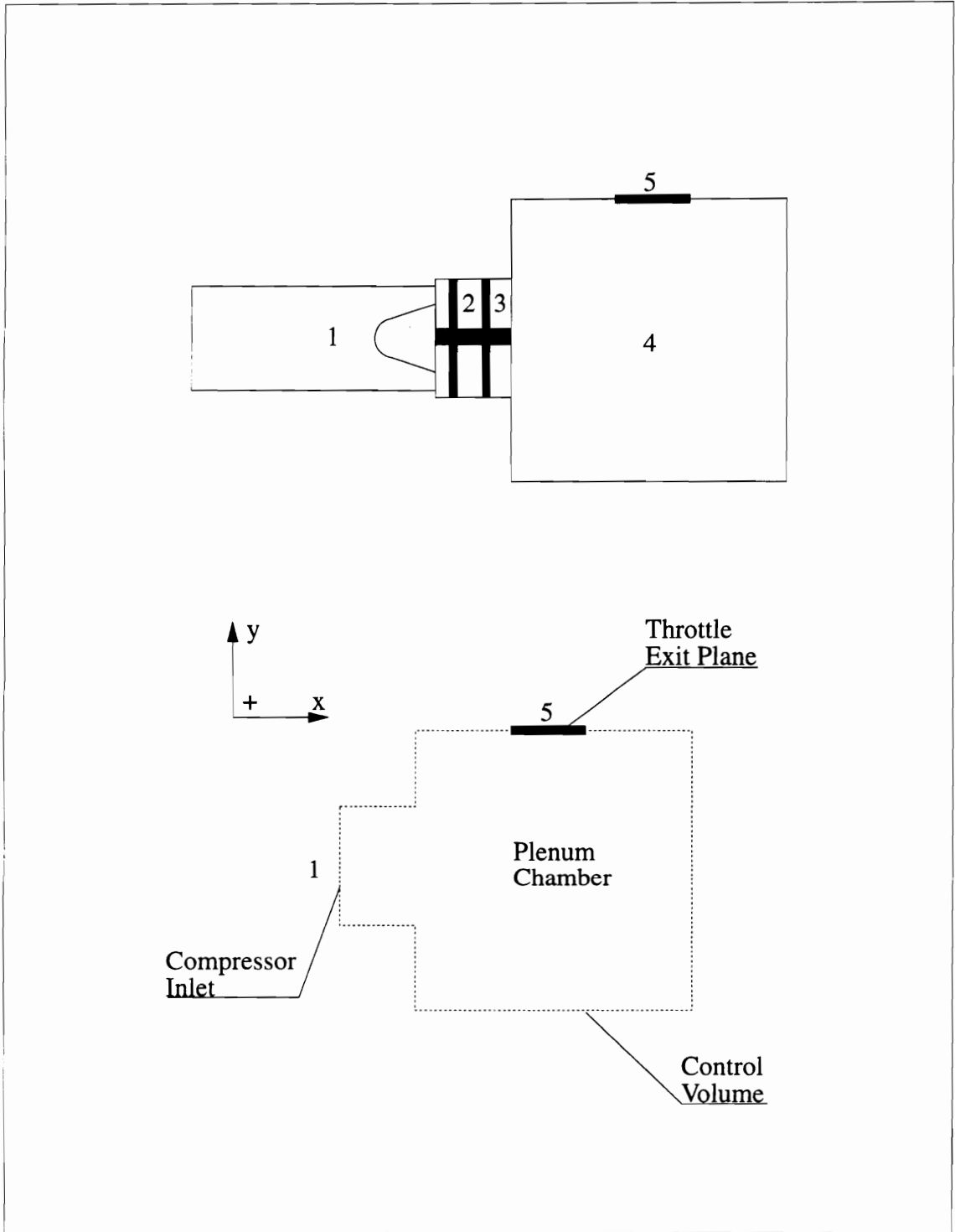


Figure 12.1 Compressor and Plenum Chamber Control Volume

The mass flow passing through the compressor is equal to the mass flux going into the compression system control volume at station (1). Solving for the mass flux at station (1) yields

$$\dot{m}_C = \frac{d\rho_P}{dt} \text{Vol} + \rho_T V_T A_T \quad (12.4)$$

where

$$\dot{m}_C = \rho_C V_C A_C \quad (12.5)$$

During steady state operation of the compressor the time derivative in equation (12.4) is equal to zero, and the equation becomes the continuity equation for a steady state steady flow process. This implies that when the compressor is operating in the steady state, the mass flow passing out the throttle exit plane is equal to the mass flow going into the compressor.

A pitot tube and thermocouple are mounted in the exit plane of the throttle area as shown in Figures 4.11 and 4.13 of the Description Of Experiment chapter. The pitot tube measures the total pressure of the flow leaving the throttle exit plane, while the thermocouple measures the temperature of the flow leaving the throttle exit plane. The probes are positioned outside the plenum chamber to guarantee that the static pressure acting on the probes is the atmospheric pressure. The temperature measurement obtained by the thermocouple allows for the flow density to be determined at the throttle exit plane using the atmospheric pressure and the ideal gas equation of state

$$\rho_T = \frac{Pa}{R T_T} \quad (12.6)$$

The total pressure measurement and flow density allow the flow velocity to be measured at the throttle exit plane using the atmospheric pressure and the Bernoulli equation

$$V_T = \sqrt{\frac{2(P_{0T} - P_a)}{\rho_T}} \quad (12.7)$$

Using the known area and discharge coefficient at the throttle exit plane along with the measured flow density and velocity, the mass flux leaving the control volume was experimentally measured. This was assumed to be the mass flow passing through the compressor during steady state operation.

During an inlet temperature transient, the time derivative in equation (12.4) cannot be set equal to zero. The unsteady term must be retained in the conservation of mass equation to determine the mass flux entering the compression system control volume. Equation (12.4) must be solved with the unsteady term included to determine the mass flow passing through the compressor during an inlet temperature transient.

During a temperature transient, the mass flux leaving the compression system control volume can be experimentally measured using the same approach previously described for the steady state steady flow operating condition. The unsteady term must be numerically approximated. The unsteady term in equation (12.4) is

$$\frac{d\rho_P}{dt} Vol$$

which states that the time rate of change of mass within the control volume is equal to the time rate of change of density within the control volume multiplied by the volume. The

ideal gas equation of state relates flow density inside the plenum chamber to the flow pressure and temperature inside the plenum chamber which can be experimentally measured

$$\rho_P = \frac{P_P}{RT_P} \quad (12.8)$$

Differentiating the ideal gas equation of state with respect to time yields

$$\frac{d\rho_P}{dt} = \frac{1}{R} \frac{\left[T_P \frac{dP_P}{dt} - P_P \frac{dT_P}{dt} \right]}{T_P^2} \quad (12.9)$$

Therefore, the unsteady term in equation (12.4) is equal to

$$\frac{d\rho_P}{dt} \text{Vol} = \frac{\text{Vol}}{R} \frac{\left[T_P \frac{dP_P}{dt} - P_P \frac{dT_P}{dt} \right]}{T_P^2} \quad (12.10)$$

which states that the time rate of change of mass within the compression system control volume can be determined if the static pressure and temperature within the control volume are known as a function of time and space. The time derivatives of static pressure and temperature in equation (12.10) can be numerically approximated from the time histories of static pressure and temperature within the control volume using a finite difference approximation

$$\frac{dP_P}{dt} \approx \frac{\Delta P_P}{\Delta t} = \frac{P_P(t + \Delta t) - P_P(t - \Delta t)}{(t + \Delta t) - (t - \Delta t)} \quad (12.11)$$

$$\frac{dT_P}{dt} \approx \frac{\Delta T_P}{\Delta t} = \frac{T_P(t + \Delta t) - T_P(t - \Delta t)}{(t + \Delta t) - (t - \Delta t)} \quad (12.12)$$

This approach was applied to the plenum chamber of the compression system to approximate the unsteady term in equation (12.4), and solve for the mass flow passing through the compressor during inlet temperature transients. Figures 4.11 and 4.13 in the Description Of Experiment chapter identify where in the plenum chamber the static pressure and temperature measurements were taken for approximating the time derivatives of static pressure and temperature.

Experimental results reveal that the unsteady term in the conservation of mass equation is small and represents less than 5 % of the total mass flow rate passing through the compression system at any instant in time during any of the inlet temperature transients. During a low magnitude inlet temperature excursion such as the one shown in Figure 6.11, the corrected mass flow rate varied from approximately 3.8 lbm/sec to 4.3 lbm/sec. The difference in corrected mass flow rate during this low magnitude inlet temperature excursion is

$$\Delta \dot{m} = 4.3 \text{ lbm / sec} - 3.8 \text{ lbm / sec} = 0.5 \text{ lbm / sec}$$

The numerical average of the minimum and maximum values of corrected mass flow rate during this inlet temperature excursion is

$$\dot{m}_{\text{ave}} = \frac{4.3 \text{ lbm / sec} + 3.8 \text{ lbm / sec}}{2} = 4.05 \text{ lbm / sec}$$

Therefore, the corrected mass flow rate varied by

$$\frac{\pm \Delta \dot{m}(0.5)}{\dot{m}_{ave}} = \frac{\pm 0.5 \text{ lbm / sec (0.5)}}{4.05 \text{ lbm / sec}} = \pm 6\%$$

from the average value of corrected mass flow rate during this low magnitude inlet temperature excursion.

During a high magnitude inlet temperature excursion such as the one shown in Figure 6.1, the corrected mass flow rate varied from approximately 3.6 lbm/sec to 5.4 lbm/sec. The difference in corrected mass flow rate during this low magnitude inlet temperature excursion is

$$\Delta \dot{m} = 5.4 \text{ lbm / sec} - 3.6 \text{ lbm / sec} = 1.8 \text{ lbm / sec}$$

The numerical average of the minimum and maximum values of corrected mass flow rate during this inlet temperature excursion is

$$\dot{m}_{ave} = \frac{5.4 \text{ lbm / sec} + 3.6 \text{ lbm / sec}}{2} = 4.5 \text{ lbm / sec}$$

Therefore, the corrected mass flow rate varied by

$$\frac{\pm \Delta \dot{m}(0.5)}{\dot{m}_{\text{ave}}} = \frac{\pm 1.8 \text{ lbm / sec (0.5)}}{4.5 \text{ lbm / sec}} = \pm 20\%$$

from the average value of corrected mass flow rate during this high magnitude inlet temperature excursion.

Based upon the estimate of uncertainty in mass flow rate determined in Appendix D, the mass flow measurement system is clearly sufficient for measuring the mass flow rate variations that occur during the experiments.

13. APPENDIX D

13.1 Measurement Uncertainty Analysis

Estimates of the uncertainty in the experimental measurements are made in this Appendix. The approach used can be found in reference (12). The approach estimates the uncertainty in an experimental value by taking the square root of the sum of the squares of the contributions of error from each measured quantity used in the determination of the experimental value. Several significant digits are carried through the analysis for the purpose of eliminating any roundoff errors. Final results are then rounded to two significant digits and set off by parenthesis ().

The uncertainty in the pressure and temperature measurements are known from the manufacturer specified error band for the pressure transducers and the thermocouples used in the experiment. Estimates of the uncertainty in the flow density and flow velocity at the throttle exit plane are performed. This uncertainty analysis is based upon the uncertainty associated with the pressure and temperature measurements made at the throttle exit plane. An estimate of the uncertainty in mass flow rate is then made from the estimates of uncertainty in flow density and flow velocity at the throttle exit plane.

13.1.1 Uncertainty in Flow Density At Throttle Exit Plane

The equation for calculating flow density at the throttle exit plane is determined from the ideal gas equation of state

$$\rho_T = \frac{Pa}{R T_T} \quad (13.1)$$

where Pa is the atmospheric pressure at the throttle exit plane and T_T is the static temperature at the throttle exit plane. The independent variables are Pa and T_T . The uncertainty in density, Z_{ρ_T} , is given by

$$Z_{\rho_T} = \left[\left[\frac{\partial \rho_T}{\partial Pa} Z_{Pa} \right]^2 + \left[\frac{\partial \rho_T}{\partial T_T} Z_{T_T} \right]^2 \right]^{\frac{1}{2}} \quad (13.2)$$

The partial derivatives are

$$\frac{\partial \rho_T}{\partial Pa} = \frac{1}{R T_T} \quad (13.3)$$

$$\frac{\partial \rho_T}{\partial T_T} = -\frac{Pa}{R T_T^2} \quad (13.4)$$

A typical value for temperature at the throttle exit plane during an inlet temperature transient is

$$T_T = 960 \text{ (R)}$$

and the atmospheric pressure at the throttle exit plane is

$$P_a = 2146 \text{ (lbf/ft}^2\text{)}$$

Evaluating the partial derivatives yields

$$\frac{\partial \rho_T}{\partial P_a} = 0.000019547 \frac{\text{lbm/ft}^3}{\text{lbf/ft}^2}$$

$$\frac{\partial \rho_T}{\partial T_T} = -0.000043695 \frac{\text{lbm/ft}^3}{\text{(R)}}$$

It is known from the manufacturer that the uncertainty in the temperature and pressure measurements are

$$Z_{P_a} = \pm 0.0705 \frac{\text{lbf}}{\text{ft}^2} \quad \text{and} \quad Z_{T_T} = \pm 2.2 \text{(R)}$$

Substituting these values into equation (13.2) yields

$$Z_{\rho_T} = \left[\left(0.000019547 \frac{\text{lbm/ft}^3}{\text{lbf/ft}^2} \times 0.0705 \frac{\text{lbf}}{\text{ft}^2} \right)^2 + \left(-0.000043695 \frac{\text{lbm/ft}^3}{\text{R}} \times 2.2 \text{(R)} \right)^2 \right]^{\frac{1}{2}}$$

$$Z_{\rho_T} = \pm 0.000096138 \text{ lbm/ft}^3 \quad (\pm 0.000096 \text{ lbm/ft}^3)$$

$$(\pm 0.0015 \text{ kg/m}^3)$$

13.1.2 Uncertainty in Flow Velocity At Throttle Exit Plane

The flow at the throttle exit plane is assumed incompressible and the velocity is calculated from the Bernoulli equation

$$V_T = \left[\frac{2}{\rho_T} (P_{0T} - P_a) \right]^{\frac{1}{2}} \quad (13.5)$$

where P_a is the atmospheric pressure, P_{0T} is the total pressure, and ρ_T is the flow density at the throttle exit plane.

The uncertainty in the calculation of the velocity is given by

$$Z_{V_T} = \left[\left[\frac{\partial V_T}{\partial \rho_T} Z_{\rho_T} \right]^2 + \left[\frac{\partial V_T}{\partial P_{0T}} Z_{P_{0T}} \right]^2 + \left[\frac{\partial V_T}{\partial P_a} Z_{P_a} \right]^2 \right]^{\frac{1}{2}} \quad (13.6)$$

The partial derivatives are

$$\frac{\partial V_T}{\partial \rho_T} = - \left[\frac{(P_{0T} - P_a)}{\rho_T^2} \right] \left[\frac{2}{\rho_T} (P_{0T} - P_a) \right]^{-\frac{1}{2}} \quad (13.7)$$

$$\frac{\partial V_T}{\partial P_{0T}} = \frac{1}{\rho_T} \left[\frac{2}{\rho_T} (P_{0T} - P_a) \right]^{-\frac{1}{2}} \quad (13.8)$$

$$\frac{\partial V_T}{\partial P_a} = - \frac{1}{\rho_T} \left[\frac{2}{\rho_T} (P_{0T} - P_a) \right]^{-\frac{1}{2}} \quad (13.9)$$

Typical values of total and atmospheric pressure at the throttle exit plane during an inlet temperature transient are

$$P_{0_T} = 2159.52 \text{ (lbf/ft}^2\text{)}$$

$$P_a = 2146 \text{ (lbf/ft}^2\text{)}$$

and a typical flow density at the throttle exit plane is

$$\rho_T = 0.042 \text{ (lbm/ft}^3\text{)}$$

Evaluating the partial derivatives yields

$$\frac{\partial V_T}{\partial \rho_T} = -1713.373088 \frac{\text{ft / sec}}{\text{lbm / ft}^3}$$

$$\frac{\partial V_T}{\partial P_{0_T}} = 5.322608705 \frac{\text{ft / sec}}{\text{lbf / ft}^2}$$

$$\frac{\partial V_T}{\partial P_a} = -5.322608705 \frac{\text{ft / sec}}{\text{lbf / ft}^2}$$

The uncertainty in the density and atmospheric pressure measurements are known from the previous calculation of uncertainty for flow density

$$Z_{\rho_T} = \pm 0.000096138 \frac{\text{lbm}}{\text{ft}^3}$$

$$Z_{P_a} = \pm 0.0705 \frac{\text{lbf}}{\text{ft}^2}$$

The uncertainty in the total pressure measurement is known from the manufacturer as $\pm 0.15\%$ of the measured value. A typical value of total pressure measured at the throttle exit plane is 2.6 inches of water. Therefore, the uncertainty in total pressure at the throttle exit plane is

$$Z_{P_{0T}} = \pm 0.02028 \frac{\text{lbf}}{\text{ft}^2}$$

Substituting these values into equation (13.6) yields

$$Z_{V_T} = \left[\left(-1713.373088 \frac{\text{ft} / \text{sec}}{\text{lbm} / \text{ft}^3} \times 0.000096138 \text{ lbm} / \text{ft}^3 \right)^2 + \left(5.322608705 \frac{\text{ft} / \text{sec}}{\text{lbf} / \text{ft}^2} \times 0.02028 \text{ lbf} / \text{ft}^2 \right)^2 + \left(-5.322608705 \frac{\text{ft} / \text{sec}}{\text{lbf} / \text{ft}^2} \times 0.0705 \text{ lbf} / \text{ft}^2 \right)^2 \right]^{\frac{1}{2}}$$

$$Z_{V_T} = \pm 0.423783368 \text{ ft/sec} \quad (\pm 0.42 \text{ ft/sec}) \\ (\pm 0.13 \text{ m/s})$$

13.1.3 Uncertainty in Mass Flow Rate

The mass flow rate is determined from the integral form of the conservation of mass equation

$$\dot{m}_C = \dot{m}_T + \frac{d(\rho_P \text{Vol})}{dt} \quad (13.10)$$

where \dot{m}_C is the mass flow rate passing through the compressor and \dot{m}_T is the mass flow

rate passing through the throttle exit plane. The unsteady term $\frac{d(\rho_P \text{Vol})}{dt}$ was

numerically evaluated during the data reduction process to calculate the dynamic mass flow rate for the experiments using the procedure described in Appendix C. It is known

from the data reduction process that the unsteady term $\frac{d(\rho_P \text{Vol})}{dt}$ is small and represents

no more than 5 % of the total mass flow rate passing through the compression system at any instant in time during any of the inlet temperature transients. Neglecting the unsteady term in equation (13.10), the mass flow rate passing through the compression system may be approximated as

$$\dot{m}_C \approx \dot{m}_T \quad (13.11)$$

where $\dot{m}_T = \rho_T V_T A_T$

The uncertainty in the calculation of the mass flow rate is given by

$$Z_{\dot{m}_T} = \left[\left[\frac{\partial \dot{m}_T}{\partial \rho_T} Z_{\rho_T} \right]^2 + \left[\frac{\partial \dot{m}_T}{\partial V_T} Z_{V_T} \right]^2 + \left[\frac{\partial \dot{m}_T}{\partial A_T} Z_{A_T} \right]^2 \right]^{\frac{1}{2}} \quad (13.12)$$

The throttle exit area does not change during the experiments therefore the uncertainty in the throttle exit area Z_{A_T} is set equal to zero. This yields for the uncertainty in the calculation of the mass flow rate

$$Z_{\dot{m}_T} = \left[\left[\frac{\partial \dot{m}_T}{\partial \rho_T} Z_{\rho_T} \right]^2 + \left[\frac{\partial \dot{m}_T}{\partial V_T} Z_{V_T} \right]^2 \right]^{\frac{1}{2}} \quad (13.13)$$

The partial derivatives are

$$\frac{\partial \dot{m}_T}{\partial \rho_T} = V_T A_T \quad (13.14)$$

$$\frac{\partial \dot{m}_T}{\partial V_T} = \rho_T A_T \quad (13.15)$$

During a high magnitude inlet temperature transient such as the transient applied in Figure 6.1, the corrected mass flow rate varies from approximately 3.6 lbm/sec to 5.4 lbm/sec. Typical values of flow density and flow velocity at the throttle exit plane during this high magnitude inlet temperature transient are

$$V_T = 169 \text{ (ft / sec)}$$

$$\rho_T = 0.042 \text{ (lbm / ft}^3\text{)}$$

The throttle exit area is

$$A_T = 0.52(\text{ft}^2)$$

Evaluating the partial derivatives yields

$$\frac{\partial \dot{m}_T}{\partial \rho_T} = 87.88 \frac{\text{lbm} / \text{sec}}{\text{lbm} / \text{ft}^3}$$

$$\frac{\partial \dot{m}_T}{\partial V_T} = 0.02184 \frac{\text{lbm} / \text{sec}}{\text{ft} / \text{sec}}$$

The uncertainty in the flow density and flow velocity at the throttle exit plane are known from the previous calculations of flow density and flow velocity at the throttle exit plane

$$Z_{\rho_T} = \pm 0.000096138 \text{ lbm}/\text{ft}^3$$

$$Z_{V_T} = \pm 0.423783368 \text{ ft}/\text{sec}$$

Substituting these values into equation (13.13) yields

$$Z_{\dot{m}_T} = \left[\left(87.88 \frac{\text{lbm}}{\text{sec}} \times 0.000096138 \frac{\text{lbm}}{\text{ft}^3} \right)^2 + \left(0.02184 \frac{\text{lbm}}{\text{ft} / \text{sec}} \times 0.423783368 \frac{\text{ft}}{\text{sec}} \right)^2 \right]^{\frac{1}{2}}$$

$$Z_{\dot{m}_T} = \pm 0.012531637 \text{ lbm}/\text{sec} \quad (\pm 0.0125 \text{ lbm}/\text{sec})$$

$$\quad \quad \quad (\pm 0.0057 \text{ kg}/\text{s})$$

$$\text{where } \dot{m}_C \approx \dot{m}_T = \rho_T V_T A_T = \begin{array}{l} 3.69 \text{ lbm/sec} \\ (1.674 \text{ kg/s}) \end{array}$$

13.2 Frequency Response Of Pressure Measurement Systems

The pressure measurement systems, used to measure the pressures at various stations of the compression system during the transient inlet temperature excursions, were required to have adequate frequency response. The pressure measurement systems used to measure pressures for this experiment consisted of the compressor pressure measurement system and the plenum pressure measurement system. The compressor pressure measurement system obtained pressure measurements from the stages of the compressor. The plenum pressure measurement system obtained pressure measurements from the plenum chamber and throttle exit plane.

The compressor pressure measurement system consisted of two total pressure probes mounted directly behind each of the compressor stage rotors as previously described in the Description Of Experiment chapter. Each total pressure probe connected to a Tygon tube that was 0.25 inches (0.0064 m) in diameter and 3 ft (0.91 m) in length. The Tygon tubes connected directly to the Barocel pressure transducers. The plenum pressure measurement system consisted of a total pressure probe mounted in the throttle exit plane and a static pressure tap mounted on the plenum chamber wall as previously described in the Description Of Experiment chapter. The total pressure probe and the static pressure tap each connected to a Tygon tube that was 0.125 inches (0.0032 m) in

diameter and 4 ft (1.22 m) in length. Each Tygon tube connected directly to a pressure transducer.

To investigate the limits of frequency response of the pressure measurement systems used in this experiment, a model-based calculation and prediction procedure was used. The frequency response is based upon an analysis found in reference (10). The analysis requires the specification of the pressure measurement system geometry and fluid media. The output from the analysis is the frequency response of the pressure measurement system. A computer program based upon this analysis was available at AlliedSignal Engines and was executed on the compressor and plenum pressure measurement systems used in this experiment. The results of the analysis are shown in Figure 13.1.

Figure 13.1 is a plot of response versus frequency for the compressor and plenum pressure measurement systems. The ordinate of Figure 13.1 is expressed in decibels making this a convenient scale to use for the analysis. The equation relating decibels to pressures is

$$\text{dB} = -20 \log_{10}(\text{P}_{\text{measured}}/\text{P}_{\text{actual}}) \quad (13.16)$$

or

$$\text{P}_{\text{actual}} = \text{P}_{\text{measured}}/[10^{(\text{dB} / -20)}] \quad (13.17)$$

The abscissa in Figure 13.1 is expressed in Hz and represents the frequency at which pressure variations enter the pressure measurement systems.

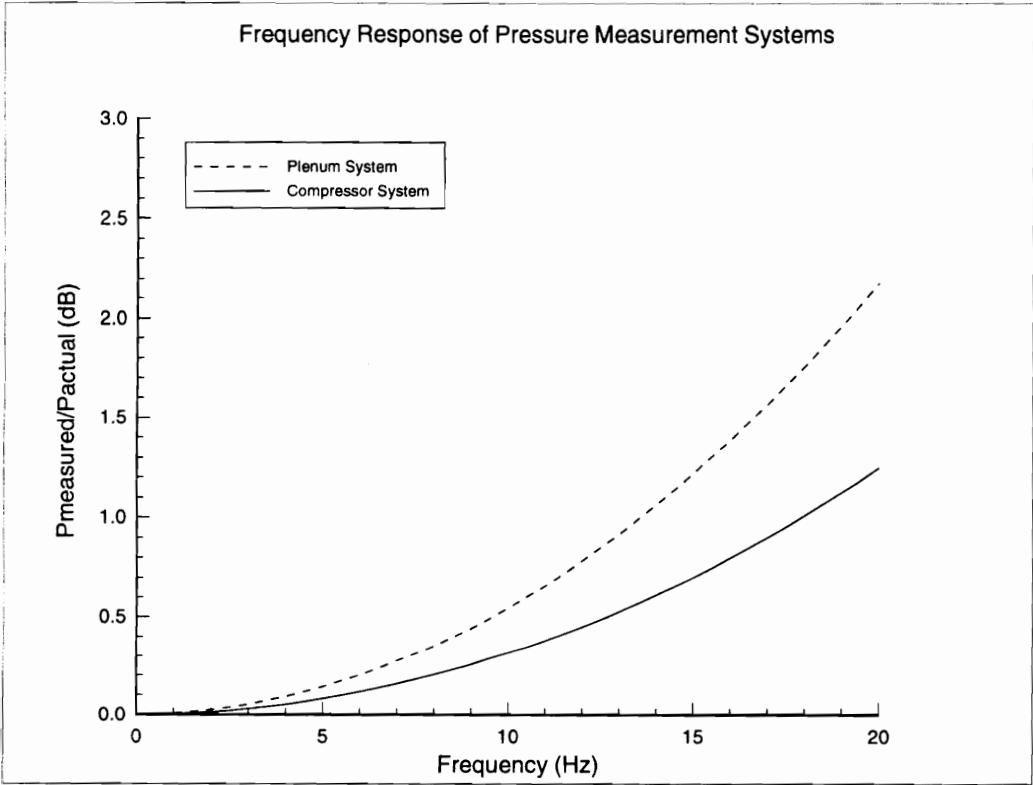


Figure 13.1 Frequency Response Of Pressure Measurement Systems

Temperature transients applied across the compressor inlet occur at frequencies of 1 Hz or less. This is demonstrated by the data obtained during the experiments. Therefore, the corresponding decrease in compressor pressure rise, due to the inlet temperature transients, will also occur at a frequency of 1 Hz or less. This is demonstrated by the data obtained during the experiments. Assuming that these low frequency pressure signals enter both the compressor and plenum pressure measurement systems at frequencies of 1 Hz or less, the ratio of ($P_{\text{measured}}/P_{\text{actual}}$) in dB for both the compressor and plenum pressure measurement systems are approximately equal to zero as determined from Figure 13.1. Evaluating equation (13.17) yields, $P_{\text{actual}} = P_{\text{measured}}$ for both the compressor and plenum pressure measurement systems.

This implies that, for the frequencies at which pressure signals enter both pressure measurement systems in the experiments, the effects and influence of the measurement systems on the respective measured pressures for both the compressor and plenum pressure measurement systems are negligible. No additional uncertainty is introduced into the compressor and plenum pressure measurements by the frequency characteristics of the measurement systems when measuring these low frequency pressures.

However, the information contained in the compressor rotating stall pressure signatures will have uncertainty due to the influence of the pressure measurement systems. Examination of experimental data for the compressor pressure rise while the compressor is in rotating stall operation reveals that the rotating stall pressure signatures contain fluctuating pressures at approximately 20 Hz. For this measurement system, the

ratio of ($P_{\text{measured}}/P_{\text{actual}}$) is approximately 1.25 dB for the compressor pressure measurement system as determined from Figure 13.1. Evaluating equation (13.17) for the compressor pressure measurement system yields

$$\frac{P_{\text{measured}}}{P_{\text{actual}}} = 0.8659643 \quad (13.18)$$

Thus, the pressure fluctuations measured by the compressor pressure measurement system at a frequency of 20 Hz are expected to be low by approximately 13.4 % due to the influence of the measurement system. Since the rotating stall signatures (not the magnitude) were of interest in this investigation, this effect was not of concern.

14. APPENDIX E

Instrumentation/Hardware

14.1 Computer/Data Acquisition System

Edison 286 computer: A, B, and C drives

Data Translation board : DT2805

Analog Input Specifications:

Accuracy

Resolution	12 bits
Programmable gain	500
Accuracy	$\pm 0.05\%$ FSR(gain=500): 12-bit A/D
Noise	0.03% FSR RMS
Linearity	To within ± 0.5 LSB
Gain error	Adjustable to zero
Offset error	Adjustable to zero

Temperature

Operating Range	0 to 50 (C)
Monotonicity	0 to 50 (C)
A/D zero drift	$\pm 20 \mu V/C$
Amplifier zero drift	$\pm 3 \mu V/C$
Gain drift	± 35 ppm of FSR/C

Dynamic Performance

Throughput	6,000 Hz to 13,700 Hz
------------	-----------------------

Input Specifications

Number of channels	8 DI (jumper selectable)
Maximum input voltage without damage, power on	$\pm 30V$
Input noise	$10 \mu V$ RMS
Channel to channel input error	$\pm 10 \mu V$
Coding	Straight binary, offset binary

Ranges

Programmable input ranges	$\pm 20mV, \pm 100mV, \pm 1mV, \pm 10mV$
bipolar	0 to 20 mV, 0 to 100 mV
unipolar	0 to 1 V, 0 to 10 V

Analog Output Specifications:

Accuracy

Resolution	12 bits
Non-linearity	0.02%
Differential linearity	± 0.5 LSB
Dynamic Performance	
Settling time to 0.01%	35 μ S
FSR (10V step)	
Settling time to 0.01%	10 μ S
FSR (100mV step)	
Slew rate	0.5V/ μ S
Temperature	
Operating Range	0 to +50 (C)
Monotonicity	0 to +50 (C)
Offset drift (unipolar)	± 3 ppm of FSR/C
Offset drift (bipolar)	± 30 ppm of FSR/C
Gain drift	± 30 ppm of FSR/C

Screw Terminal Panel : DT707-T

General Specifications

Outline dimensions	5.2"HX8.75"WX0.875"D
Weight	12.5 ounces
Screw Terminal	80 barrier strip connections in 4 sections of 20 connections each
Barrier Strip Screw Size	6-32 Screws
Marrir Strip Screw Material	Magnum
Barrier Strip Material	Polyester, UL grade, 94V-O polypropylene
Acceptable Wire Size	18 to 22 AWG

User-Supplied Current Loop Specifications

Resistor Value	250 ohms (0 to 20 mA current range)
Resistor Tolerance	± 0.2 % or better
Resistor Power Dissipation	0.25 watts
Resistor Temperature	
Coefficient	± 15 ppm/C or better

Thermocouple Cold-Junction Compensation Circuit

Output Impedance	Amplifier Output 100 milliohms 100 ohm divider
Output Voltage Equation	Output Voltage = 0.5mV x T where T= temperature of D707-T board in (C)
Operating Temperature	
Range	0 to +50 (C)
Power Requirements	± 15 volts, 5.5 mA

3M Ribbon cable : 3426

14.2 Ignition System

Ignition Coil : Standard 12 volts 197U

Ignition Wire : Standard Metallic Core : 3402

Power Supply :Hewlett Packard 6200 B DC power supply, No.67744

Signal Generator: Hewlett Packard 200 S signal generator, No.325

Capacitive Discharge Ignitor : Tiger SST 123172

Spark Plug : RFN16LY

14.3 Fuel/Fuel Control

Propane 100 lbf cylinder 110 psig

Electronic Solid State Relay : CRYDOM TD1210 120V-10 A

Solenoid Coil : Dayton 120 volts, 50/60 Hz 6X543

Solenoid Valve : Dayton 2cm 1A578

Wire : Archer 18-GA (polarized)

14.4 Compressor Control

Rheostat: General Electric 5748472G130

Drive Motor: General Electric KINEMATIC Direct Current Generator 5CD256G38

Compressor: General Electric Fan Unit 7A5-A1

14.5 Thermocouples

Thermocouple Wire : OMEGA Chromel Alumel Type K

Thermocouple : Chromel/Alumel, Type K, 0.005 inch diameter, exposed junction

Thermocouple Response Time : 0.08 (s)

Thermocouple Measurement Error : ± 2.2 (C)

Thermocouple Sample Rate : 30 samples/sec or 0.03 sec/sample

Number Of Thermocouples Measuring : 14

Calibration Constant : 0.4 mV/(C)

14.6 Pressure Transducers

OMEGA Pressure Transducer

General Specifications :

Model Number : PX800-001GV

Pressure Range : 0-1 psig

Supply Voltage : 10 volts

Zero Offset : 0 ± 3 mV

Sensitivity : 1.67mV/V/PSI

Non Linearity & Hysteresis : max $\pm 0.1\%$ BSL

Temperature Error Band : max $\pm 1.5\%$ FRO

Compensated Temperature Range : -20 (C) to +80 (C)

Pressure Connection : 0.25 NPT Flat

Electrical Connection

Cable Length : 3 FEET

Positive Supply : Red

Negative Supply : White

Positive Output : Yellow

Negative Output : Blue

Excitation : 10 Vdc at 15 mA

Output : 17 mV

Output Impedance : 1000 ohms nominal

Load Impedance : > 100 kilohm for rated performance

Accuracy : $\pm 0.1\%$ BFSL

Zero Balance : ± 3 mV

Span Setting : ± 10 mV

Compensated Temperature Range : -20 to 80 (C)

Overpressure Rating : 10X for 1 psig range

Natural Frequency : 28 kHz

Mechanical Shock : 1000g for 1 ms

Acceleration : 0.006% FSO/g

Pressure Media : Fluids compatible with quartz and titanium

Transducer Principle : Integrated silicon gage bridge

Pressure Port : 0.25-18 NPT

Electrical Connection : 36" 4-wire shielded cable

Calibration Constant : 1 psig = 16.7 mV

Datametrics Type 590 Integral Barocel Pressure Transducer

General Specifications :

Pressure Range : 10 inches of water

Power Requirements : 18 to 35 Volts DC or 20 to 33 Volts AC at 75 ma. 50-60 Hz

Output Signal : 0 to ± 10 VDC, 2 ma into 5 K Ω load, floating (Code-4), zero adjustable ± 0.5 %, span adjustable ± 1.0 %

Leak Rate to Ambient : Viton-sealed model (Code-V) $5E-7$ std cc/sec @ 760 Torr
All-welded model (Code-H) $1E-10$ std cc/sec @ 760 Torr

Electrical Fittings : MS3102A-16S-1PZ (One mating connector, MS3106A-16S-1SZ is supplied with each 590 transducer)

Pressure Fittings : 1/8"-27 NPT (Code-1) standard

Volume : 5.0 cc per side, with zero differential pressure applied, 0.16 cc diaphragm displacement with full range pressure applied

Transient Response : 8 msec (to step input of zero to sensor full pressure range pressure, at 1 atm line pressure, with no external tubulation, measured to 63 % f.s.

Diaphragm Resonant Frequency : 3khz (nominal)

Overpressure : 1.5 times sensor full range

Ambient Temperature Range : Storage : -45 (C) to +85 (C)
Operating : +5 (C) to +70 (C)
Calibration : +10 (C) to +50 (C)

Temperature Effects : 30 ppm/(C) on zero, 300 ppm/(C) on slope

Accuracy (zero-based linearity): $\pm(0.15\% \text{ of reading} + 0.01\% \text{ f.s.})$

Repeatability : 0.01 % of reading +0.005 % of maximum applied pressure

Hysteresis Error : $\pm 0.001\%$

Datametrix Type 1400 Electric Manometer

General Specifications :

Display : 3 1/2 digits, update twice per second

Power Requirements : 115 VAC, 50-60 Hz, 0.2 amp

Outputs : 28 VDC, capable of powering up to 6 Barocels and one Type 1402
Barocel Selector, 0 to ± 1 VDC pressure signal, BCD
DTL/T2L compatible

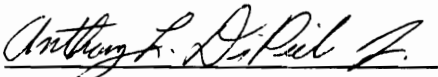
Controls : Power ON/OFF, Zero and Span adjustment, Range switch with X1 and
X0.1 scales, and CALIBRATE position

Ambient Temperature : Operating +10 (C) to +40 (C) Storage -45 (C) to +55 (C)

Interconnecting Cables : Type 711-15, 15 feet in length

15. VITA

The author, Anthony L. DiPietro Jr., was born on September 7, 1968 in Salem Massachusetts. He attended Herndon High School and graduated with honors in June of 1986. Entering Virginia Polytechnic Institute and State University in the fall of 1986, he graduated with a Bachelor of Science Degree in Aerospace Engineering in May of 1991. He began graduate studies at Virginia Polytechnic Institute and State University in the fall of 1991 and graduated in May of 1993 with a Master of Science Degree in Aerospace Engineering. He began to pursue a Doctor of Philosophy Degree in Mechanical Engineering in the fall of 1993 and plans to graduate in spring of 1997. After graduation he plans to begin a career in industry as a research scientist conducting experimental research in the area of gas turbine engines and turbomachinery design.


Anthony L. DiPietro Jr.